



**Nebraska  
Transportation  
Center**



Report TRP-03-311-14  
DPS-STWD (118)

Final Report

## **Predicting the Dynamic Fracture of Steel via a Non-Local Strain-Energy Density Failure Criterion**

**Kevin D. Schrum, M.S.C.E., E.I.T.**

Graduate Research Assistant  
Midwest Roadside Safety Facility  
University of Nebraska-Lincoln

**Dean L. Sicking, Ph.D., P.E.**

Emeritus Professor

**Ronald K. Faller, Ph.D, P.E.**

Research Associate Professor  
Midwest Roadside Safety Facility Director

**John D. Reid, Ph.D.**

Professor

---

2014

Nebraska Transportation Center  
262 WHIT  
2200 Vine Street  
Lincoln, NE 68583-0851  
(402) 472-1975

"This report was funded in part through grant[s] from the Federal Highway Administration [and Federal Transit Administration], U.S. Department of Transportation. The views and opinions of the authors [or agency] expressed herein do not necessarily state or reflect those of the U. S. Department of Transportation."



*NDOR Sponsoring Agency Contract No. DPS-STWD (118)*

# **PREDICTING THE DYNAMIC FRACTURE OF STEEL VIA A NON LOCAL STRAIN- ENERGY DENSITY FAILURE CRITERION**

Submitted by

Kevin D. Schrum, M.S.C.E, E.I.T.  
Graduate Research Assistant

Dean L. Sicking, Ph.D., P.E.  
Emeritus Professor

Ronald K. Faller, Ph.D., P.E.  
Research Associate Professor  
MwRSF Director

John D. Reid, Ph.D.  
Professor

## **MIDWEST ROADSIDE SAFETY FACILITY**

Nebraska Transportation Center  
University of Nebraska-Lincoln  
130 Whittier Research Center  
2200 Vine Street  
Lincoln, Nebraska 68583-0853  
(402) 472-0965

Submitted to

**NEBRASKA DEPARTMENT OF ROADS**  
1500 Nebraska Highway 2  
Lincoln, NE 68502

**FEDERAL HIGHWAY ADMINISTRATION –  
Nebraska Division**  
100 Centennial Mall – Room 220  
Lincoln, NE 68508

MwRSF Research Report No. TRP-03-311-14

June 23, 2014

## TECHNICAL REPORT DOCUMENTATION PAGE

1. Report No. TRP-03-311-14	2.	3. Recipient's Accession No.	
4. Title and Subtitle Predicting the Dynamic Fracture of Steel via a Non Local Strain-Energy Density Failure Criterion		5. Report Date June 23, 2014	
		6.	
7. Author(s) Schrum, K.D., Sicking, D.L., Faller, R.K., Reid, J.D.		8. Performing Organization Report No. TRP-03-311-14	
9. Performing Organization Name and Address Midwest Roadside Safety Facility (MwRSF) Nebraska Transportation Center University of Nebraska-Lincoln 130 Whittier Research Center 2200 Vine Street Lincoln, Nebraska 68583-0853		10. Project/Task/Work Unit No.	
		11. Contract © or Grant (G) No. NDOR DPS-STWD (118)	
12. Sponsoring Organization Name and Address Nebraska Department of Roads 1500 Nebraska Highway 2 Lincoln, NE 68502  Federal Highway Administration – Nebraska Division 100 Centennial Mall North – Room 220 Lincoln, NE 68508		13. Type of Report and Period Covered 2012 – 2014	
		14. Sponsoring Agency Code	
15. Supplementary Notes Prepared in cooperation with U.S. Department of Transportation, Federal Highway Administration.			
16. Abstract (Limit: 200 words) Predicting the onset of fracture in a material subjected to dynamic loading conditions has typically been heavily mesh-dependent, and often must be specifically calibrated for each geometric design. This can lead to costly models and even costlier physical testing. In response to this, a failure criterion was created based on the strain energy density (SED) of the material. Calculations to obtain the SED were developed to take advantage of a non-local length scale, wherein the sensitivity to mesh density was partially reduced. This method was applied to a steel coupon subjected to dynamic uniaxial tension. A one-time calibration was used to determine the material's critical SED in the non-local length scale. This length scale was dependent on the mesh density of the model and a prescribed magnifier, such that the failure criterion was a function of the length scale. Steel coupons were modeled and tested dynamically. Thicknesses of those coupons were varied and stress concentrations were included. Differing grades of steel were also employed. The non-local SED failure criterion provided consistent and accurate predictions, regardless of the changes in dimensions of the coupons.			
17. Document Analysis/Descriptors Steel Fracture, Failure Criterion, Dynamic Loading Conditions, Peridynamics, Strain-Energy Density, Stress Concentration, LS-DYNA, FORTRAN		18. Availability Statement No restrictions. Document available from: National Technical Information Services, Springfield, Virginia 22161	
19. Security Class (this report) Unclassified	20. Security Class (this page) Unclassified	21. No. of Pages 163	22. Price

## **DISCLAIMER STATEMENT**

This report was completed with funding from the Federal Highway Administration, U.S. Department of Transportation. The contents of this report reflect the views and opinions of the authors who are responsible for the facts and the accuracy of the data presented herein. The contents do not necessarily reflect the official views or policies of the Nebraska Department of Roads nor the Federal Highway Administration, U.S. Department of Transportation. This report does not constitute a standard, specification, regulation, product endorsement, or an endorsement of manufacturers.

## **UNCERTAINTY OF MEASUREMENT STATEMENT**

The Midwest Roadside Safety Facility (MwRSF) has determined the uncertainty of measurements for several parameters involved in standard full-scale crash testing and non-standard testing of roadside safety features. Information regarding the uncertainty of measurements for critical parameters is available upon request by the sponsor and the Federal Highway Administration. Test nos. DFS-L1 through DFS-L7 and DFS-T1 through DFS-T3 were non-certified component tests conducted for research and development purposes only and are outside the scope of the MwRSF's A2LA Accreditation.



## **ACKNOWLEDGEMENTS**

The authors wish to acknowledge several sources that made a contribution to this project:

(1) The Nebraska Department of Roads and the Federal Highway Administration for sponsoring this project; and (2) MwRSF personnel for constructing the systems and conducting the component tests.

Acknowledgement is also given to the following individuals who made a contribution to the completion of this research project.

### **Midwest Roadside Safety Facility**

J.C. Holloway, M.S.C.E., E.I.T., Test Site Manager  
K.A. Lechtenberg, M.S.M.E., E.I.T., Research Associate Engineer  
R.W. Bielenberg, M.S.M.E., E.I.T., Research Associate Engineer  
S.K. Rosenbaugh, M.S.C.E., E.I.T., Research Associate Engineer  
J.D. Schmidt, Ph.D., P.E., Post-Doctoral Research Associate  
C.S. Stolle, Ph.D., Post-Doctoral Research Associate  
A.T. Russell, B.S.B.A., Shop Manager  
K.L. Krenk, B.S.M.A., Maintenance Mechanic  
S.M. Tighe, Laboratory Mechanic  
D.S. Charroin, Laboratory Mechanic  
Undergraduate and Graduate Research Assistants

### **Nebraska Department of Roads**

Phil TenHulzen, P.E., Design Standards Engineer  
Jim Knott, P.E., State Roadway Design Engineer  
Jodi Gibson, Research Coordinator

### **Federal Highway Administration**

John Perry, P.E., Nebraska Division Office  
Danny Briggs, Nebraska Division Office

## TABLE OF CONTENTS

TECHNICAL REPORT DOCUMENTATION PAGE .....	i
DISCLAIMER STATEMENT .....	ii
UNCERTAINTY OF MEASUREMENT STATEMENT .....	ii
ACKNOWLEDGEMENTS .....	iii
TABLE OF CONTENTS .....	iv
LIST OF FIGURES .....	vii
LIST OF TABLES .....	x
1 INTRODUCTION .....	1
1.1 Problem Statement .....	1
1.2 Research Objectives .....	2
1.3 Research Plan .....	2
2 LITERATURE REVIEW .....	3
2.1 Fracture Mechanics .....	3
2.1.1 Griffith Theory .....	3
2.1.2 Linear-Elastic Fracture Mechanics .....	3
2.1.3 Elastic-Plastic Fracture Mechanics .....	5
2.1.3.1 J Integral .....	5
2.1.3.2 Crack-Tip-Opening Displacement (CTOD) .....	6
2.1.4 Strain Energy Density .....	6
2.1.5 Dynamic Loading and Fracture .....	9
2.2 Behavior of Steel .....	10
2.3 Local Fracture Modeling Techniques .....	11
2.3.1 Element Deletion .....	12
2.3.2 Tied Nodes with Failure .....	12
2.3.3 Cohesive Zone Models (CZM) .....	13
2.3.4 Overlapping Tied Shells .....	13
2.3.5 Extended Finite Element Method (XFEM) .....	14
2.3.6 LS-DYNA .....	15
2.4 Non Local Fracture Modeling Techniques .....	15
2.4.1 Molecular Dynamics .....	15
2.4.2 Peridynamics .....	16
2.4.3 Coupling FEM and Peridynamics .....	17
3 RESEARCH APPROACH AND METHODOLOGY .....	19
4 MESH SENSITIVITY OF EXISTING TECHNIQUES .....	21
4.1 Parametric Model Description .....	21
4.2 Maximum Plastic Strain .....	27

4.3 Tied Nodes with Failure.....	27
4.4 Maximum Principal Strain.....	27
4.5 Maximum Shear Strain.....	28
4.6 Summary and Discussion.....	28
4.7 Hourglass Energy.....	34
5 DYNAMIC TENSILE TESTING SETUP .....	35
5.1 Purpose.....	35
5.2 Scope.....	35
5.3 Summary of Steel Coupons and Component Tests.....	36
5.4 Evolution of Testing Phase .....	36
5.5 Equipment and Instrumentation.....	38
5.5.1 Bogies .....	39
5.5.2 Load Cells .....	40
5.6 Accelerometers .....	41
5.6.1 Digital Photography .....	42
5.6.2 Gauge Length Grid .....	43
5.7 Coupon Descriptions.....	44
5.7.1 Test Nos. DFS-L1 and DFS-L2 .....	44
5.7.2 Test No. DFS-L3.....	45
5.7.3 Test No. DFS-L3-2 .....	45
5.7.4 Test No. DFS-L4.....	46
5.7.5 Test No. DFS-L5.....	46
5.7.6 Test Nos. DFS-L6 and DFS-L7 .....	47
5.7.7 Test Nos. DFS-T1, DFS-T2, and DFS-T3 .....	48
6 TENSILE TEST RESULTS .....	50
6.1 Quasi-Static Material Testing .....	50
6.1.1 A572 Gr. 50 Steel .....	50
6.1.2 AASHTO M180 Steel.....	51
6.1.3 A1011-12B Gr. 50 Steel .....	52
6.1.4 LS-DYNA Description of Materials.....	53
6.2 Dynamic Coupon Tests.....	54
6.2.1 Test No. DFS-L1.....	54
6.2.2 Test No. DFS-L2.....	56
6.2.3 Test No. DFS-L3.....	58
6.2.4 Test No. DFS-L3-2 .....	59
6.2.5 Test No. DFS-L4.....	61
6.2.6 Test No. DFS-L5.....	64
6.2.7 Test No. DFS-L6.....	66
6.2.8 Test No. DFS-L7.....	69
6.2.9 Test No. DFS-T1.....	72
6.2.10 Test No. DFS-T2.....	74
6.2.11 Test No. DFS-T3.....	77
6.3 Summary of Dynamic Tensile Tests.....	79
6.4 Discussion.....	80

7 NON LOCAL SED FAILURE CRITERION.....	83
7.1 Strain Energy Density Calculation.....	83
7.2 Calculating Etr.....	86
7.3 Failure Criterion.....	88
7.3.1 General.....	88
7.3.2 A572 Gr 50 .....	91
7.4 Additional Material Failure Criterion .....	97
7.5 Comparison to Physical Testing .....	98
7.5.1 A572.....	98
7.5.2 M180.....	99
7.5.3 A1011.....	100
7.6 Discussion .....	101
8 ADDITION OF A STRESS CONCENTRATION.....	104
8.1 Stress Concentration Factor .....	104
8.2 Application to SED .....	105
8.3 Post-Processing Parameters .....	105
8.4 Comparison to Physical Tests.....	106
8.4.1 A572.....	106
8.4.2 M180 .....	107
8.4.3 A1011.....	108
8.5 Discussion .....	109
9 EXAMPLE APPLICATION – W-BEAM GUARDRAIL .....	111
9.1 Background Research .....	111
9.2 Modeling with SED Failure Criterion.....	114
9.2.1 Splice Holes .....	115
9.3 Discussion.....	118
9.4 Conclusion and Recommendations.....	119
10 CONCLUSIONS AND RECOMMENDATIONS .....	120
10.1 Summary .....	120
10.2 Conclusions.....	121
10.3 Recommendations.....	124
11 LIMITATIONS AND FUTURE WORK .....	126
11.1 Limitations to the Current Work.....	126
11.2 Recommendations for Future Work.....	127
12 REFERENCES .....	131
13 APPENDICES .....	137
Appendix A. Dynamic Component Test Setup Details.....	137
Appendix B. Material Specifications .....	150
Appendix C. FORTRAN Post-Processing Code.....	154
Appendix D. Example “nodes.k” File.....	159
Appendix E. Example of “input.txt” File.....	161

## LIST OF FIGURES

Figure 1. Three Modes of Crack Surface Displacements [5].....	4
Figure 2. Yield and Failure Hypotheses According to SED.....	8
Figure 3. Tensile Stress-Strain Curve at Various Strain Rates for an 8-mm Thick Plate [19] .....	11
Figure 4. Schematic of Peridynamic Representation [41] .....	17
Figure 5. Dimensions of Enlarged Steel Tensile Coupons .....	21
Figure 6. LS-DYNA Material Model Parameters.....	22
Figure 7. Mesh 1 – 4 Elements through the Cross Section with a Close-Up View .....	24
Figure 8. Mesh 2 – 8 Elements through the Cross Section with a Close-Up View .....	24
Figure 9. Mesh 3 – 12 Elements through the Cross Section with a Close-Up View .....	24
Figure 10. Mesh 4 – 16 Elements through the Cross Section with a Close-Up View .....	25
Figure 11. Mesh 5 – 20 Elements through the Cross Section with a Close-Up View .....	25
Figure 12. Internal Energy at the Point of Fracture Initiation.....	30
Figure 13. Cross-Sectional Force at the Point of Fracture Initiation .....	31
Figure 14. Gauge Length Deflection at the Point of Fracture Initiation .....	32
Figure 15. Strain Energy Density at the Point of Fracture Initiation .....	33
Figure 16. Hourglass and Internal Energy for Maximum Plastic Strain Model .....	34
Figure 17. Overall View of Final Version of the Dynamic Tensile Test Configuration .....	38
Figure 18. Rigid-Frame Bogie on Guidance Track .....	39
Figure 19. Two-Tube Steel Coupon Mounting Assembly.....	40
Figure 20. Load Cell and Mounting Assembly.....	41
Figure 21. Gauge Length Grid Data Processing .....	43
Figure 22. Test No. DFS-L1, Pre-Test.....	44
Figure 23. Test No. DFS-L2, Pre-Test.....	45
Figure 24. Test No. DFS-L3, Pre-Test.....	45
Figure 25. Test No. DFS-L3-2, Pre-Test .....	46
Figure 26. Test No. DFS-L4, Pre-Test.....	46
Figure 27. Test No. DFS-L5, Pre-Test.....	47
Figure 28. Test No. DFS-L6, Pre-Test.....	47
Figure 29. Test No. DFS-L7, Pre-Test.....	48
Figure 30. Test No. DFS-T1, Pre-Test.....	48
Figure 31. Test No. DFS-T2, Pre-Test.....	49
Figure 32. Test No. DFS-T3, Pre-Test.....	49
Figure 33. Scaled Stress-Strain Curve of A572 Gr. 50 Steel [59] to Match 0.439 GPa .....	51
Figure 34. Stress-Strain Curve of AASHTO M180 Steel [60] .....	52
Figure 35. Stress-Strain Curve of A1011-12B Gr. 50 Steel .....	53
Figure 36. Force vs. Deflection and Energy vs. Deflection, Test No. DFS-L1 .....	55
Figure 37. Stress vs. Strain, Test No. DFS-L1.....	55
Figure 38. Post-Impact Photographs, Test No. DFS-L1 .....	56
Figure 39. Force vs. Deflection and Energy vs. Deflection, Test No. DFS-L2 .....	57
Figure 40. Stress vs. Strain, Test No. DFS-L2.....	57
Figure 41. Post-Impact Photographs, Test No. DFS-L2 .....	58
Figure 42. Force vs. Deflection and Energy vs. Deflection, Test No. DFS-L3-2.....	60
Figure 43. Stress vs. Strain, Test No. DFS-L3-2 .....	60
Figure 44. Post-Impact Photographs, Test No. DFS-L3-2.....	61
Figure 45. Force vs. Deflection and Energy vs. Deflection, Test No. DFS-L4.....	63

Figure 46. Stress vs. Strain, Test No. DFS-L4.....	63
Figure 47. Post-Impact Photographs, Test No. DFS-L4.....	64
Figure 48. Force vs. Deflection and Energy vs. Deflection, Test No. DFS-L5.....	65
Figure 49. Stress vs. Strain, Test No. DFS-L5.....	65
Figure 50. Post-Impact Photographs, Test No. DFS-L5.....	66
Figure 51. Force vs. Deflection and Energy vs. Deflection, Test No. DFS-L6.....	67
Figure 52. Stress vs. Strain, Test No. DFS-L6.....	68
Figure 53. Post-Impact Photographs, Test No. DFS-L6.....	69
Figure 54. Force vs. Deflection and Energy vs. Deflection, Test No. DFS-L7.....	70
Figure 55. Stress vs. Strain, Test No. DFS-L7.....	71
Figure 56. Post-Impact Photographs, Test No. DFS-L7.....	71
Figure 57. Force vs. Deflection and Energy vs. Deflection, Test No. DFS-T1.....	73
Figure 58. Stress vs. Strain, Test No. DFS-T1.....	73
Figure 59. Post-Impact Photographs, Test No. DFS-T1.....	74
Figure 60. Force vs. Deflection and Energy vs. Deflection, Test No. DFS-T2.....	75
Figure 61. Stress vs. Strain, Test No. DFS-T2.....	76
Figure 62. Post-Impact Photographs, Test No. DFS-T2.....	76
Figure 63. Force vs. Deflection and Energy vs. Deflection, Test No. DFS-T3.....	78
Figure 64. Stress vs. Strain, Test No. DFS-T3.....	78
Figure 65. Post-Impact Photographs, Test No. DFS-T3.....	79
Figure 66. Stress-Strain Curve between Two Nodes.....	84
Figure 67. Schematic of Non-Locality around a Node.....	85
Figure 68. Logarithmic Expressions of Non-Local Critical SED.....	89
Figure 69. Exponential Proportion of the Scaled Failure Parameter.....	90
Figure 70. Internal Energy for Various Delta Magnifiers.....	92
Figure 71. Cross-Sectional Force for Various Delta Magnifiers.....	92
Figure 72. Gauge Length Displacement for Various Delta Magnifiers.....	93
Figure 73. SED for Various Delta Magnifiers.....	93
Figure 74. Convergence Comparison for Internal Energy.....	94
Figure 75. Convergence Comparison for Cross-Sectional Force.....	95
Figure 76. Convergence Comparison for Gauge Length Displacement.....	95
Figure 77. Convergence Comparison for SED.....	96
Figure 78. Force-Deflection Comparisons for A572 Gr 50 Steel without a Hole.....	99
Figure 79. Force-Deflection Comparisons for M180 Steel without a Hole.....	100
Figure 80. Force-Deflection Comparison for A1011-12B Gr 50 Steel without a Hole.....	101
Figure 81. Force-Deflection Comparison for A572 Gr 50 with a Hole.....	107
Figure 82. Force-Deflection Comparison for M180 with a Hole.....	108
Figure 83. Force-Deflection Comparison for A1011-12B Gr 50 with a Hole.....	109
Figure 84. Rail Splice Failures: Quasi Static Tensile Test Results (Left) and TTI Full-Scale Testing Results (Right) [74,75].....	111
Figure 85. Ruptured Rail Installed Over a Curb [76].....	112
Figure 86. Rail Rupture from Quasi-Static Tension Testing at MwRSF [77].....	113
Figure 87. Rail Rupture from 2270P Impact.....	114
Figure 88. Stress-Strain Curves Implemented in LS-DYNA for W-Beam Models.....	116
Figure 89. W-Beam Guardrail Model – Splice Failure.....	117
Figure 90. Force-Deflection and Energy-Deflection Curves for W-Beam Rail Splice.....	117
Figure A-1. Detail of Test Setup.....	138

Figure A-2. Load Cell Assembly and Coupon Mounting Frame.....	139
Figure A-3. Load Cell Assembly Details.....	140
Figure A-4. Coupon Mounting Bracket Details.....	141
Figure A-5. Coupon Mounting Bracket Part Details .....	142
Figure A-6. Part Details for the Load Cell Assembly.....	143
Figure A-7. Anti-Rotation Components of Load Cell Assembly .....	144
Figure A-8. Bolts and Threaded Rod of the Load Cell Assembly.....	145
Figure A-9. Concrete-Filled Tubes Attached to the Bogie Block .....	146
Figure A-10. Enlarged A572 Gr 50 Steel Coupon.....	147
Figure A-11. Detail of Clevis Used to Connect Coupon to Bogie.....	148
Figure A-12. Bill of Materials for Dynamic Component Testing .....	149
Figure B-1. A572 Gr 50 Steel Coupon .....	151
Figure B-2. A1011-12B Gr 50 Thin Steel Coupon.....	152
Figure B-3. AASHTO M180 Steel Coupons .....	153

## LIST OF TABLES

Table 1. Mesh Densities.....	24
Table 2. Summary of Failure Parameters for Mesh 3 .....	28
Table 3. Results of Convergence with Respect to Internal Energy .....	31
Table 4. Results of Convergence with Respect to Cross-Sectional Force .....	32
Table 5. Results of Convergence with Respect to Gauge Length Deflection.....	33
Table 6. Results of Convergence with Respect to Strain Energy Density.....	33
Table 7. Summary of Dynamic Bogie Testing Matrix for Enlarged Steel Coupons .....	36
Table 8. Summary of LS-DYNA Material Input.....	54
Table 9. Summary of Dynamic Tensile Test Results .....	82
Table 10. Exponential Proportion of the Scaled Failure Parameter.....	89
Table 11. Percent Differences between Mesh 2 and Mesh 5 for Each Technique .....	96
Table 12. Post-Processing Parameters for Models with Holes .....	106



## 1 INTRODUCTION

### 1.1 Problem Statement

The components of most steel structures are designed to stay in the linear-elastic range, providing small temporary deformations and an even smaller risk of catastrophic failure. However, rupture is often desirable for some structures. For instance, when the box-beam, bursting, energy-absorbing, single-sided crash cushion (BEAT-SSCC) is struck head-on by an errant vehicle, an extruder is forced through the tube, ripping the tube at the corners [1]. In this event, the material is stressed beyond the elastic range, and after some plastic flow, rupture occurs. The extraordinary energy dissipation, resulting from mobilizing the full spectrum of the material's strength (i.e., primarily from plastic deformation and increased frictional resistance following rupture), can slow down the vehicle at safe occupant ridedown accelerations (ORAs), thus potentially saving a life.

Applying numerical approximations to this example is an arduous task because cracking and crack propagation are the result of dynamic processes. A great number of factors contribute to this initiation and propagation, including inertia effects, nonlinear material properties, and reflecting and interacting stress waves. As a result, most models of fracture are developed after physical testing, where the results of the testing are used to calibrate the model. In the process of research and development, a system that relies on material failure may require numerous physical tests before arriving at the optimized design. If a model existed that could predict the onset of fracture without having to recalibrate it against physical testing for each design change, then the design process could be streamlined through numerical methods before any full-scale test is conducted. However, there is no method that meets this requirement with a computationally-efficient and commercially-available platform.

## **1.2 Research Objectives**

This research focused on the development of a failure model capable of accurately predicting the onset of fracture under dynamic loading conditions. First, mesh dependency was demonstrated in several failure criteria used in the finite element method (FEM). Then, a strain energy density (SED) approach to failure was developed and implemented in a post-processor over a non-local area of influence, described by a length scale. With this length scale, a critical SED to initial fracture, a material property, was determined from tensile test data. Finally, this process was repeated for various configurations and materials to predict the force-displacement curves prior to conducting physical tests.

## **1.3 Research Plan**

This project focused on applying and evaluating a non-local SED failure criterion to predict only the onset of fracture in steel. Model validation was limited to tensile coupon testing using three common steel alloys. Comparisons between models and tests were conducted using force-displacement curves, or more specifically, the areas under those curves, representing the total energy in the coupon through the elastic and plastic ranges up to fracture initiation. Testing and modeling were applied to coupons with varying thicknesses. Finally, a stress concentration was included in some of the coupons to determine the model's effectiveness in handling geometric obscurities without recalibration.

## 2 LITERATURE REVIEW

### 2.1 Fracture Mechanics

#### 2.1.1 Griffith Theory

In a paper published in 1924, Griffith proposed an energy-based approach to predicting the behavior of a crack [2]. He postulated that the amount of energy required to grow a crack was proportional to the area of the new crack surface. He also observed that rupture stresses were less than 10% of the theoretical value determined by his energy approach, and the energy for rupture was less than 1% of the theoretical value [3]. He deduced that this was caused by heterogeneity in the material microstructure, severe initial stresses in the material, or the formation of small cracks during or after manufacture.

Irwin developed an approach that essentially mirrored Griffith's energy approach, but he did so in a way that made it more convenient for engineering problems [4]. Irwin developed a term that would become known as the energy release rate, which he described as the "crack extension force tendency" [4]. The energy release rate is the derivative of the potential energy supplied by internal strain energy and external forces with respect to the surface area of a crack surface [3]. The general equation for the energy release rate is given below:

$$\mathcal{G} = -\frac{d\Pi}{dA} \quad (2.1)$$

Where  $\mathcal{G}$  = energy release rate  
 $\Pi$  = potential energy  
 $A$  = surface area of the crack

#### 2.1.2 Linear-Elastic Fracture Mechanics

Linear-elastic fracture mechanics (LEFM) is primarily defined by the use of a stress intensity factor for determining crack extension [5]. It also assumes that a flaw or crack already

exists in the material, and that the nonlinear zone immediately in front of the crack tip is negligible, which is not entirely true for ductile metals [6]. Most concepts of fracture mechanics prior to 1960 applied only to linear-elastic materials [3]. There are three basic stress systems or modes near a crack tip, as shown in Figure 1 [5].

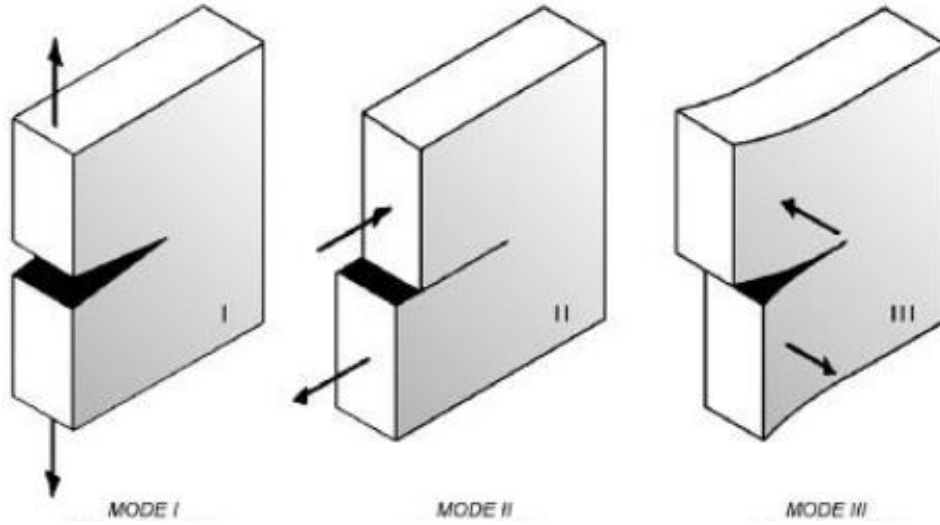


Figure 1. Three Modes of Crack Surface Displacements [5]

The stress intensity factor was introduced by Irwin in the 1950s and was developed in response to the difficulty in implementing Griffith's energy approach [1,7]. Irwin found that the stress field in the vicinity of a crack tip took the form below [1]:

$$\sigma_{ij} = \frac{K}{\sqrt{2\pi r}} f_{ij}(\theta) + \dots \quad (2.2)$$

Where

- $K$  = stress intensity factor =  $\sigma\sqrt{\pi a} \cdot f(a/W)$
- $r, \theta$  = cylindrical coordinates of a point with respect to the crack tip
- $a$  = half the crack length
- $f(a/W)$  = parameter based on the geometries of the specimen and crack
- $\sigma$  = remotely applied stress (differs from  $\sigma_{ij}$ )

The stress intensity factor and the energy release rate are related, and this relationship is demonstrated by using a wide plate with a center cut. The energy release rate and stress intensity factor for this case are given below. Note that  $f(a/W) = 1$  for a wide plate with a central crack of length  $2a$  and Mode I loading [5].

$$\mathcal{G} = \frac{\pi\sigma^2 a}{E} \quad (2.3)$$

$$K = \sigma\sqrt{\pi a} \quad (2.4)$$

Where  $E$  = Young's modulus

By solving for the remotely applied stress in each of the above equations and setting them equal, the Mode I stress intensity factor can be related to the energy release rate according to the below equation, which has been shown to be valid for any geometry [1]:

$$\mathcal{G} = \frac{K^2}{E} \quad (2.5)$$

### 2.1.3 Elastic-Plastic Fracture Mechanics

#### 2.1.3.1 J Integral

A path-independent integral was developed by Rice in 1968 that was able to bypass the detailed solutions of boundary-valued problems [8]. This “J Integral” represents a constant value for any possible path from one side of a crack to the other. The J Integral is related to the strain energy density, components of the traction and displacement vectors, and the incremental length along the arbitrary contour, as shown in the equation below. The J Integral is a more general form of the energy release rate, and for linear-elastic material,  $J = \mathcal{G}$  [3].

$$J = \int_{\Gamma} \left( w dy - T_i \frac{\partial u_i}{\partial x} ds \right) \quad (2.6)$$

Where  $\Gamma$  = curve surrounding the crack tip  
 $w$  = strain energy density =  $\int_0^{\varepsilon_{ij}} \sigma_{ij} d\varepsilon_{ij}$   
 $T_i$  = components of the traction vector =  $\sigma_{ij} n_j$   
 $u_i$  = components of the displacement vector  
 $ds$  = incremental length along  $\Gamma$

### 2.1.3.2 Crack-Tip-Opening Displacement (CTOD)

Wells observed that steel materials were too tough and exhibited too much plasticity to be analyzed with the LEFM method [9]. Following the testing of steel samples, he observed that the crack surfaces moved apart from one another, and that plastic deformation blunted the sharp end of the crack. The magnitude of that blunting was a function of the toughness of the material, leading to the development of a crack-tip-opening displacement parameter (CTOD) used to predict the opening of a crack as a function of the materials toughness.

### 2.1.4 Strain Energy Density

Strain energy is the energy absorbed by a material during deformation caused by a loading process. Because of the principle of energy conservation, the strain energy is the work done by the load, assuming no loss of energy in thermal processes, and is equal to the area under the force-displacement curve [10]. This principle can be illustrated by Equation 2.7:

$$U = \int_0^x F(x) d\delta \quad (2.7)$$

Where  $U$  = strain energy  
 $F(x)$  = force as a function of the displacement  
 $x$  = displacement

The total strain energy is dependent on the volume of the material, in that a larger object would require more energy than a smaller object at the same displacement. Thus, the strain energy density becomes a more general, and therefore, useful tool. The strain energy density (SED) is the strain energy per unit of volume [10] and can be described according to the area under the stress-strain curve, as in Equation 2.8.

$$u = \int_0^{\varepsilon} \sigma d\varepsilon \quad (2.8)$$

Where  $u$  = strain energy density  
 $\sigma$  = stress  
 $\varepsilon$  = strain

Sih proposed a failure criterion in response to the need to predict crack growth in mixed-mode applications in a simple and unified manner [11-13]. First, he related the SED to a strain energy density factor,  $S$ , and the radial distance measured from the point of possible fracture initiation,  $r$ , as in Equation 2.9.

$$u = \frac{S}{r} \quad (2.9)$$

Where  $u$  = the strain energy density (in Sih's notation,  $u = dW/dV$ )  
 $S$  = the SED factor  
 $r$  = the radial distance measured from the fracture location

Three hypotheses govern the SED failure criterion proposed by Sih [14] and can be schematically thought of as in Figure 2:

1. The location of fracture coincides with the location of relative minimum strain energy density,  $u_{min}$ , and yielding with relative maximum strain energy density,  $u_{max}$ .

2. Failure by fracture or yielding occurs when  $u_{min}$  or  $u_{max}$  reach their respective critical values.
3. The crack growth increments  $r_1, r_2, \dots, r_j, \dots, r_c$  during stable crack growth satisfy the equation

$$u_c = \frac{s_1}{r_1} = \frac{s_2}{r_2} = \dots = \frac{s_j}{r_j} = \dots = \frac{s_c}{r_c} \quad (2.10)$$

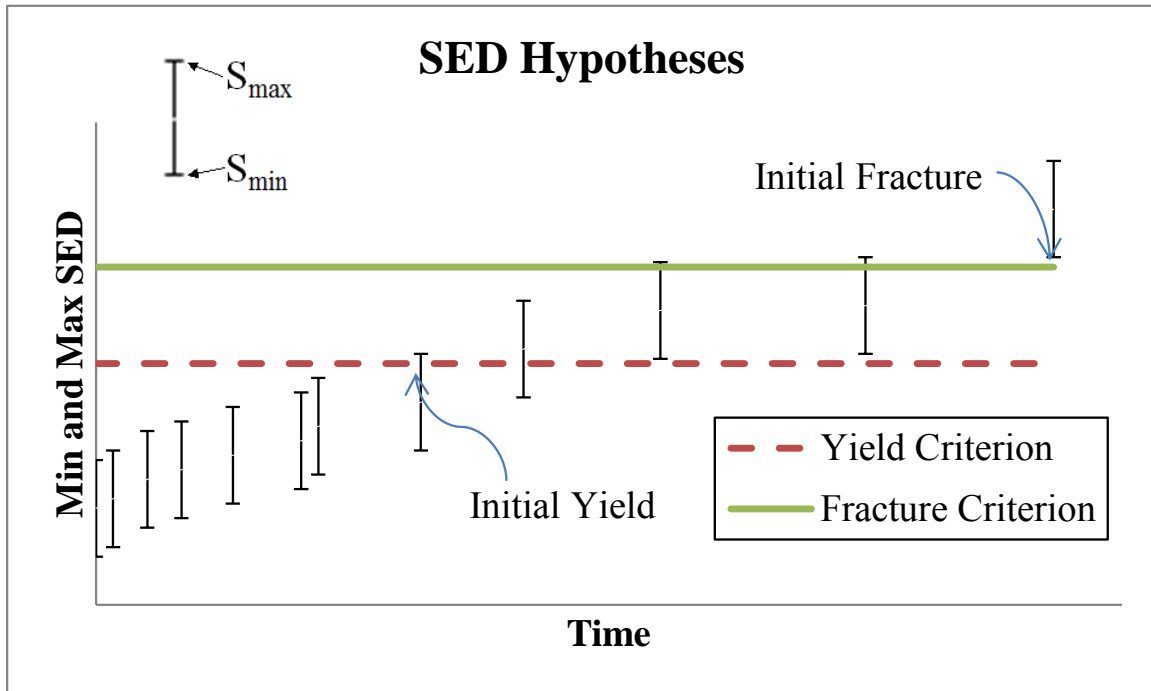


Figure 2. Yield and Failure Hypotheses According to SED

Sih then related the SED factor to the stress intensity factor,  $K$  [15], which, by 1974, was a well-established technique for modeling linear-elastic fracture. For a comparison, he looked at samples with pre-existing cracks, such as a through-crack in a plate subject to uniaxial tension. He provided the following definition of the SED:



$$SED = \frac{1}{r} (a_{11}k_1^2 + 2a_{21}k_1k_2 + a_{22}k_2^2 + a_{33}k_3^2) + \dots \quad (2.11)$$

where the coefficients for plane strain are given by:

$$a_{11} = \frac{1}{16\mu} [(3 - 4\nu - \cos \theta)(1 + \cos \theta)] \quad (2.12)$$

$$a_{12} = \frac{1}{16\mu} (2 \sin \theta) [\cos \theta - (1 - 2\nu)] \quad (2.13)$$

$$a_{22} = \frac{1}{16\mu} [4(1 - \nu)(1 - \cos \theta) + (1 + \cos \theta)(3 \cos \theta - 1)] \quad (2.14)$$

$$a_{33} = \frac{1}{4\mu} \quad (2.15)$$

Where  $\nu$  = Poisson's ratio  
 $\mu$  = shear modulus of elasticity  
 $k_i = K_i/\sqrt{\pi}$ ,  $i = 1, 2, \text{ or } 3$   
 $K_i$  = stress intensity factor for Mode  $I$   
 $\theta$  = angle with respect to direction of crack

### 2.1.5 Dynamic Loading and Fracture

Dynamic fracture mechanics is concerned with the fracture caused by impact loading or with unstable crack propagation. Classical LEFM was developed for linear-elastic materials under quasi-static loading conditions. Generally, three complicating issues arise when dealing with dynamic effects [3]: (1) inertia forces, (2) rate-dependent material behavior, and (3) reflected stress waves. Reflected stress waves are of particular importance because as new surfaces are created through crack initiation and propagation, the reflecting stress waves will influence the stress at the crack tip [3]. Elastodynamic fracture mechanics are the LEFM equivalent for dynamic applications and can typically account for inertia effects and reflected stress waves, but often neglect nonlinear material behavior [3]. The incorporation of nonlinear, time-dependent material behavior into

elastodynamic fracture mechanics is a relatively new innovation and typically generalizes the J integral to account for inertia and viscoplasticity [3].

Multiple numerical approximations have been developed to model dynamic fracture mechanics. In 1985, Atluri and Nishioka published a paper summarizing advances in numerical approximations of dynamic fracture [16]. In a study published eight years prior, Kanninen found that the finite element method was ill-suited for dynamic crack propagation [17], but significant computational advances were made in a very short period of time [16]. The finite element method was applied using both stationary mesh and moving mesh procedures. When using a stationary mesh, the location of the crack tip advances from one node to the next over the time step. For a moving mesh, as implied by the name, the mesh moves with the crack tip. However, this approach cannot be applied to bodies with finite dimensions in the direction of crack propagation.

Aminjikai and Tabiei utilized the explicit time integration scheme of DYNA3D and brick elements to model mixed-mode crack propagation [18]. The explicit nature of the code allowed them to apply the mechanics to large-scale simulations. They proposed an element-deletion-and-replacement method, but noted that instantaneous crack growth resulting from element deletion sends high-frequency oscillations through the solution. To overcome this problem, the authors applied a restraining force over a series of sub-increments between nodes, such that instead of the element's resistive power instantly going to zero, it gradually tended toward zero.

## **2.2 Behavior of Steel**

Mild steel can experience variations in its constitutive relationships as the strain rate varies. Strain rates ranging from  $10^{-4} \text{ s}^{-1}$  to  $10^3 \text{ s}^{-1}$  were applied to a mild steel of grade St52-3N, which has a carbon content of 0.12 percent by weight, and the ultimate stress was shown to increase almost linearly with the logarithm of the strain rate [19]. The stress-strain curves at various strain rates applied to a thin plate are shown in Figure 3. This study highlights the fact that the effect of

strain rate is limited in the range of typical roadside safety applications. The ultimate stress in the plate at a strain rate of  $1070 \text{ s}^{-1}$  was approximately the same as when a strain rate of  $21.4 \text{ s}^{-1}$  was used.

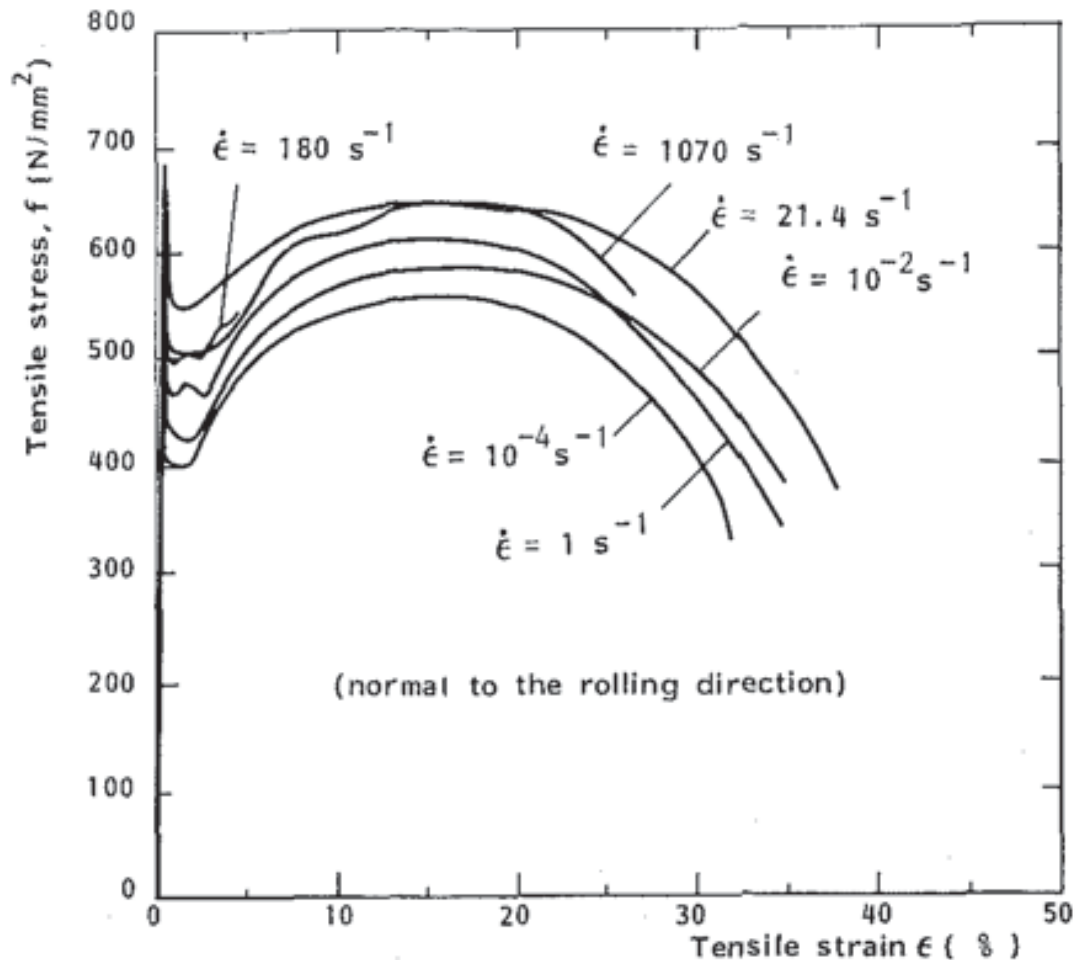


Figure 3. Tensile Stress-Strain Curve at Various Strain Rates for an 8-mm Thick Plate [19]

### 2.3 Local Fracture Modeling Techniques

Local models characterize the behavior of a model by examining each point within the discretized continuum. For example, at any given time, the strain in a single element is correlated to the stress in that element. There are many techniques that use this approach. The FEM is not inherently local, but most commercial applications of the method utilize local discretizations in

their calculations. Extensions or modifications to the local FEM include cohesive zone models (CZM), overlapping tied shells, and the extended finite element method (XFEM).

### **2.3.1 Element Deletion**

The FEM is a numerical approximation used to solve complex partial differential equations for complex shapes [20]. The method's name is derived from the process by which a shape is discretized into elements connected by nodes. Partial differential equations are solved for each element, providing an approximate solution for stress analysis, heat flow, fluid flow, and electromagnetics [20].

A simple approach to fracture modeling via local FEM is element deletion. This approach does not require special consideration of discontinuities because of the local nature of each element [21]. In other words, cracks do not exist anywhere except on the boundaries of elements. Elements are not literally deleted, but the stress in the element is set to zero [21]. Because the energy release rate is dependent on the area or volume of the deleted element, mesh dependency plays an integral role in this approach [21]. Additionally, the orientation of the elements with respect to each other dictates the path of the crack and, as a result, may produce significant error in the simulated solution unless the mesh geometry is aligned with the crack, as determined from physical testing [22]. This dependency removes the possibility of predicting crack propagation.

### **2.3.2 Tied Nodes with Failure**

A body can be discretized with independent, separate shells or bricks, where the nodes that define the element share space with other nodes belonging to other elements. The group of nodes occupying the same space can be grouped together and held in such manner until a user-specified, plastic volumetric strain,  $\varepsilon_{vpl}$ , is reached at the location of the nodes [26]. At this point, the nodes are released from one another. In so doing, mass loss is avoided, but crack propagation is still firmly rooted in the orientation of the mesh.

### **2.3.3 Cohesive Zone Models (CZM)**

The CZM was originally formulated by Hillerborg to simulate the behavior of concrete and circumvent some of the limitations of the LEFM [27]. It assumes that as a crack opens, for small openings, forces can still be transmitted across the crack, thus requiring energy to overcome these forces and propagate the crack.

A softening function is considered a material property for a cohesive zone model [6]. This function is primarily defined by two properties: (1) the tensile strength at which the crack initiates and begins to open, and (2) the cohesive fracture energy supplied by an external force that creates a unit surface area crack and is described as the area under the softening function.

If the mesh size is small enough and cohesive zone elements are placed everywhere, *a priori* knowledge of the crack initiation and path are not needed [28]. However, for practical mesh sizes in large-scale simulations, the computational expense of cohesive elements restricts their use to the area around the crack, where the mesh would be sufficiently refined. This implies that *a priori* knowledge is required for large-scale models, thus eliminating this technique's predictive capabilities [29]. Additionally, this method is not capable of modeling multiple crack paths or crack branching [30] and requires a pre-crack in the material in order to function properly.

### **2.3.4 Overlapping Tied Shells**

This technique was developed to capture realistic behavior of polymer parts on a vehicle in the event of a crash [22]. It was adapted to LS-DYNA for particular use in simulating full-scale models. It uses the simple approach of element deletion and does not require remeshing. In essence, an object is modeled with two parts, each of which is discretized with shell elements. The technique is characterized by the use of regular tetragon shell elements, with the mesh of one part rotated 45 degrees with respect to the other part. Finally, the two parts are connected with a tied contact, \*CONTACT\_TIED\_SHELL\_EDGE\_TO\_SURFACE\_BEAM\_OFFSET [31]. Ultimately, crack

propagation is still mesh-dependent, but this technique reduces that dependency significantly. The results of the polymer simulation matched physical testing well in crack initiation, crack path, and force necessary to propagate the crack [22]. Similarly, crack initiation and path were modeled well in the windshield of a vehicle undergoing deformation in its A-pillar. However, force levels in the model were lower than in the physical test, prompting the authors to recommend further study of the technique [31].

### **2.3.5 Extended Finite Element Method (XFEM)**

To model a meandering crack with finite elements, the mesh must be aligned with the geometry of the crack. The extended finite element method (XFEM) was developed in response to this cumbersome practice [32]. The traditional finite element solution, using the summation of nodal displacements and shape functions, must be modified at the node or nodes that may experience a discontinuity. A jump function is added to a node near the crack but away from the crack tip, and to model an entire crack, asymptotic crack tip functions are added to nodes around the crack tip [32]. The incorporation of the additional functions was accomplished using the partition of unity method, which ultimately allowed for crack growth without requiring the user to remesh the model.

However, as with the local FEM, the divergence of the stress field is used to describe the equations of motion [33]. Therefore, as indicated previously, exceptions to the equation of motion must be implemented at the discontinuity because the divergence of the stress field is undefined.

Additionally, XFEM has been used to model dynamic fracture using the loss-of-hyperbolicity criterion, or the point at which the tangent modulus loses its positive slope, and the level set method [34]; however, it was not able to model multiple cracks or crack branching [30].

### **2.3.6 LS-DYNA**

LS-DYNA is produced by Livermore Software Technology Corporation (LSTC), which is located in Livermore, CA. The code is generally used for large deformations and dynamic responses, particularly in the field of impact engineering, and it utilizes explicit time integration [23]. Element deletion, CZM, overlapping tied shells, and XFEM can be used in LS-DYNA [22-25], although XFEM has only recently been added and may not be practice-ready at the moment.

Element deletion is incorporated in material models, such as \*MAT\_024 (\*MAT\_PIECEWISE\_LINEAR\_PLASTICITY), where the “FAIL” parameter is set to a negative number for a user-defined failure subroutine or positive for plastic strain to failure [26].

Numerous failure criteria can be defined and applied to any material by including \*MAT\_ADD\_EROSION in the model. Of particular interest are failure definitions for maximum principal strain and maximum shear strain.

LS-DYNA also enables its users to create their own material models, which can incorporate failure [26]. Constitutive equations can be developed any way the user chooses, and similarly, an existing material model with a user-defined failure subroutine can be used [24].

## **2.4 Non Local Fracture Modeling Techniques**

Nonlocal methods were developed in part to investigate the effect of the microscopic material structure on the macroscopic material behavior [35]. Among the more commonly used non-local techniques are molecular dynamics (MD) and peridynamics.

### **2.4.1 Molecular Dynamics**

Molecular dynamics was developed in the 1950s and 60s to solve Newton’s equations of motion between atoms and molecules using molecular force fields [36-37]. Each molecule is treated as a point mass, subject to Newton’s laws of motion, but the time step required in this

method is substantially small [38]. Therefore, using MD at any practical engineering scale would require unreasonable computational time.

### 2.4.2 Peridynamics

In the theory of peridynamics, the partial differential equations used in the classical theory of solid mechanics were replaced by integro-differential equations [39]. As a result, the theory is ideally suited for fracture, particularly in problems where the crack location is unknown [40]. The original peridynamic equation of motion is given below [39-40], where bold terms represent vectors, and applicable terms are illustrated in Figure 4 [41]:

$$\rho(\mathbf{x})\ddot{\mathbf{u}}(\mathbf{x}, t) = \int_{\mathcal{H}} \mathbf{f}(\mathbf{u}(\mathbf{x}', t) - \mathbf{u}(\mathbf{x}, t), \mathbf{x}' - \mathbf{x}) dV_{\mathbf{x}'} + \mathbf{b}(\mathbf{x}, t) \quad (2.16)$$

Where

$\rho(\mathbf{x})$  = mass density

$\mathbf{u}(\mathbf{x}, t) = \mathbf{u}$  = displacement vector

$\mathbf{u}(\mathbf{x}', t) = \mathbf{u}'$  = displacement vector of a neighboring point

$\mathbf{x}$  = position vector

$\mathbf{x}'$  = position vector of a neighboring point

$t$  = time

$\mathbf{f}(\boldsymbol{\eta}, \boldsymbol{\xi})$  = pairwise force function for all bonds,  $\boldsymbol{\xi}$ , and relative displacements,  $\boldsymbol{\eta}$

$\mathbf{b}(\mathbf{x}, t)$  = prescribed body force density

$V_{\mathbf{x}'}$  = volume around the position vector of a neighboring point

$\boldsymbol{\xi} = \mathbf{x}' - \mathbf{x}$

$\boldsymbol{\eta} = \mathbf{u}' - \mathbf{u}$

$\mathcal{H}$  = integration region around  $\mathbf{x}$  with radius =  $\delta$

$\delta$  = peridynamic horizon of the material



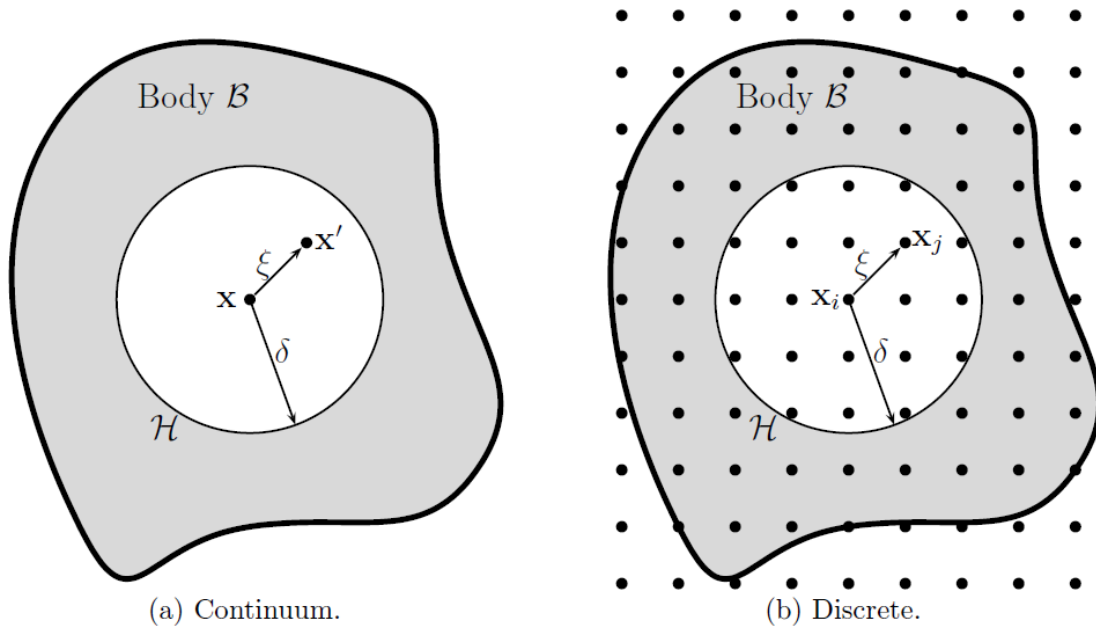


Figure 4. Schematic of Peridynamic Representation [41]

### 2.4.3 Coupling FEM and Peridynamics

Due to the non-local nature of peridynamics, implementation of its theory can lead to computationally expensive models. However, its efficiency can be dramatically improved when coupled with the local FEM. A study was done to model the penetration of a projectile through a steel plate using ABAQUS, peridynamics (via EMU, a numerical code developed specifically to discretize the peridynamic equations), and a coupled form of the two [52]. The square aluminum plate was 9.8 in. (250 mm) to a side and 0.5 in. (12.5 mm) thick. The impacting ball was 2 in. (50 mm) in diameter and weighed 11.3 lb (5.11 kg). The model used 50,000 nodes in its grid spacing and approximately 2.4 million bonds in the EMU model. The model was also simulated with a coupled model that used 1,200 conventional continuum elements, 12,500 peridynamic nodes, and 670,000 trusses that were embedded in the continuum elements and represented the peridynamic bonds described previously. EMU required 283 minutes of wall-clock time to complete the simulation, whereas ABAQUS required 73 minutes. Even more interesting, when peridynamics

was coupled to the local FEM code, the wall-clock time was reduced even more to 27 minutes. The embedded trusses carry forces according to the constitutive modeling relationships of the peridynamic theory, and the sum of the forces in the trusses connected to a node are used to describe the motion of that node, according to the peridynamic equation of motion [53].

Another study done by Beckmann et al. incorporated trusses in the model to represent the bond between two nodes [54]. The behavior of each bond was controlled by a quasi-force-stretch constitutive relationship, where the truss was set to fail at a prescribed critical stretch, as determined from the critical energy release rate, the horizon radius, and the bulk modulus.

Another approach to couple the two theories is to divide the body into two domains, one with finite elements and one with collocation points that are connected within a horizon [55]. Each collocation point is described by a hexahedral subdomain and uses eight integration points. The two domains overlap in a region where the properties of the finite elements are effectively voided, but their presence dictates displacement boundary conditions for use in the peridynamic regions.

A third method of coupling involves submodeling [56-57]. Essentially, two separate models are simulated, with the first being a local FEM model. This first model is simulated under the assumption that the body remains continuous. Then, if the development of a crack in a specific region is expected, that region would be cut out of the local FEM model, and the displacements from that model would be used in the submodel. For this to work, the effect of the crack on the overall displacement must be negligible. If this is the case, then the displacement boundary conditions can be applied to the peridynamic model (EMU) of the cut-out region, and the second or sub-model can be simulated. However, *a priori* knowledge of the crack location is required, which negates one of the most attractive features of peridynamics.

### **3 RESEARCH APPROACH AND METHODOLOGY**

To accomplish the objectives of this research, a series of tasks were completed to create a new model for failure prediction in the material based on a non-local strain energy density criterion. In addition to generating this new model, physical tests were carried out to validate the model results, providing confidence in the results.

First, the strain energy density (SED) that was required to initiate fracture for an enlarged steel coupon was estimated from a dynamic uniaxial tension test. This SED was derived from stress-strain data taken from quasi-static tensile data found in literature. Later, dynamic tensile tests were conducted wherein the forces used to calculate stresses were recorded by load cell transducers, and the deflection data used to calculate strains was collected via high-speed video analysis. These dynamic tests were used to validate the non-local SED model.

The coupon was then modeled with five different mesh densities, employing shell elements in LS-DYNA. First, well-established failure models (maximum principle strain, maximum plastic strain, maximum shear strain, and constrained tied nodes with failure) were applied to the five meshes, and one of the five meshes was fine-tuned for each failure technique until modeled results matched physical test results. These fine-tuned material models were applied to the remaining meshes. Then, the approximated solution for the SED at the onset of fracture was plotted against the number of shell elements through the cross section to observe the mesh sensitivity of each of these techniques.

Each mesh was then simulated with a piecewise linear plasticity material model (\*MAT\_024 in LS-DYNA), wherein failure was set to unrealistically high strains. In the process, the displacement of every node was recorded for post-processing. Next, the nodal output was analyzed via a FORTRAN code developed by the author, wherein a non-local SED failure criterion was implemented. This implementation included determining the coarsest mesh that provided a

converged solution, the non-local length scale required to reduce mesh sensitivity, and the critical SED over the non-local area surrounding a point. This final requirement was completed by empirically deriving a magnification factor of the critical global SED of the material based on a length scale large enough to include a sufficient number of nodes in the calculations.

With the established non-local length scale and critical SED for high-strength steel, the physical testing phase was repeated for a thinner coupon, and the model was adjusted by thinning the shell sections. The model was used to predict the force-displacement curve of the thinner coupon prior to conducting the test. Similarly, a model was created for AASHTO M180 steel sheet metal (used in standard W-beam guardrail). The critical SED was determined from quasi-static tensile testing taken from literature. It was then used to predict force-displacement curves up to fracture for various steel coupons with different dimensions.

Finally, a stress concentration was added to some coupons, and the LS-DYNA model was adjusted accordingly. In combination with reduced thicknesses, this addition was made to study the effect of geometric changes on the SED failure criterion. If the model accurately predicted fracture, then it could be concluded that recalibration is not required for geometric changes in the part.

Crack propagation modeling was not possible at this time but may be included in the future. The current research effort predicts the onset of fracture for a steel tensile sample based on video evidence from dynamic component testing. Therefore, once a point of fracture initiation has been identified, the remainder of the simulation no longer represents physics. Results of the analysis, up to the point of fracture initiation, were compared to the physical test results. This comparison was made with force-displacement curves, effectively comparing the energy required to deform and fracture the steel.

## 4 MESH SENSITIVITY OF EXISTING TECHNIQUES

### 4.1 Parametric Model Description

The enlarged steel coupon shown in Figure 5 was discretized with shell elements using five differing mesh densities. For the mesh sensitivity study, the coupon was  $\frac{5}{16}$  in. (8 mm) thick. The coupon was divided into two parts, where the first part included the square tabs on each side of the coupon. The density of shell elements along the outside edges was controlled by the density of the shell elements through the critical section. However, the mesh density around the bolt hole was very fine, and remained unchanged for each mesh. This fine mesh was used so that the contact between the coupon and the rigid cylinders represented pinned connections without large penetration errors, which would lead to unstable models via shooting nodes around this bolt hole.

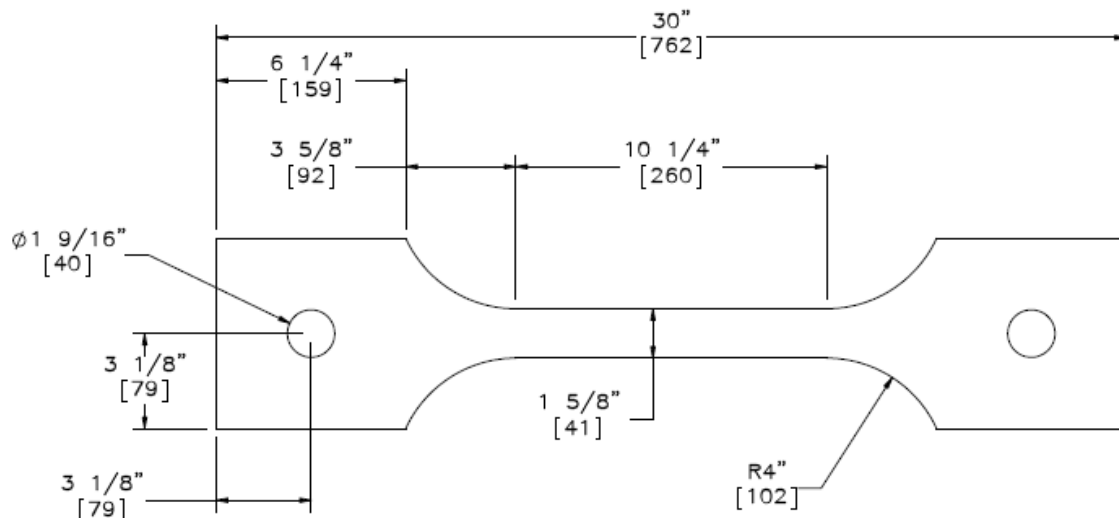


Figure 5. Dimensions of Enlarged Steel Tensile Coupons

Additionally, a rigid cylinder was placed through each of the bolt holes. One cylinder was fixed in space in all three directions, while the other was prescribed a constant motion of 22.4 mph (10 mm/ms) with a linear ramp-up time of 0.1 ms. Contact between each cylinder and the coupon was modeled using an automatic, one-way, surface-to-surface algorithm using a segment-based

penetration check to compute contact stiffness ( $\text{SOFT} = 2$ ). The material was modeled with \*MAT\_PIECEWISE\_LINEAR\_PLASTICITY, where seven data points were used in the material card and are shown in Figure 6. These data points were tabulated and included in the figure. The effective plastic strains (EPS) were shown on the x-axis of the plot and the effective or true stresses (ES) were shown on the y-axis. EPS were taken from values reported in literature [59], and ES were scaled from that reported data such that the yield stress matched the material certificate of conformity given in Appendix B.

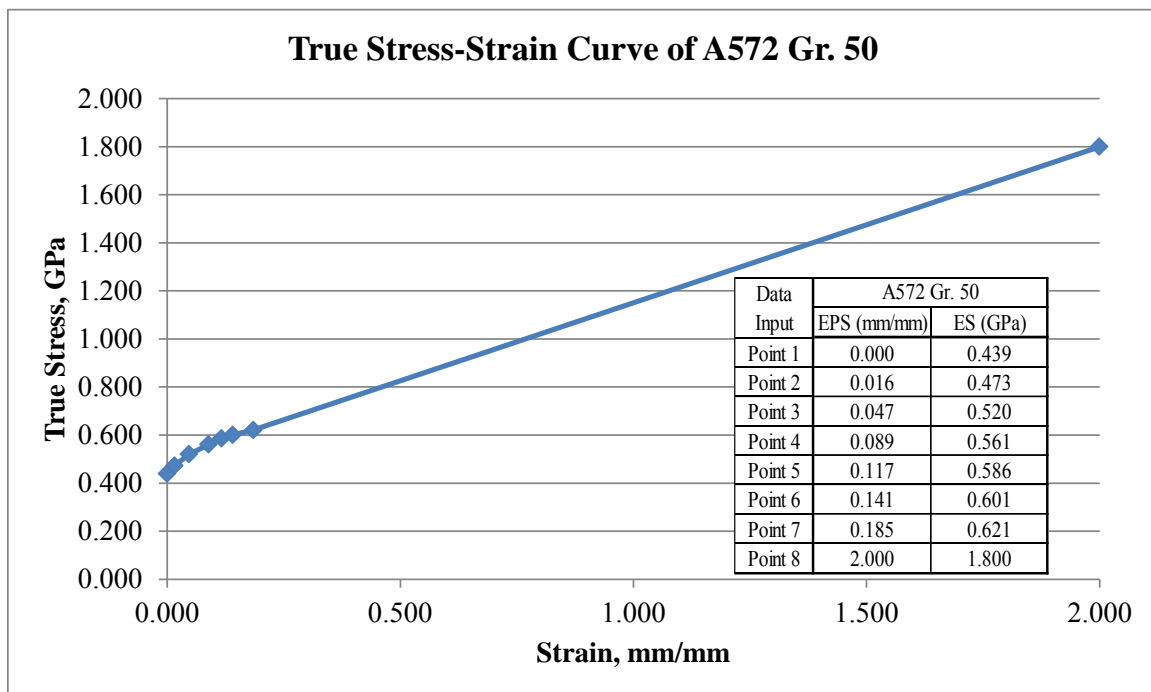


Figure 6. LS-DYNA Material Model Parameters

In general, quadrilateral shell elements were used wherever possible. However, in some regions, triangular shell elements were required to fit around curved edges or holes. Also, the transition region from reduced-width to maximized-width required triangular shells. This prompted the use of the input card \*CONTROL\_SHELL, which governs the behavior of all shell elements unless specifically adjusted with individual section cards. Of particular note, this card

contains a parameter to sort elements and treat degenerate quadrilateral shells as triangular C0 elements. If this card is omitted, the default for the sorting parameter is turned off. Therefore, since triangular elements are present in all meshes, the ESORT parameter was set to 1, providing full sorting for C0 triangular elements.

Another common feature among all models contained herein is the number of integration points analyzed through the thickness of the elements. By default, these calculations are performed using Gaussian integration over 2 points. In general, more Gauss points roughly equates to a more accurate solution. However, there is a point where adding an additional Gauss point does not significantly improve the results of the model. In many ways, this is similar to determining the density of the mesh that provides a stable and accurate solution. However, this additional study was not done to determine the minimum number of Gauss points that provide an accurate solution, since the time savings in the calculations would be negligible. Therefore, the default value of 2 was replaced by 5 integration points for all models.

Another default parameter that required adjustment was the shear correction factor, which by default is 1.0. The LS-DYNA keyword manual recommends a value of  $\frac{5}{6}$  for isotropic materials [26], and as such, this value was adopted for all models.

The densities of the five meshes were approximately controlled by establishing the number of shell elements through the critical width of the coupon, namely 4, 8, 12, 16, and 20 elements. The mesh densities used in the critical sections are summarized in Table 1, and a graphical depiction of each density is given in Figures 7 through 11. A close-up view of the critical cross-section is included in these figures. To create these coupons, two parts were generated and duplicate nodes were merged. The interior part was considered the critical section, and it was this part that determined the number of shells and nodes reported in Table 1.

Table 1. Mesh Densities

Mesh	Shells through Cross Section	Total Shells	Total Nodes
1	4	243	308
2	8	1,012	1,141
3	12	2,222	2,318
4	16	3,771	4,029
5	20	5,978	6,300

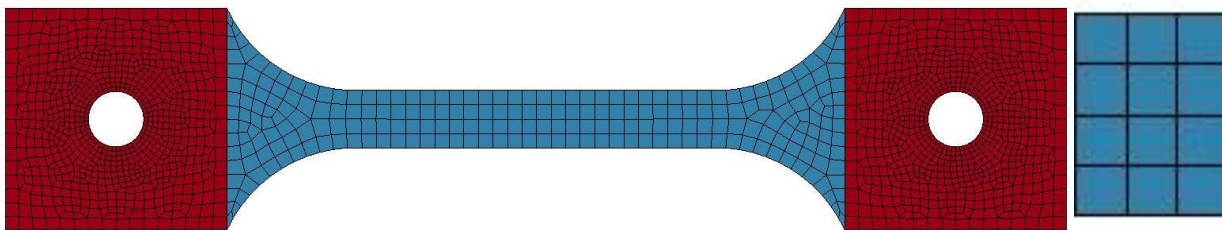


Figure 7. Mesh 1 – 4 Elements through the Cross Section with a Close-Up View

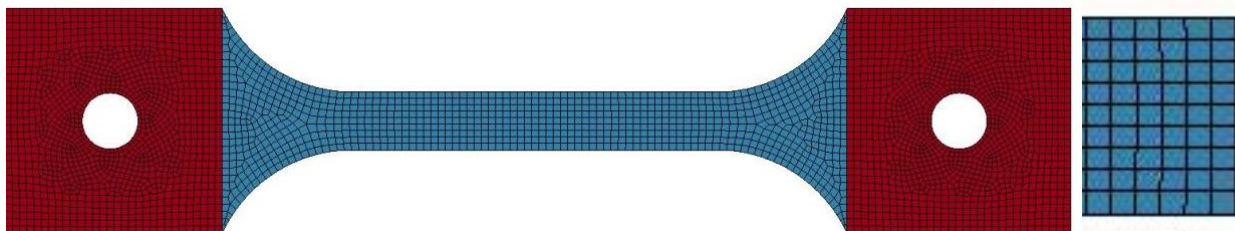


Figure 8. Mesh 2 – 8 Elements through the Cross Section with a Close-Up View

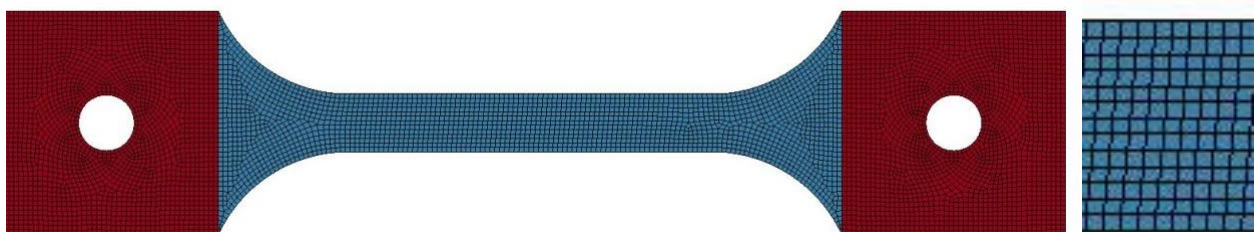


Figure 9. Mesh 3 – 12 Elements through the Cross Section with a Close-Up View



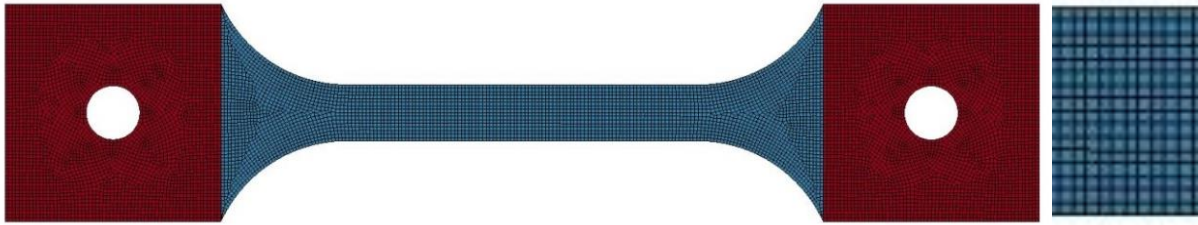


Figure 10. Mesh 4 – 16 Elements through the Cross Section with a Close-Up View



Figure 11. Mesh 5 – 20 Elements through the Cross Section with a Close-Up View

Each of these mesh densities was used to model failure in well-established techniques available in LS-DYNA. Eight failure criteria or modeling techniques suited to cracking were identified and included maximum plastic strain, tied nodes with failure, maximum principal strain, maximum shear strain, cohesive zone models (CZM), extended finite element method (XFEM), smoothed particle hydrodynamics (SPH), and tied overlapping shells. However, CZM requires a discontinuity, such as a crack tip, to work and was excluded from further consideration. XFEM has only recently been implemented in LS-DYNA and suffers from implementation complications, possibly related to the version of LS-DYNA used in this study, thus eliminating it from the current investigation. SPH models go unstable almost immediately when tension is applied, and it was excluded. Finally, the tied overlapping shells technique presents jagged edges where the shells are rotated, and as a result, stress concentrations develop in erroneous locations. Until a pre-processor can more adequately mesh a part with overlapping shells, this technique cannot be used and was thus excluded. This left four failure criteria to investigate: (1) maximum plastic strain, (2) tied nodes with failure, (3) maximum principal strain, and (4) maximum shear strain. First, the failure

criterion for each of these four approaches was adjusted in mesh 3 from Table 1 or Figure 9 until the modeled results matched physical results. For example, the maximum plastic strain was adjusted by trial-and-error until the initiation of fracture (element deletion, in this case) matched the test results. Then, the same value for the failure parameter was used in the two coarser meshes (mesh 1 and 2) and two finer meshes (mesh 4 and 5). Finally, the force-deflection curve up to failure and the SED at failure were recorded for all five meshes and plotted against the number of elements through the cross section of the model. The deflections were measured from the outside edges of the coupon to provide a precise and consistent point of comparison between all models. The force was taken from a cross-section force recorded in the ASCII files and read by the post processor. The engineering stress was calculated by dividing the cross-section tension force by the initial cross-sectional area. Finally, the strain was calculated by dividing the displacement in the critical section (not the overall displacement mentioned previously) by the original gauge length between the two points used in the analysis. The SED at fracture was determined by integrating the stress-strain curve and locating the SED at the correct strain, correlating with the predicted time of fracture.

Quasi-static stress-strain data for A572 Gr. 50 steel was available from literature and was used to calibrate each model. This data is shown in Figure 6. Integration of this curve was accomplished via the trapezoidal rule, according to Equation 4.1, and the resulting strain energy density used for calibrating the models was 21.0 ksi (145 MPa).

$$SED = \int_0^{\varepsilon_f} \sigma(\varepsilon) d\varepsilon \approx \sum_{i=1}^n \frac{\sigma(\varepsilon_i) + \sigma(\varepsilon_{i-1})}{2} \cdot (\varepsilon_i - \varepsilon_{i-1}) \quad (4.1)$$

Where  $SED$  = Strain Energy Density  
 $\varepsilon_f$  = failure strain of the material  
 $\sigma(\varepsilon)$  = stress curve as a function of the strain  
 $d\varepsilon$  = infinitesimal increase of strain

$i$  = increment of summation for trapezoidal rule  
 $n$  = number of increments needed for accurate summation

## **4.2 Maximum Plastic Strain**

If the FAIL input parameter in \*MAT\_PIECEWISE\_LINEAR\_PLASTICITY is set to a positive number, the element will fail when the plastic strain reaches that number. Therefore, this parameter was adjusted for mesh 3 until the final SED matched the physical results, requiring an elemental failure strain of 1.03 to initiate fracture in the material.

## **4.3 Tied Nodes with Failure**

This approach required that each shell element be self-contained (i.e., the nodes defining the shell were not shared with any other shells). Then, all of the nodes occupying the same space were tied together and given a failure condition by \*CONSTRAINED\_TIED\_NODES\_FAILURE. The constitutive relationship in each shell was controlled by the same material cards as the maximum plastic strain procedure, except the failure strain was adjusted. To match the results of mesh 3 to the physical test results, an elemental failure strain of 1.21 was used to initiate fracture in the material.

## **4.4 Maximum Principal Strain**

This approach used the card \*MAT\_ADD\_EROSION to define failure. The constitutive relationship (Figure 6) in each shell was controlled by the same material cards as the maximum plastic strain procedure, except the failure strain was set to a large number,  $1 \times 10^{20}$ . Then the material ID used by the plasticity card was input into the erosion card, signifying that the \*MAT\_024 material would fail according to the provisions included in the erosion material cards. In this case, to match mesh 3 model results to physical test results, a maximum principal strain (MXEPS) of 1.00 was used to initiate fracture in the material.

#### 4.5 Maximum Shear Strain

Similar to the preceding section, this approach used \*MAT\_ADD\_EROSION and \*MAT\_024. Maximum shear strain was related to the maximum and minimum principle strain according to the relationships demonstrated in Mohr's circle. Knowing the principle strains,  $\varepsilon_1$  and  $\varepsilon_2$ , the shear strain,  $\gamma$ , is calculated as follows:

$$\gamma = \frac{\varepsilon_1 - \varepsilon_2}{2} \quad (4.2)$$

Where  $\gamma$  = Shear strain  
 $\varepsilon_1$  = Maximum principle strain  
 $\varepsilon_2$  = Minimum principle strain

The failure flag is activated when the shear strain equals or exceeds the user-specified maximum ( $\gamma \geq \gamma_{max}$ ). Maximum shear strain (EPSSH in \*MAT\_ADD\_EROSION) was adjusted until the mesh 3 results matched physical test results, requiring a maximum shear strain of 1.10 to initiate fracture in the material.

#### 4.6 Summary and Discussion

The value used for determining failure of an element or tied connection for each of the four described modeling techniques was determined by calibrating the central mesh (mesh 3) with physical tensile data. These limiting values are summarized in Table 2.

Table 2. Summary of Failure Parameters for Mesh 3

Failure Parameter Value for Mesh 3	
Maximum Plastic Strain	1.03
Tied Nodes with Failure	1.21
Maximum Principle Strain	1.00
Maximum Shear Strain	1.10

Internal energy, cross-sectional force, gauge-length deflection, and SED, as functions of the number of elements through the cross section, are plotted in Figures 12 through 15. Corresponding tabulated results are shown in Tables 3 through 6. The first three functions were included because the models were calibrated with SED. Therefore, pseudo-convergence studies were conducted on neutral variables, or variables that were indirectly affected for all four techniques. General FEM modeling requires a mesh sensitivity analysis to determine the coarsest allowable mesh while maintaining a converged solution. The premise of this research is based on the hypothesis that currently existing modeling techniques demonstrate significant mesh dependence, and this research would result in a technique that reduces that sensitivity. Therefore, once mesh dependence was demonstrated, the convergence study was ceased, making it a pseudo-convergence study, rather than a complete convergence study. In other words, a converged solution was not necessary to demonstrate mesh dependence.

Each of the four modeling techniques exhibited some level of mesh dependence, thus proving the hypothesis to be correct, and all but one appeared to converge or start to converge to a solution for the two finer meshes, indicating that the model is behaving as a typical FEM model is intended. In other words, as elements are added to the cross section, the model should tend towards the solution (or converge), as was the case in this study. In particular, the maximum plastic strain and maximum principle strain criteria provided nearly converged solutions of each metric for meshes 4 and 5. Also, the maximum shear strain began to converge but failed to reach the same level of convergence as the maximum plastic strain criterion. Tied nodes with failure, however, did not appear to converge for the given mesh densities.

The SED criterion was not a neutral variable. It was used to calibrate each model, and as such, it was expected to show similarities between the four techniques. In this case, the four techniques have very similar relationships between the SED at the point of fracture and the number

of elements through the cross section. However, the magnitudes were different at the extreme meshes. This parameter was calculated in LS-PrePost by first plotting the engineering stress against the engineering strain. The engineering stress was calculated by using a “secforc” ASCII file and dividing the resultant force by the cross-sectional area. The engineering strain was calculated by plotting the change in length in the x-direction and dividing that difference by the original gauge length. The two plots, as functions of time, were cross-plotted to get the classical stress-strain curve. Then, this curve was integrated to plot the SED as a function of strain. The SED at the point of fracture initiation correlated with the strain at the point of fracture initiation.

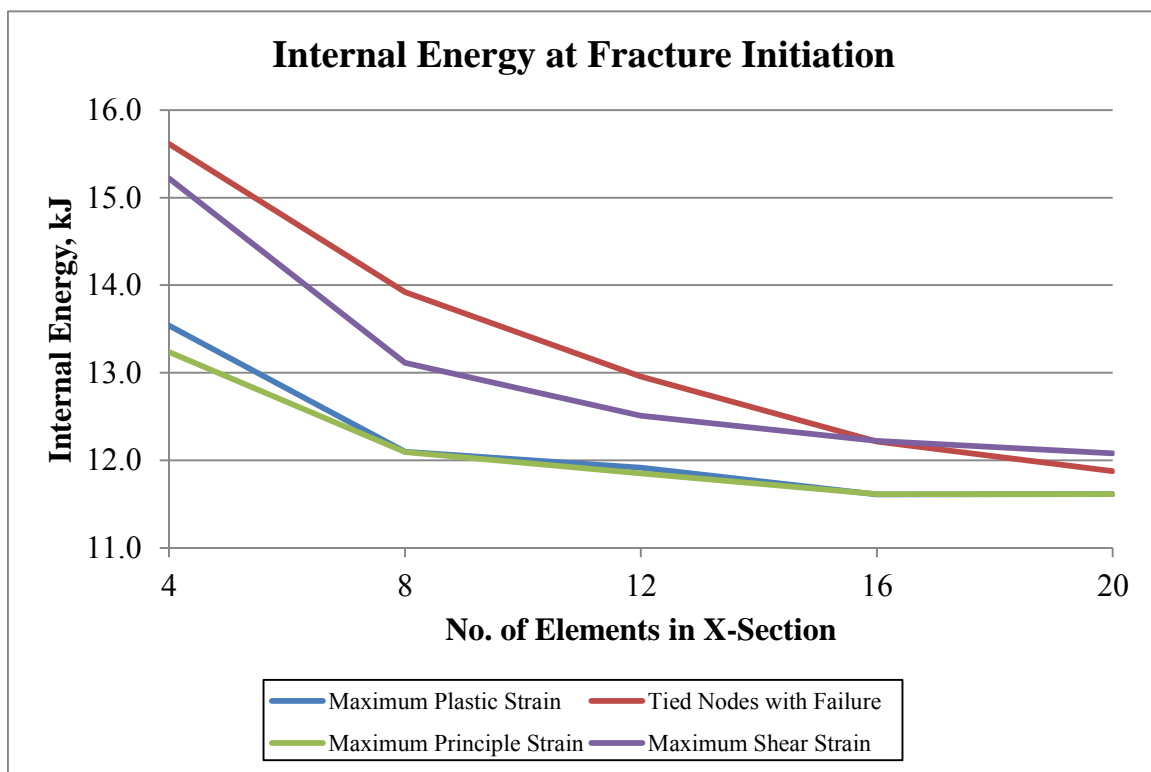


Figure 12. Internal Energy at the Point of Fracture Initiation

Table 3. Results of Convergence with Respect to Internal Energy

Internal Energy at Fracture Initiation (kJ)					
Mesh Description: Number of Elements in X-Section:	Mesh 1 4	Mesh 2 8	Mesh 3 12	Mesh 4 16	Mesh 5 20
Maximum Plastic Strain	13.539	12.098	11.915	11.612	11.614
Tied Nodes with Failure	15.614	13.923	12.959	12.215	11.877
Maximum Principle Strain	13.237	12.096	11.852	11.613	11.614
Maximum Shear Strain	15.220	13.115	12.511	12.223	12.080

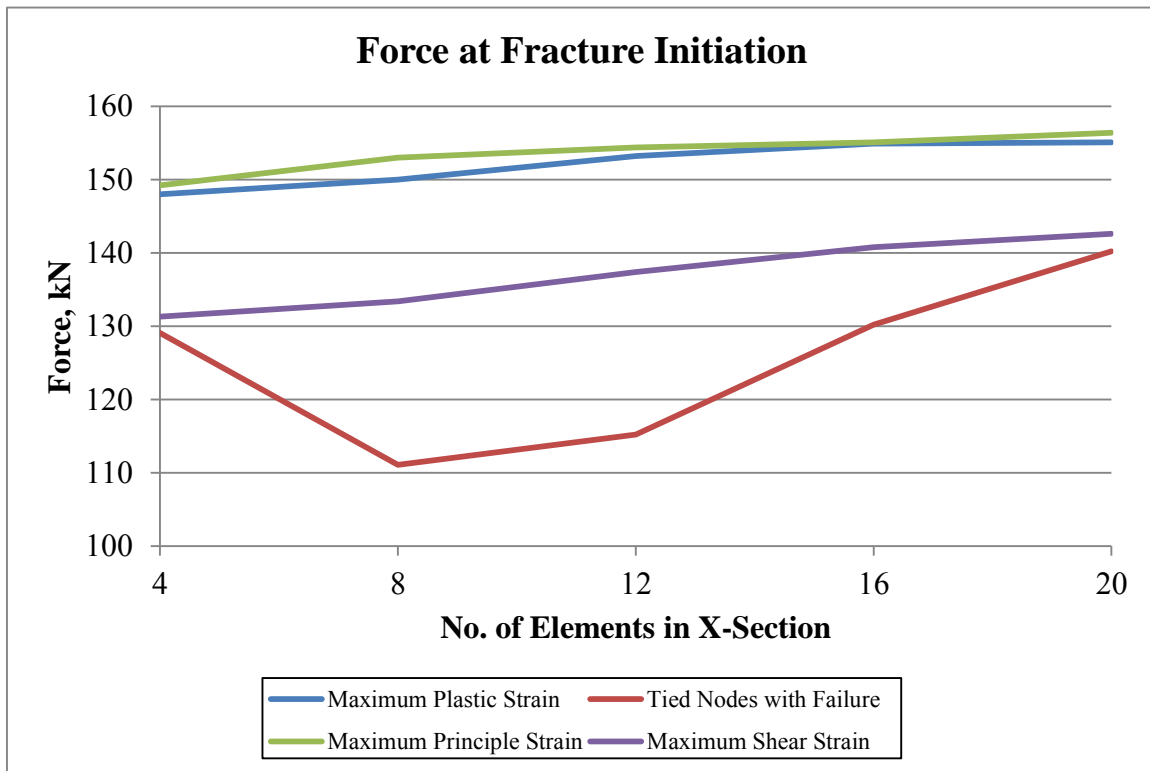


Figure 13. Cross-Sectional Force at the Point of Fracture Initiation

Table 4. Results of Convergence with Respect to Cross-Sectional Force

Force at Fracture Initiation (kN)					
Mesh Description: Number of Elements in X-Section:	Mesh 1 4	Mesh 2 8	Mesh 3 12	Mesh 4 16	Mesh 5 20
Maximum Plastic Strain	148.0	150.0	153.2	154.9	155.1
Tied Nodes with Failure	129.1	111.1	115.2	130.2	140.2
Maximum Principle Strain	149.2	153.0	154.4	155.1	156.4
Maximum Shear Strain	131.3	133.4	137.4	140.8	142.6

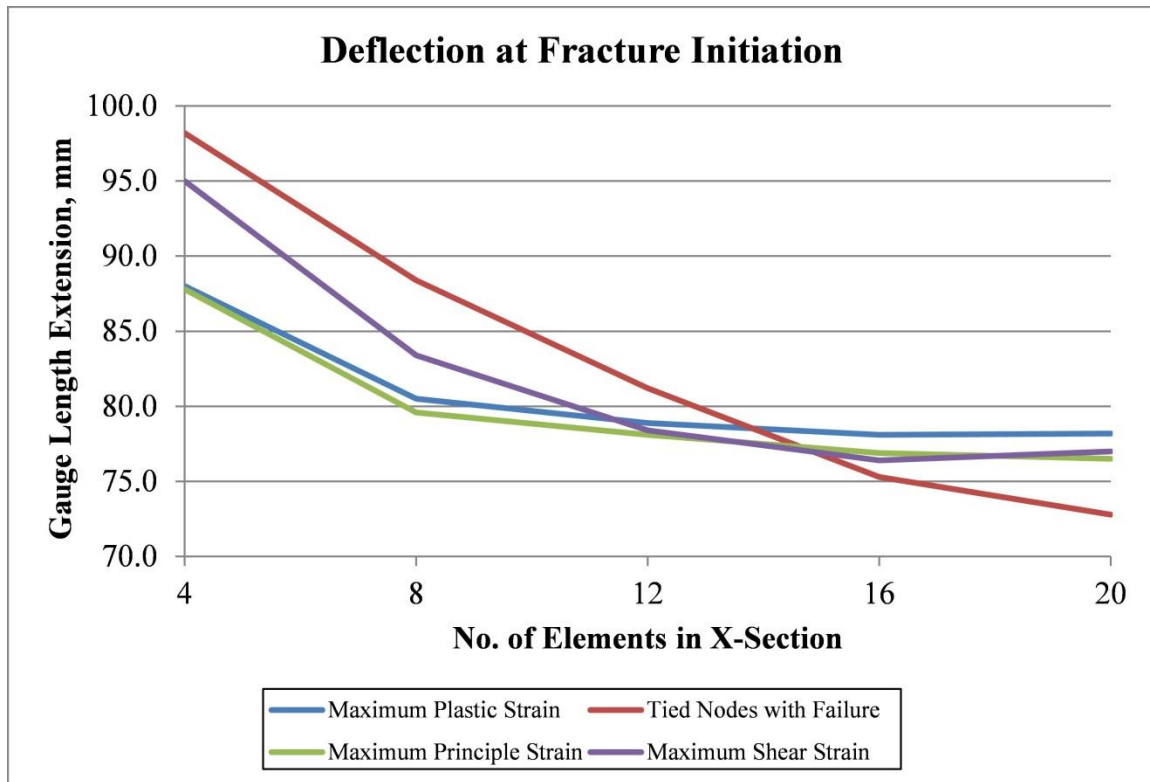


Figure 14. Gauge Length Deflection at the Point of Fracture Initiation



Table 5. Results of Convergence with Respect to Gauge Length Deflection

Deflection of Gage Length at Fracture Initiation (mm)					
Mesh Description: Number of Elements in X-Section:	Mesh 1 4	Mesh 2 8	Mesh 3 12	Mesh 4 16	Mesh 5 20
Maximum Plastic Strain	88.0	80.5	78.9	78.1	78.2
Tied Nodes with Failure	98.2	88.4	81.2	75.3	72.8
Maximum Principle Strain	87.8	79.6	78.1	76.9	76.5
Maximum Shear Strain	95.0	83.4	78.4	76.4	77.0

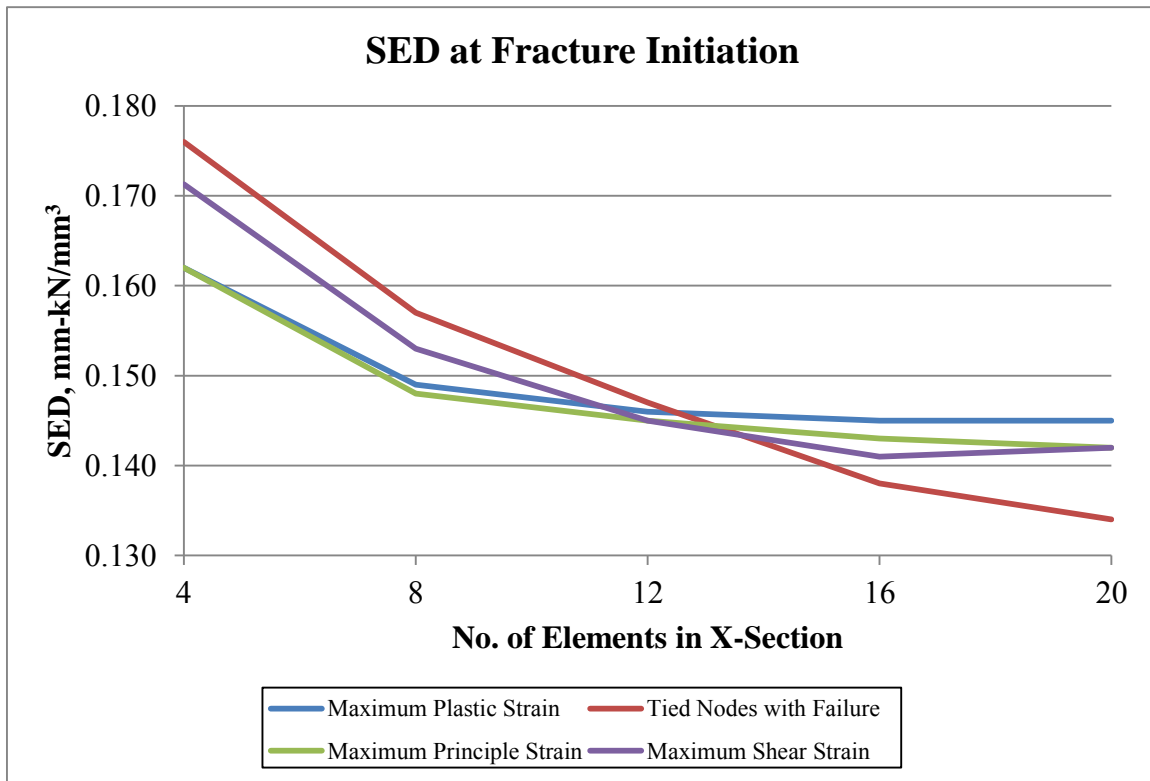


Figure 15. Strain Energy Density at the Point of Fracture Initiation

Table 6. Results of Convergence with Respect to Strain Energy Density

Strain Energy Density at Fracture Initiation (mm-kN/mm <sup>3</sup> )					
Mesh Description: Number of Elements in X-Section:	Mesh 1 4	Mesh 2 8	Mesh 3 12	Mesh 4 16	Mesh 5 20
Maximum Plastic Strain	0.162	0.149	0.146	0.145	0.145
Tied Nodes with Failure	0.176	0.157	0.147	0.138	0.134
Maximum Principle Strain	0.162	0.148	0.145	0.143	0.142
Maximum Shear Strain	0.1713	0.153	0.145	0.141	0.142

#### 4.7 Hourglass Energy

The shell elements were governed by a Belytschko-Tsay element formulation [66]. The formulation is computationally efficient but often suffers from the non-physical phenomenon known as hourglassing. To determine if more robust element formulations were required, or if hourglass controls needed to be added, the hourglass energy and internal energy of the coupon was plotted in Figure 16. From this plot, the hourglass energy was zero throughout the simulation, and a similar response was seen in all models. Therefore, the Belytschko-Tsay element formulation was considered adequate.

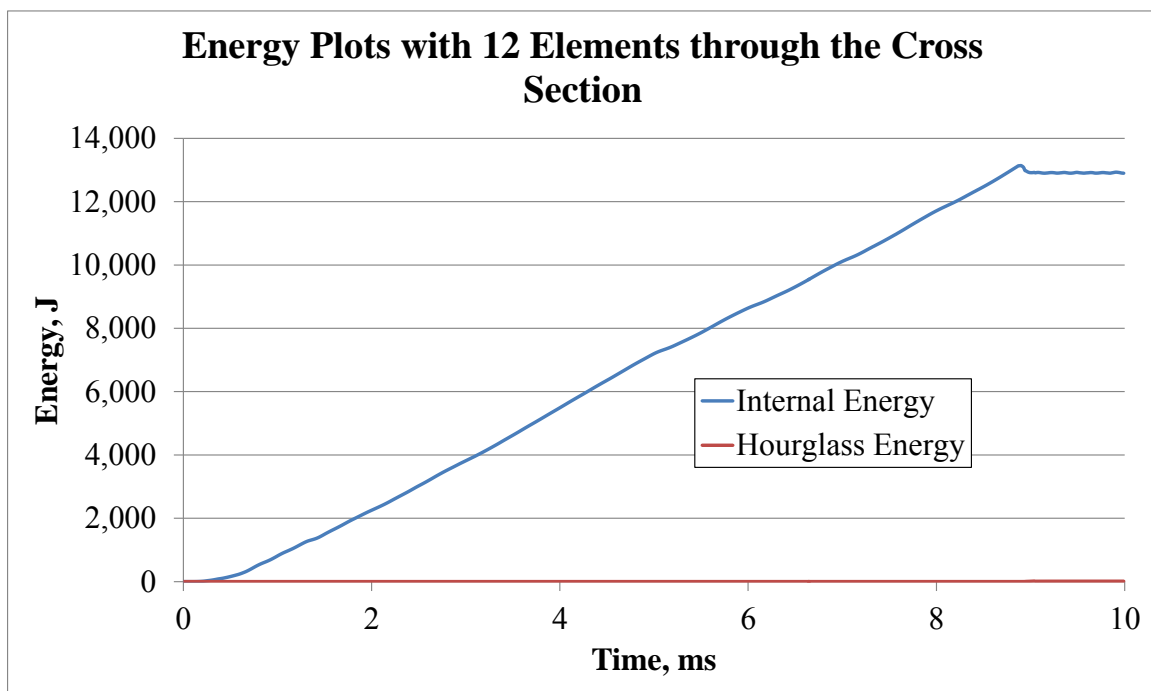


Figure 16. Hourglass and Internal Energy for Maximum Plastic Strain Model

## **5 DYNAMIC TENSILE TESTING SETUP**

### **5.1 Purpose**

Enlarged steel coupons were dynamically tested in tension to study the phenomena associated with this loading pattern. Specifically, strain-rate dependence and stress wave propagation were examined. The first phenomenon was investigated with physical testing to determine if it was applicable to the steel coupons for loading rates indicative of roadside safety engineering applications, specifically an impact event wherein a vehicle strikes a longitudinal barrier, such as a W-beam guardrail system. Then, testing was carried out to determine the accuracy of the SED failure criterion with respect to fracture initiation, as described in chapter 7. All dynamic tests were conducted at the Midwest Roadside Safety Facility (MwRSF) Proving Grounds in Lincoln, Nebraska. The testing facility is located at the Lincoln Air Park on the northwest side of the Lincoln Municipal Airport and is approximately 5 miles (8.0 km) northwest of the University of Nebraska-Lincoln.

### **5.2 Scope**

Dynamic tensile testing on wire rope has been done by MwRSF in the past and provided the framework for the current research [69]. A total of 11 bogie tests were conducted on enlarged steel coupons mounted to a rigid frame and concrete bogie block. The steel coupons were composed of ASTM A572 Grade 50, ASTM A1011-12B Grade 50, or AASHTO M180 steel, and the mill certificates of conformity are given in Appendix B. Testing was limited to uniaxial tension, producing primarily Mode I loading. Coupons were cut either parallel (longitudinal) or perpendicular (transverse) to the roll direction. Stress concentrations were added to four coupon tests. Finally, testing was conducted at temperatures well above the ductile-to-brittle transition temperature.

### 5.3 Summary of Steel Coupons and Component Tests

In all, 11 enlarged steel coupons were planned for the dynamic testing program and subjected to uniaxial tension. A stress concentration was included in four of those coupons. Three materials were employed: A572 Gr. 50, A1011-12B Gr. 50, and AASHTO M180. Coupon thickness was either  $\frac{5}{16}$  in. (7.9 mm), 10 gauge (3.42 mm), or 12 gauge (2.67 mm). The width of the critical section was either  $1\frac{5}{8}$  or  $2\frac{1}{4}$  in. (41.3 or 57.2 mm). Target bogie velocities ranged from 5 to 25 mph (8.0 to 40.2 km/h). Finally, the orientation of the grain in the steel resulting from the rolling process was either parallel or perpendicular to the direction of the coupon. A summary of all 11 steel coupons and test conditions is shown in Table 7.

Table 7. Summary of Dynamic Bogie Testing Matrix for Enlarged Steel Coupons

Test Name	Material	Stress Concentration	Thickness, in. [mm]	Width, in. [mm]	Target Bogie Velocity, mph [km/h]	Grain Orientation
DFS-L1	A572 Gr. 50	Circle	5/16 [7.9]	$1\frac{5}{8}$ [41.3]	15 to 20 [24.1 to 32.1]	Longitudinal
DFS-L2	A572 Gr. 50	Circle	5/16 [7.9]	$1\frac{5}{8}$ [41.3]	15 to 20 [24.1 to 32.1]	Longitudinal
DFS-L3	A572 Gr. 50	None	5/16 [7.9]	$1\frac{5}{8}$ [41.3]	5 to 10 [8.0 to 16.1]	Longitudinal
DFS-L3-2	A572 Gr. 50	None	5/16 [7.9]	$1\frac{5}{8}$ [41.3]	20 to 25 [32.2 to 40.2]	Longitudinal
DFS-L4	AASHTO M180	None	12 ga. [2.66]	$2\frac{1}{4}$ [57.2]	15 to 20 [24.1 to 32.1]	NA
DFS-L5	A1011-12B Gr. 50	None	10 ga. [3.42]	$1\frac{5}{8}$ [41.3]	15 to 20 [24.1 to 32.1]	NA
DFS-L6	AASHTO M180	Circle	12 ga. [2.66]	$2\frac{1}{4}$ [57.2]	15 to 20 [24.1 to 32.1]	NA
DFS-L7	A1011-12B Gr. 50	Circle	10 ga. [3.42]	$1\frac{5}{8}$ [41.3]	15 to 20 [24.1 to 32.1]	NA
DFS-T1	A572 Gr. 50	None	5/16 [7.9]	$1\frac{5}{8}$ [41.3]	20 to 25 [32.2 to 40.2]	Transverse
DFS-T2	A572 Gr. 50	None	5/16 [7.9]	$1\frac{5}{8}$ [41.3]	20 to 25 [32.2 to 40.2]	Transverse
DFS-T3	A572 Gr. 50	None	5/16 [7.9]	$1\frac{5}{8}$ [41.3]	20 to 25 [32.2 to 40.2]	Transverse

### 5.4 Evolution of Testing Phase

Initially, six coupons of A572 Gr 50 steel were created for testing, with three cut parallel to the grain of the steel and three cut perpendicular to the grain of the steel. Testing was to begin with low-speed tensile loads (targeting 5 to 10 mph or 8.0 to 16.0 km/h). The first test (test no. DFS-L3) was conducted on a longitudinal sample (cut parallel to the grain), and the actual speed

of the bogie at the time of release from the towing vehicle was 12.2 mph (19.6 km/h). Since no plastic deformation was observed in the sample, a second test (test no. DFS-L3-2) using this coupon was set up for a higher speed, targeting 20 to 25 mph (32.2 to 40.2 km/h). For both tests, the 4-cable towing assembly was laid out in one curve, with the amplitude of the curve perpendicular to the direction of travel of the bogie. For the high-speed test, the steel coupon ruptured before the cables even lifted off the ground or became completely straight with respect to the direction of the bogie. This result indicated an enormous amount of energy in the cable: enough, in fact, to cause significant damage to the components of the test configuration. This damage included complete rupture of a high-strength,  $\frac{3}{4}$ -in. (19-mm) diameter cable tether, which was intended to prevent the separated end of the coupon from being dragged down the runway.

Owing to this extreme energy, the cables were repositioned for subsequent tests by looping the cables parallel to the bogie direction. With this configuration, the side-to-side motion of the cable was mitigated, and the energy in the cable was primarily applied parallel to the bogie direction, which would then reduce damage in the system that was previously caused by side-to-side cable whip. This reduced damage would allow for faster turn-around time from test to test and a more consistent uniaxial tensile load on the steel coupon.

Initially, the cable was attached to two tubes positioned on rollers, supported by the web of a steel H-barrier [70]. These tubes were only  $\frac{1}{8}$ -in. (3.2-mm) thick, and the sudden application of energy from the cable caused significant deformation around the bolt holes and throughout the length of the tube. The H-barrier itself was knocked off its support and out of alignment. To mitigate this, the tube thicknesses were increased to  $\frac{3}{8}$  in. (9.5 mm) and welded together. Then, the combined assembly was mounted to a second bogie vehicle. This additional weight and stiffened system damped out vibrations from the cable loading to the point where multiple tests

could be conducted in a single day with very little down time required for repairs. An overall view of the final version of the dynamic test configuration is shown in Figure 17.



Figure 17. Overall View of Final Version of the Dynamic Tensile Test Configuration

### **5.5 Equipment and Instrumentation**

The equipment and instrumentation that was used to collect and record data during the dynamic component tests included a bogie, a test jig, accelerometers, load cells, high-speed and standard-speed digital video, and still cameras.

### 5.5.1 Bogies

Two rigid-frame bogies were used to apply the tensile load. A four-cable tether was used to connect the two bogies. The larger bogie, weighing 4,952 lbs. (2,251 kg), was guided by keeping one side's wheels in the valley of a guardrail, as shown in Figure 18. The smaller bogie, weighing 2,108 lbs (956 kg), was attached at one end to the four-cable tether, and at the other end to the steel coupon.



Figure 18. Rigid-Frame Bogie on Guidance Track

The four-cable assembly was originally attached to the larger bogie by a ribbed bracket and shackle assembly, where the 1-in. (25-mm) diameter pin was loaded in double shear. However, this bracket was significantly damaged in the first test using the two-bogie system (second test overall), and was replaced by three nylon tethers, each with a 17,000-lb (75.6-kN) capacity. The four-cable assembly was attached to the nylon tethers with a clevis and is shown attached to the bogie in Figure 18.



The coupon was attached to two steel tubes, each measuring 13 ft - 1¼ in. (4.0 m) in length. The dimensions of the cross sections were 3½ in. x 3½ in. x ⅜ in. (89 mm x 89 mm x 9.5 mm). They were welded together in five locations, approximately spaced evenly throughout the length of the tubes. The combined assembly was mounted to the bogie with steel brackets, which were welded to the tubes. These brackets were placed on top of a stack of steel plates and welded in place. The stack of steel plates was then bolted to the frame of the bogie vehicle. An overall view of this mounting assembly is shown in Figure 19.

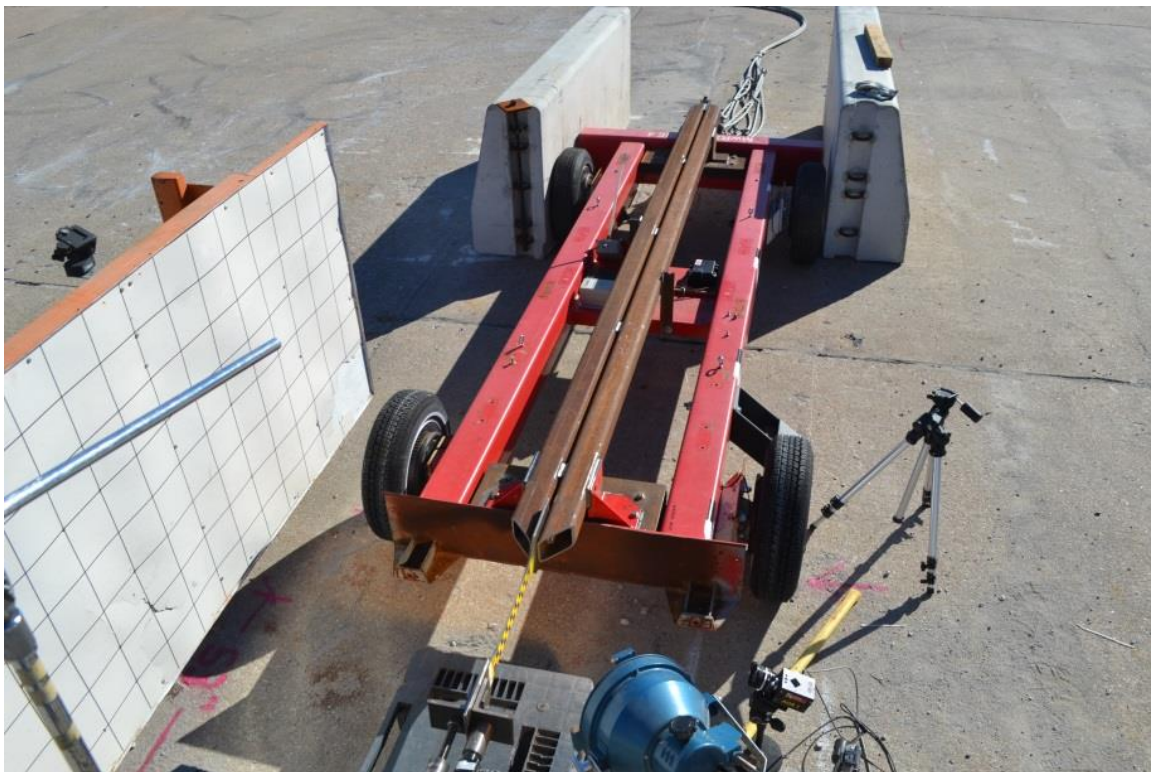


Figure 19. Two-Tube Steel Coupon Mounting Assembly

### 5.5.2 Load Cells

The load frame assembly was mounted such that the attachment brackets were free to rotate about a horizontal axis, allowing for horizontal views of the enlarged steel coupons for high-speed cameras. Drawings of the load frame assembly are provided in Appendix A. A photo of the



assembly is provided in Figure 20. Four concrete-filled steel tubes with cross-sectional dimensions of 4 in. x 4 in. x  $\frac{1}{4}$  in. (102 mm x 102 mm x 6 mm) and a length of 16 in. (406 mm) were mounted to the concrete bogie block located at MwRSF's test facility. Holes were drilled through each tube and 1-in. (25-mm) diameter threaded rods were placed through those holes prior to filling the tubes with concrete. The back tubes (closest to the bogie block) included a 2½-in. (64-mm) hole in the sides of the tubes. A load cell assembly was inserted into these two holes such that the assembly could rotate in one direction (about the horizontal axis). The front tubes were added to stiffen the assembly.



Figure 20. Load Cell and Mounting Assembly

## 5.6 Accelerometers

An accelerometer system was mounted on the small bogie vehicle near its center of gravity to measure the acceleration in the longitudinal, lateral, and vertical directions. Only the

longitudinal acceleration was processed, however, due to the response of the cable tether and other nonlinear contributions; the force estimates from the accelerometers were unreliable as they applied to the steel coupon. Load transducers applied to the anchored end of the coupon were far more reliable.

The first accelerometer system was a two-arm piezoresistive accelerometer system manufactured by Endevco of San Juan Capistrano, California. Three accelerometers were used to measure each of the longitudinal, lateral, and vertical accelerations independently at a sample rate of 10,000 Hz. The accelerometers were configured and controlled using a system developed and manufactured by Diversified Technical Systems, Inc. (DTS) of Seal Beach, California. More specifically, data was collected using a DTS Sensor Input Module (SIM), Model TDAS3-SIM-16M. The SIM was configured with 16 MB SRAM and 8 sensor input channels with 250 kB SRAM/channel. The SIM was mounted on a TDAS3-R4 module rack. The module rack was configured with isolated power/event/communications, 10BaseT Ethernet and RS232 communication, and an internal backup battery. Both the SIM and module rack were crashworthy. The “DTS TDAS Control” computer software program and a customized Microsoft Excel worksheet were used to analyze and plot the accelerometer data.

The third system, Model EDR-3, was a triaxial piezoresistive accelerometer system manufactured by Instrumental Sensor Technology, Inc. (IST) of Okemos, Michigan. The EDR-3 was configured with 256 kB of RAM, a range of  $\pm 200$  g's, a sample rate of 3,200 Hz, and a 1,120 Hz low-pass filter. The “DynaMax 1 (DM-1)” computer software program and a customized Microsoft Excel worksheet were used to analyze and plot the accelerometer data.

### **5.6.1 Digital Photography**

Two AOS VITcam high-speed digital video cameras, one JVC digital video camera, and two GOPRO cameras were used to document each test. The AOS high-speed cameras had a frame

rate of 4,000 frames per second. All but one of the cameras was placed laterally from the coupon, with a view perpendicular to the bogie's direction of travel. A GOPRO camera was placed downstream of the coupon in an orientation that captured the overall view of the test, including the coupon, H-barrier (if applicable), cables, and bogies. A Nikon D50 digital still camera was also used to document pre- and post-test conditions for all tests.

### 5.6.2 Gauge Length Grid

On each coupon, a uniform grid was painted for reference in post-test high-speed video analysis. The grid was created by printing a vinyl decal with a square pattern. The length of each side of the squares was equated to half the width of the critical section of the coupon, or  $13/16$  in. (20.6 mm). The decal was transferred to the coupon and centered longitudinally. Next, in anticipation of large strains, plastic yellow spray paint was applied to the coupon in three layers. Once the third layer dried sufficiently, the vinyl decals were removed, leaving a checkered grid pattern. Each printed vinyl decal included extraneous squares on both sides of the gauge length. In these squares, a black "X" was drawn with a permanent marker. The unmarked squares represented the gauge length and measured  $9\frac{3}{4}$  in (248 mm). This gauge length was used for all 11 coupons. An example of this grid is shown in Figure 21.

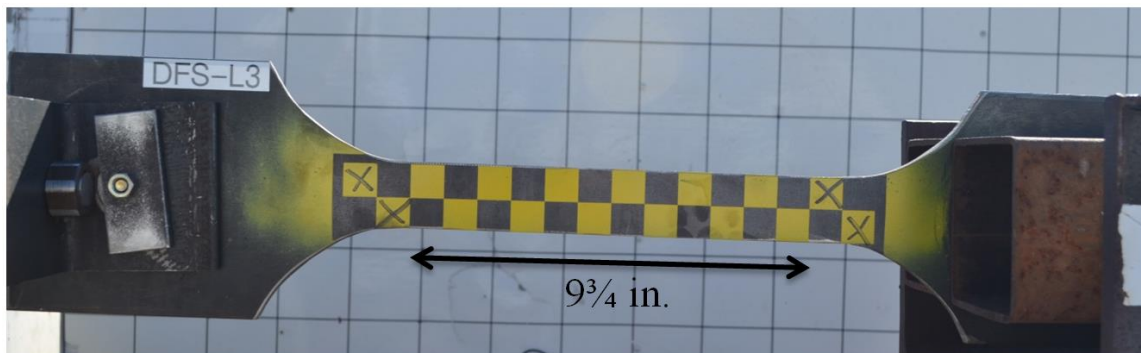


Figure 21. Gauge Length Grid Data Processing

## 5.7 Coupon Descriptions

Each coupon shared the same profile footprint. They were enlarged relative to the standard size used in quasi-static tensile tests for two reasons. First, the load was applied by towing a bogie and recorded by load transducers. Low-speed tests would have been nearly impossible to repeat consistently, and the margin of error in the load cells may have been influential. To avoid both pitfalls, a large sample, as shown in Figure 5, was used for each coupon. However, the material itself, as well as thickness and grain orientation, were different in some tests. Finally, the target bogie velocity was subject to change according to the expected strength of the coupon.

### 5.7.1 Test Nos. DFS-L1 and DFS-L2

Each of these tests utilized A572 Gr. 50 steel, whose mill certificate of conformity is given in Appendix B. The thickness of each coupon was  $\frac{5}{16}$  in. (7.9 mm). Finally, these coupons were modified by drilling a  $\frac{1}{2}$ -in. (12.7-mm) diameter hole in the center of the coupon, creating a stress concentration. The target bogie velocity for these tests was 15 to 20 mph (24.1 to 32.1 km/h). The coupon was cut parallel to the roll direction, such that the grain orientation was longitudinal. A stress concentration was added to both coupons by drilling a  $\frac{1}{2}$ -in. (12.7-mm) hole in the center. Pre-test photos of each coupon are shown in Figures 22 and 23.



Figure 22. Test No. DFS-L1, Pre-Test



Figure 23. Test No. DFS-L2, Pre-Test

### 5.7.2 Test No. DFS-L3

This coupon utilized A572 Gr. 50 steel, whose mill certificate of conformity is given in Appendix B. The thickness of this coupon was  $\frac{5}{16}$  in. (7.9 mm). This coupon did not contain a stress concentration, but it had a target velocity of 5 to 10 mph (8.0 to 16.1 km/h). The coupon was cut parallel to the roll direction, such that the grain orientation was longitudinal. A pre-test photo of this coupon is shown in Figure 24.



Figure 24. Test No. DFS-L3, Pre-Test

### 5.7.3 Test No. DFS-L3-2

Test no. DFS-L3-2 was run with the same coupon from test no. DFS-L3 using a target velocity of 20 to 25 mph (32.2 to 40.2 km/h). The bogie speed from the previous test did not produce a large enough load to induce plasticity in the coupon. The coupon was cut parallel to the



roll direction, such that the grain orientation was longitudinal. A pre-test photo of this coupon is shown in Figure 25.



Figure 25. Test No. DFS-L3-2, Pre-Test

#### 5.7.4 Test No. DFS-L4

This test utilized AASHTO M180 steel, whose mill certificate of conformity is given in Appendix B. The thickness of the coupon was 12 gauge (2.67 mm). The target bogie velocity for this test was 15 to 20 mph (24.1 to 32.1 km/h). The through-thickness was cut differently for this test and measured 2¼ in. (57.2 mm). A pre-test photo of this coupon is shown in Figure 26.



Figure 26. Test No. DFS-L4, Pre-Test

#### 5.7.5 Test No. DFS-L5

This test utilized A1011-12B Gr. 50 steel, whose mill certificate of conformity is given in Appendix B. The thickness of this coupon was 10 gauge (3.42 mm). The target bogie velocity for

this test was 15 to 20 mph (24.1 to 32.1 km/h). A pre-test photo of this coupon is shown in Figure 27.



Figure 27. Test No. DFS-L5, Pre-Test

#### 5.7.6 Test Nos. DFS-L6 and DFS-L7

Test nos. DFS-L6 and DFS-L7 were repeated from test nos. DFS-L4 and DFS-L5, respectively, with one additional caveat. A stress concentration was added by drilling a ½-in. (12.7-mm) hole in the center of the coupons. The target bogie velocity for these tests was 15 to 20 mph (24.1 to 32.1 km/h). Cross-sectional widths were 2¼ and 1⅝ in. (57.2 and 41.3 mm) for test nos. DFS-L6 and DFS-L7, respectively. Pre-test photos for these coupons are shown in Figures 28 and 29.



Figure 28. Test No. DFS-L6, Pre-Test



Figure 29. Test No. DFS-L7, Pre-Test

#### 5.7.7 Test Nos. DFS-T1, DFS-T2, and DFS-T3

Each of these tests utilized A572 Gr. 50 steel, whose mill certificate of conformity is given in Appendix B. The thickness of each coupon was  $\frac{5}{16}$  in. (7.9 mm). The target bogie velocity for these tests was 20 to 25 mph (32.2 to 40.2 km/h). The coupon was cut perpendicular to the roll direction, such that the grain orientation was transverse. Pre-test photos of these coupons are shown in Figures 30 through 32.



Figure 30. Test No. DFS-T1, Pre-Test





Figure 31. Test No. DFS-T2, Pre-Test



Figure 32. Test No. DFS-T3, Pre-Test

## **6 TENSILE TEST RESULTS**

### **6.1 Quasi-Static Material Testing**

#### **6.1.1 A572 Gr. 50 Steel**

Tensile force-deflection data was obtained from component test results on roadside breakaway sign supports in the mid-1990s [58], and the corresponding stress-strain curves were likewise collected from literature [59]. In the samples documented from these sources, the yield stress of the steel was 67 ksi (462 MPa). However, according to the mill certificate of conformity, presented in Appendix B, the yield stress of the steel used in this project was 63.7 ksi (439 MPa). Therefore, the stress-strain curve found in previous testing was scaled down to match the material used in this report. Scaling was accomplished by multiplying the stress at each point by the ratio of the yield stress from the mill certificate to the yield stress reported in literature. The resulting stress-strain curve is shown in Figure 33, where failure occurred at a strain of 0.237. The area under this curve, or the strain energy density, was 21.0 in.-kip/in.<sup>3</sup> (144.7 mm-N/mm<sup>3</sup>).

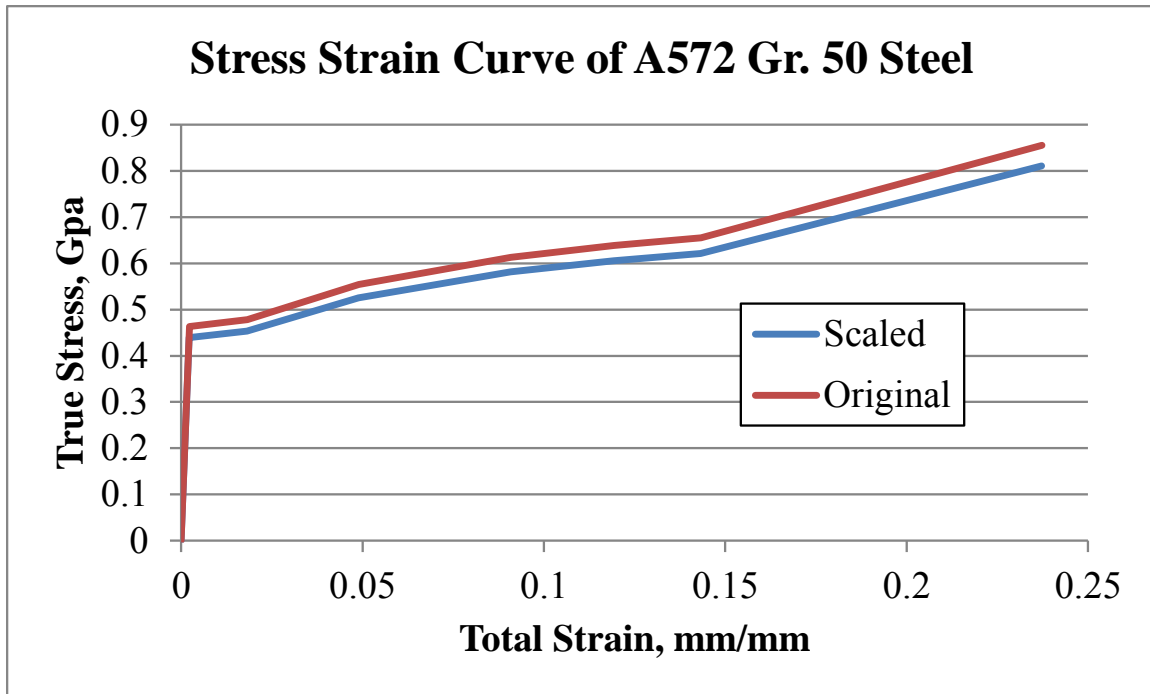


Figure 33. Scaled Stress-Strain Curve of A572 Gr. 50 Steel [59] to Match 0.439 GPa

### 6.1.2 AASHTO M180 Steel

Standard W-beam guardrail conforms to AASHTO M180 steel, whose strength characterization is abundantly documented in literature. Most recently, a research effort was undertaken at the Midwest Roadside Safety Facility to investigate the variational strength of this material, and a baseline material model was recommended for use in the LS-DYNA material model, \*MAT\_PIECEWISE\_LINEAR\_PLASTICITY [60]. The stress-strain curve adopted in the current project is shown in Figure 34 where failure occurred at a strain of 0.203. The area under this curve, or the strain energy density, was 15.8 in.-kip/in.<sup>3</sup> (108.7 mm-N/mm<sup>3</sup>).

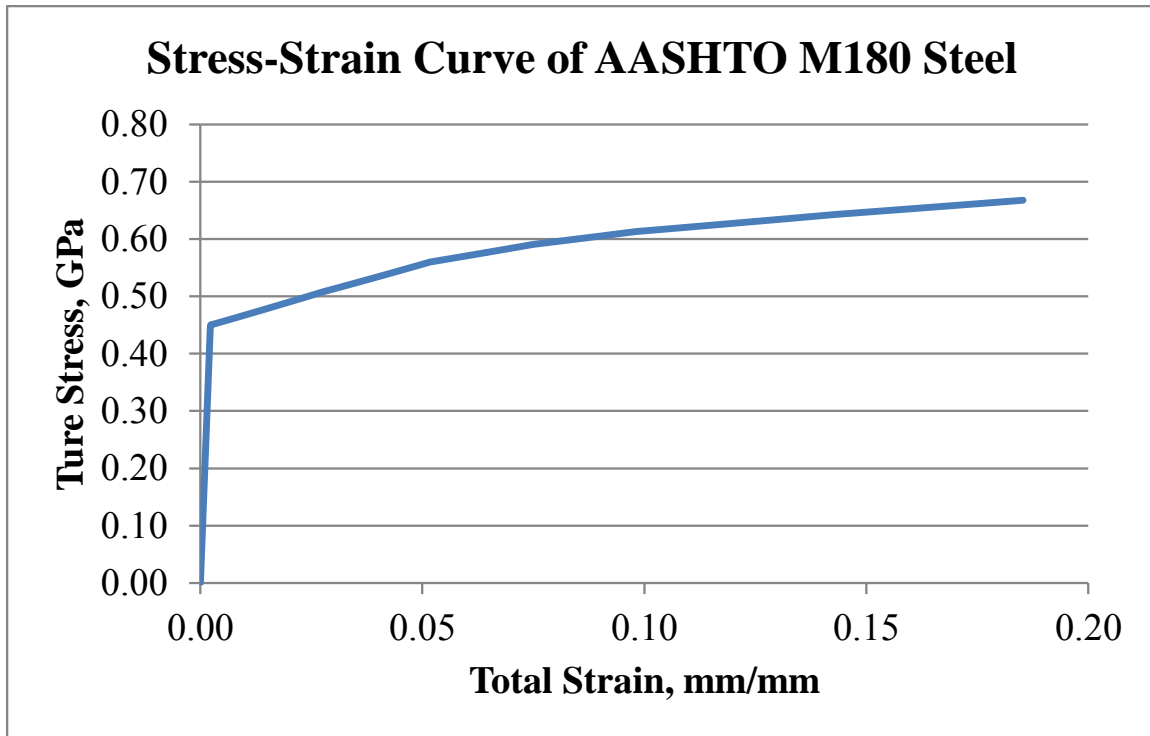


Figure 34. Stress-Strain Curve of AASHTO M180 Steel [60]

### 6.1.3 A1011-12B Gr. 50 Steel

Quasi-static data was not available for this material. As such, the yield stress reported in the mill certificate of conformity was used to scale the stress-strain data used for AASHTO M180 steel. Scaling was accomplished by multiplying the stress at each point by the ratio of the yield stress from the mill certificate to the yield stress reported in literature. The scaled stress-strain curve used in LS-DYNA is shown in Figure 35. The area under this curve, or the strain energy density, was 18.5 in.-kip/in.<sup>3</sup> (127.8 mm-N/mm<sup>3</sup>).

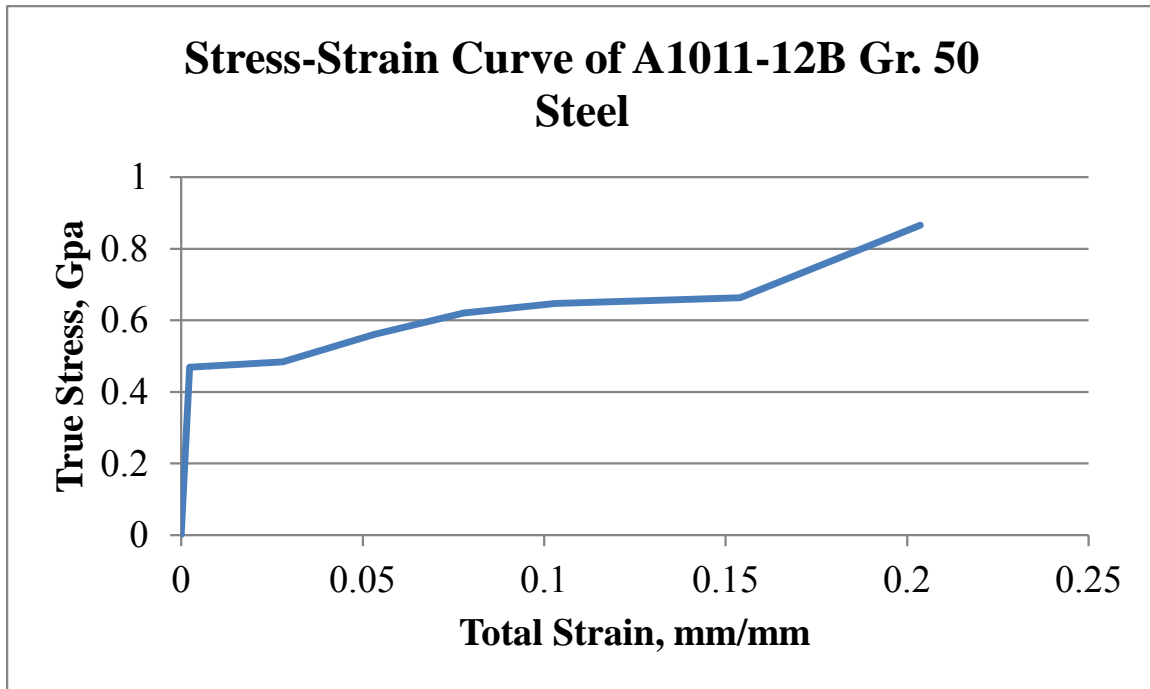


Figure 35. Stress-Strain Curve of A1011-12B Gr. 50 Steel

#### 6.1.4 LS-DYNA Description of Materials

The quasi-static stress-strain curves for the preceding materials were used to develop the constitutive relationship in LS-DYNA via the material input card `*MAT_PIECEWISE_LINEAR_PLASTICITY`. This card uses an 8-point stress-strain curve to control the behavior of the material. Strains are input according to the effective plastic strain, i.e., the elastic strain in the material is removed. The corresponding stress to the effective plastic strain is also programmed. This stress can represent engineering or true stress-strain curves. However, the eighth point in the curve is typically adjusted by trial-and-error until the simulated stress-strain response matches physical data, and, in this case, engineering stress-strain results from test no. DFS-L3-2 were used to calibrate the material model. The points used for each material are summarized in Table 8.

Table 8. Summary of LS-DYNA Material Input

Data Input	A572 Gr. 50		AASHTO M180		A1011-12B Gr. 50	
	EPS (mm/mm)	ES (GPa)	EPS (mm/mm)	ES (GPa)	EPS (mm/mm)	ES (GPa)
Point 1	0.000	0.439	0.000	0.449	0.000	0.469
Point 2	0.016	0.473	0.026	0.494	0.033	0.472
Point 3	0.047	0.520	0.051	0.532	0.050	0.509
Point 4	0.089	0.561	0.076	0.548	0.076	0.546
Point 5	0.117	0.586	0.101	0.556	0.101	0.572
Point 6	0.141	0.601	0.152	0.557	0.126	0.591
Point 7	0.185	0.621	0.201	0.558	0.153	0.609
Point 8	2.000	1.800	2.000	1.800	0.999	1.021

## 6.2 Dynamic Coupon Tests

### 6.2.1 Test No. DFS-L1

During test no. DFS-L1, the bogie reached a speed of 18.1 mph (29.1 km/h), causing nearly uniaxial tension in the coupon. The coupon was loaded past its elastic limit around the hole and experienced very little necking and even less deformation away from the hole. Highly localized ductile failure was observed around the hole, and additional evidence of plasticity was discovered in the observation that the plastic spray paint melted off of the coupon near the location of the fracture; heat generation can be significant in plastic deformation.

Force-deflection and energy-deflection curves were created from the load cell data and high-speed video analysis and are shown in Figure 36. Yield occurred at 24.7 kips (109.9 kN) and increased until an ultimate force of 33.1 kips (147.2 kN) was observed at a displacement of 0.21 in. (0.5 cm) over the gauge length, resulting in a dynamic strain of 0.022 in./in. (mm/mm). At this displacement, the coupon absorbed 5.31 k-in. (0.6 kJ) of energy. The strain energy density at fracture was 1.6 in.-kip/in.<sup>3</sup> (11.0 mm-N/mm<sup>3</sup>). The stress-strain curve used in determining the SED is shown in Figure 37. Photographs of coupon damage are shown in Figure 38.

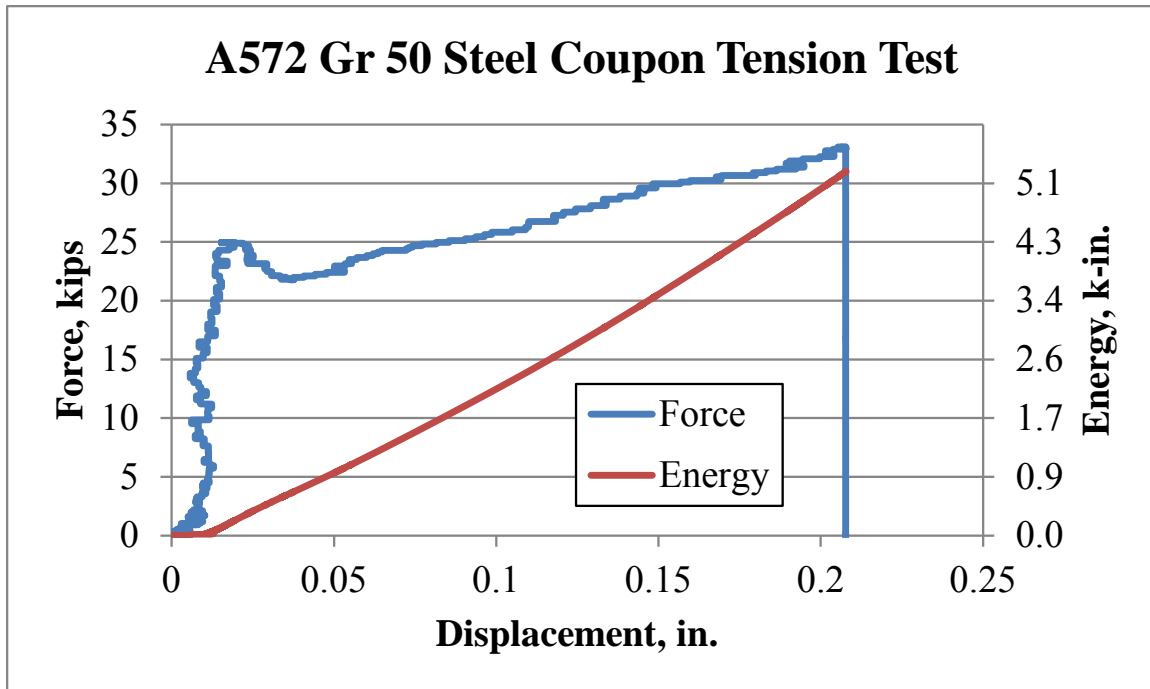


Figure 36. Force vs. Deflection and Energy vs. Deflection, Test No. DFS-L1

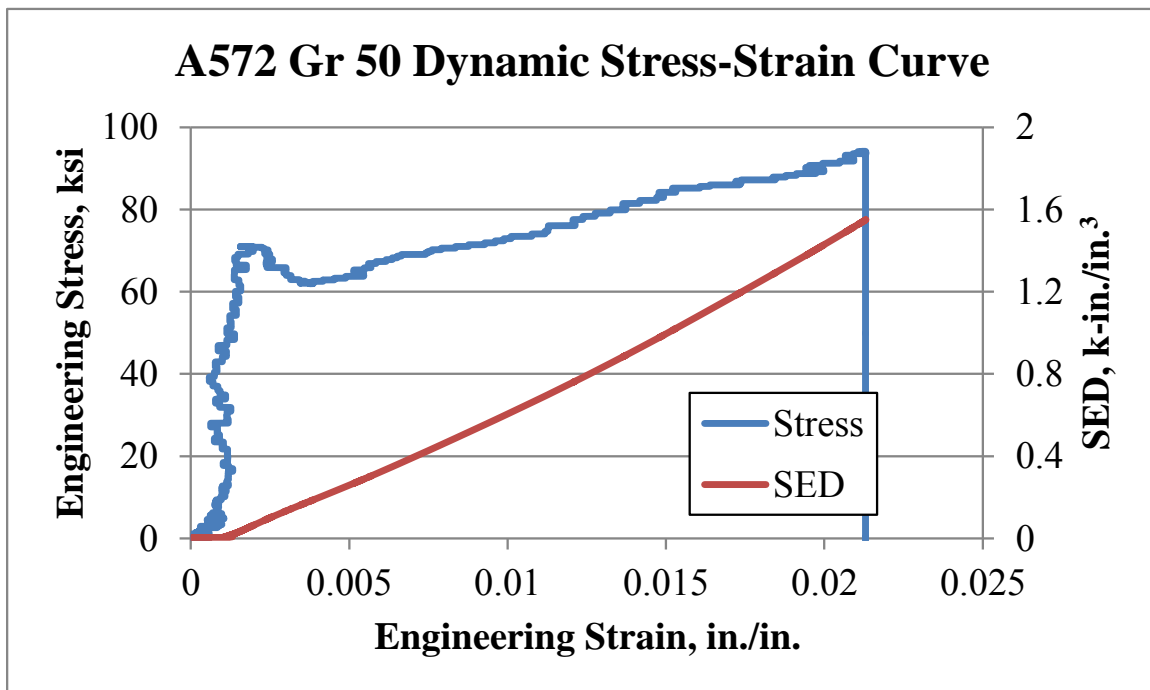


Figure 37. Stress vs. Strain, Test No. DFS-L1



Figure 38. Post-Impact Photographs, Test No. DFS-L1

### 6.2.2 Test No. DFS-L2

During test no. DFS-L2, the bogie reached a speed of 16.6 mph (26.7 km/h), causing nearly uniaxial tension in the coupon. The coupon was loaded past its elastic limit around the hole and experienced very little necking and even less deformation away from the hole. Highly-localized ductile failure was observed around the hole, and additional evidence of plasticity was observed when the plastic spray paint melted off of the coupon near the location of the fracture; heat generation can be significant in plastic deformation.

Force-deflection and energy-deflection curves were created from the load cell data and high-speed video analysis and are shown in Figure 39. Yield occurred at approximately 20 kips (89.0 kN) and increased until an ultimate force of 31.2 kips (138.8 kN) was observed at a displacement of 0.39 in. (1.0 cm), resulting in an ultimate strain of 0.040 in./in. (mm/mm). At this displacement, the coupon absorbed 8.4 k-in. (1.0 kJ) of energy. The strain energy density at



fracture was 2.4 in.-kip/in.<sup>3</sup> (16.6 mm-N/mm<sup>3</sup>). The stress-strain curve used in determining the SED is shown in Figure 40. Photographs of coupon damage are shown in Figure 41.

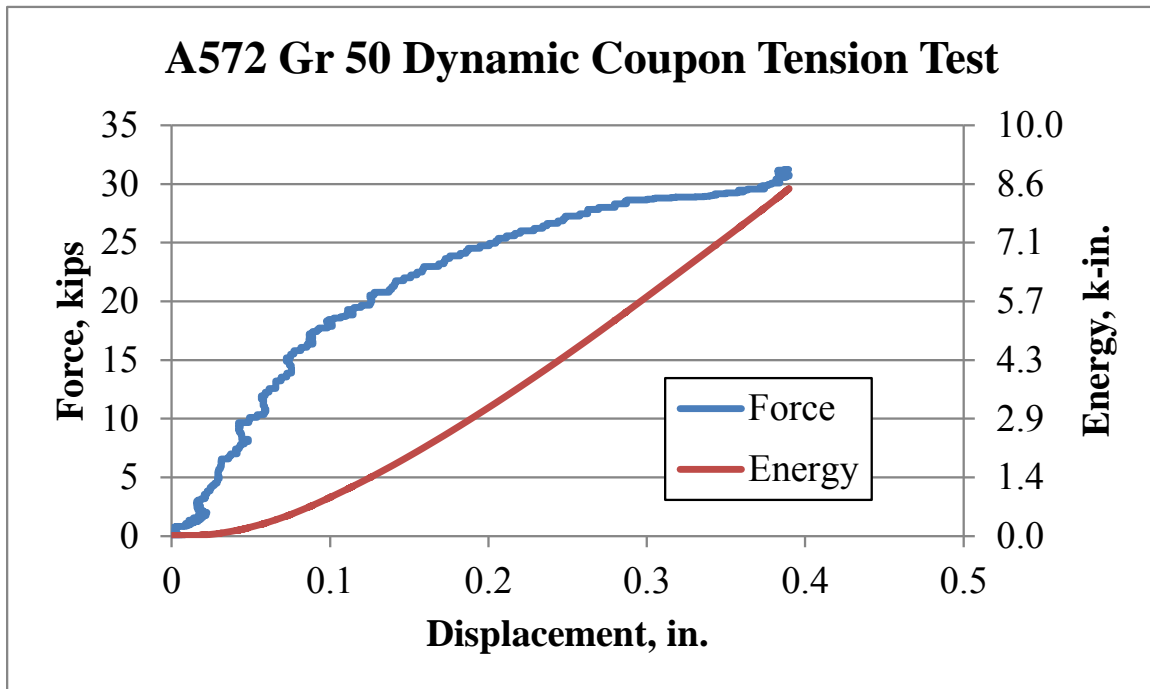


Figure 39. Force vs. Deflection and Energy vs. Deflection, Test No. DFS-L2

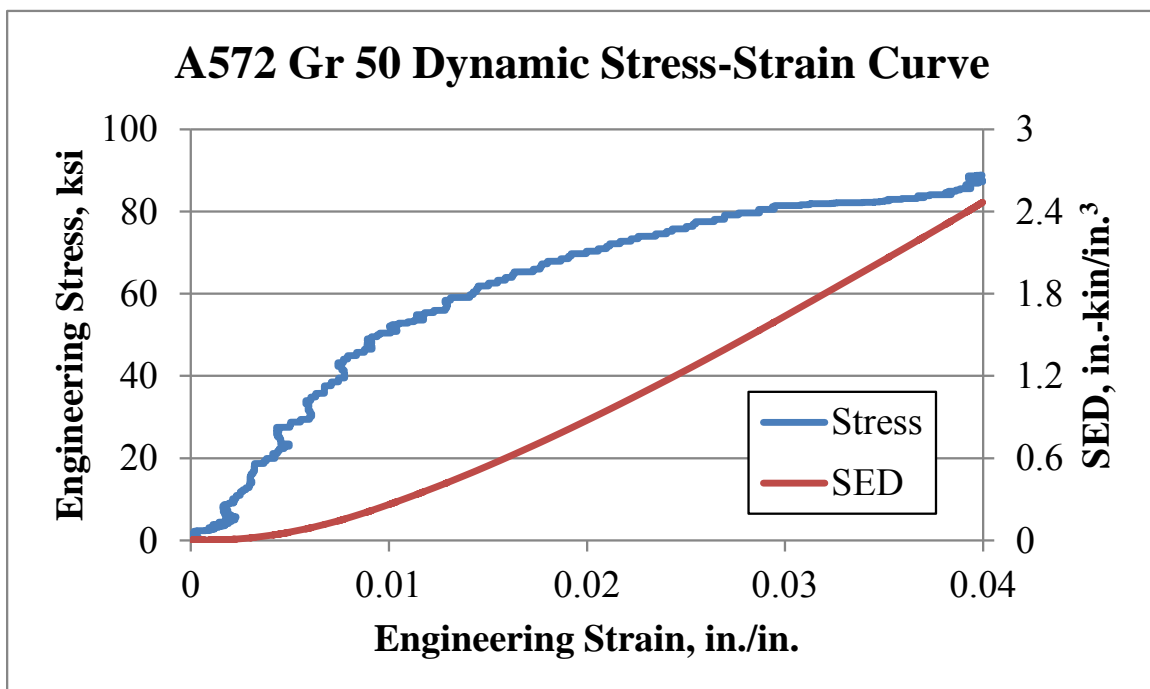


Figure 40. Stress vs. Strain, Test No. DFS-L2



Figure 41. Post-Impact Photographs, Test No. DFS-L2

### 6.2.3 Test No. DFS-L3

During test no. DFS-L3, the bogie reached a speed of 12.1 mph (19.5 km/h), causing nearly uniaxial tension in the coupon. After the test, the gauge length was measured at  $9\frac{3}{4}$  in. (247.7 mm), which was identical to the pre-test gauge length. During the test, load cell data provided a maximum tensile force of 32.8 kips (146 kN), which was very near the rated tensile yield force of 32 kips. The maximum force in this test corresponded to a maximum stress of 64.5 ksi (445 MPa), which was slightly higher than the yield stress determined from quasi-static tensile testing and reported in the mill certificate of conformity. Since the coupon was loaded dynamically, and since there was no measureable permanent deformation, it was concluded that the coupon was not stressed beyond its elastic limit.

#### **6.2.4 Test No. DFS-L3-2**

During test no. DFS-L3-2, the bogie reached a speed of 22.5 mph (36.2 km/h), causing nearly uniaxial tension in the coupon. The same coupon from test no. DFS-L3 was loaded past its elastic limit and experienced necking in the critical section on the side of the load application. Ductile failure was observed in the coupon, wherein the surface of the fracture was nearly at a 45-degree angle. Additional evidence of plasticity was found due to the plastic spray paint being melted off of the coupon near the location of the fracture; heat generation can be significant in plastic deformation.

Force-deflection and energy-deflection curves were created from the load cell data and high-speed video analysis and are shown in Figure 42. Yield occurred at 33 kips (147 kN) and increased until an ultimate force of 38 kips (169 kN) was observed at a displacement of 2.82 in. (7.2 cm) through the gauge length, resulting in an ultimate strain of 0.289 in./in. (mm/mm). At this displacement, the coupon absorbed 104 k-in. (11.8 kJ) of energy. The strain energy density at fracture was 21.0 in.-kip/in.<sup>3</sup> (145.0 mm-N/mm<sup>3</sup>). The stress-strain curve used in determining the SED is shown in Figure 43. Photographs of coupon damage are shown in Figure 44.

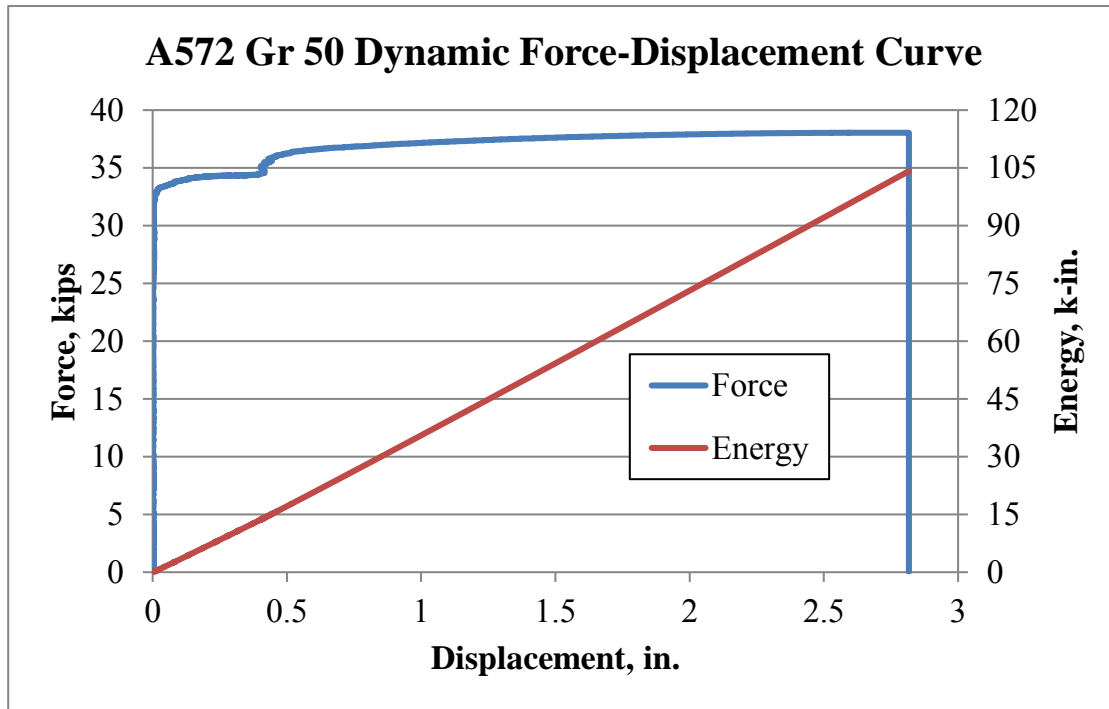


Figure 42. Force vs. Deflection and Energy vs. Deflection, Test No. DFS-L3-2

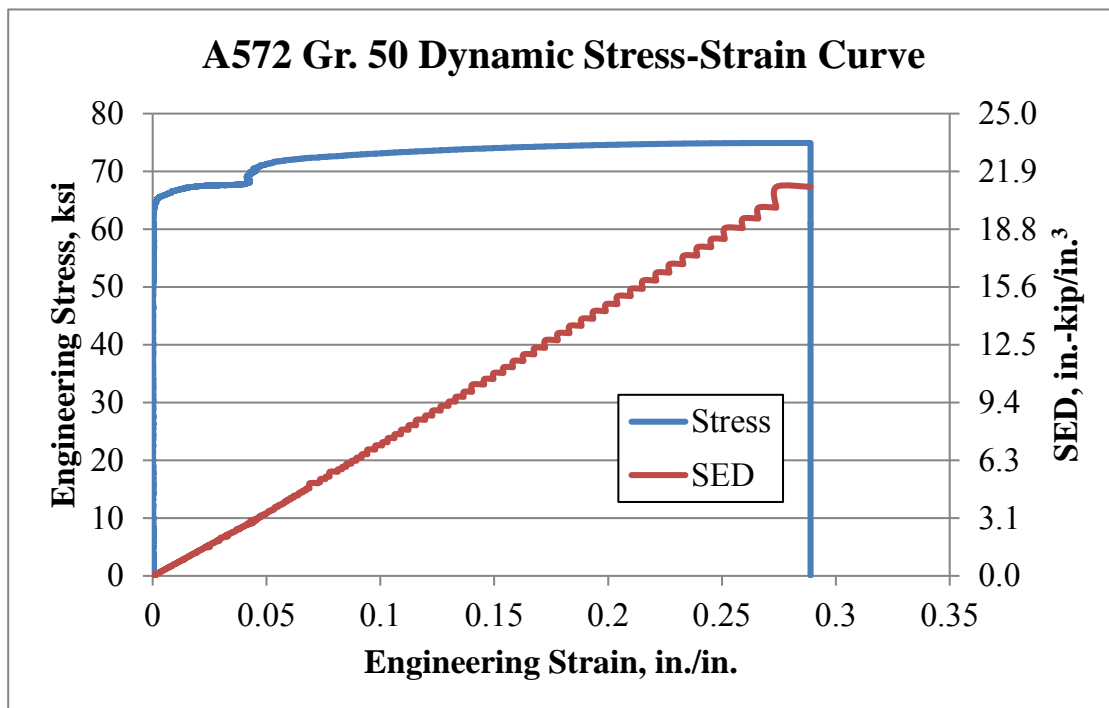


Figure 43. Stress vs. Strain, Test No. DFS-L3-2



Figure 44. Post-Impact Photographs, Test No. DFS-L3-2

#### 6.2.5 Test No. DFS-L4

During test no. DFS-L4, the bogie reached a speed of 16.0 mph (25.7 km/h), causing nearly uniaxial tension in the coupon. The thinner steel coupon ruptured along an angle of approximately 30 degrees, which occurred on the fixed support side of the coupon. Very little necking was observed in the coupon. An ultimate strain of 0.240 was observed. However, there was a significant amount of plastic deformation around each bolt hole.

Force-deflection and energy-deflection curves were created from the load cell data and high-speed video analysis and are shown in Figure 45. Yield occurred at 12.2 kips (54.2 kN) and

increased until an ultimate force of 16.1 kips (71.6 kN) was observed at a displacement of 2.34 in. (5.9 cm), resulting in an ultimate strain of 0.240 in./in. (mm/mm). At this displacement, the coupon absorbed 32.1 k-in. (3.6 kJ) of energy. The strain energy density at fracture was 13.9 in.-kip/in.<sup>3</sup> (96.0 mm-N/mm<sup>3</sup>). The stress-strain curve used in determining the SED is shown in Figure 46. Photographs of coupon damage are shown in Figure 47.

Displacements were measured through the gauge length, but forces were recorded by load cells. As a result, the measured forces were experienced throughout the coupon. With a narrow cross-section, higher stresses would occur in the critical section. It was assumed that fracture in this region would occur before damage would accumulate anywhere else in the coupon. However, that was not the case for this test. Instead, some energy was absorbed in the plastic deformation of the bolt holes. However, the forces measured by the load cells were experienced equally throughout the coupon, and displacements were only measured relative to the gauge length. Therefore, the force-displacement curves were indicative of the energy in the critical section, as well as the corresponding stress-strain curve.

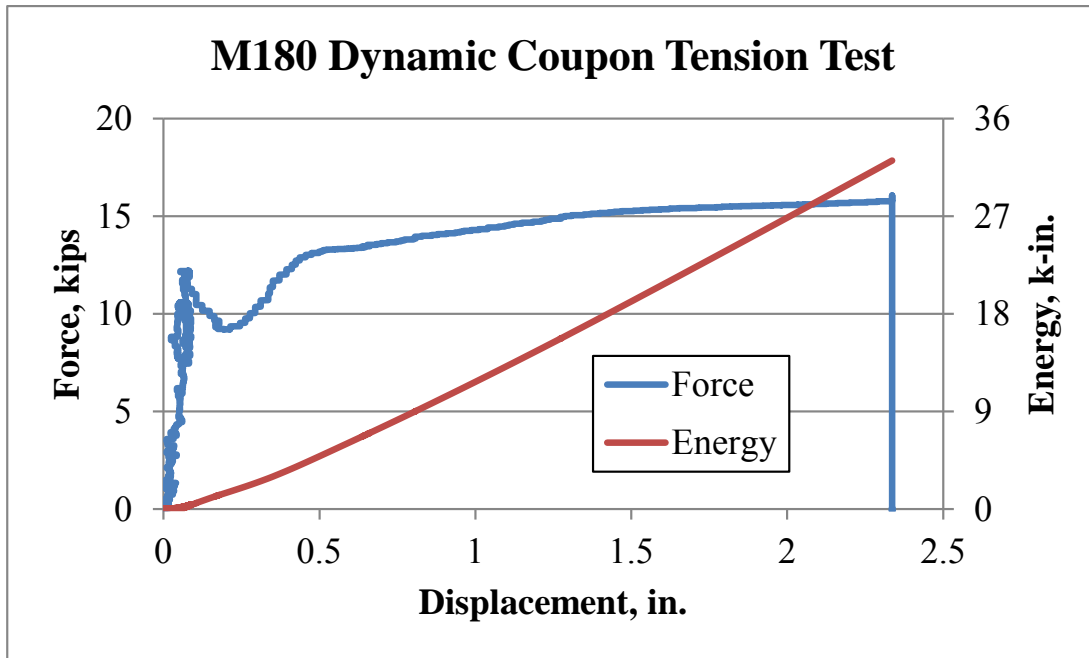


Figure 45. Force vs. Deflection and Energy vs. Deflection, Test No. DFS-L4

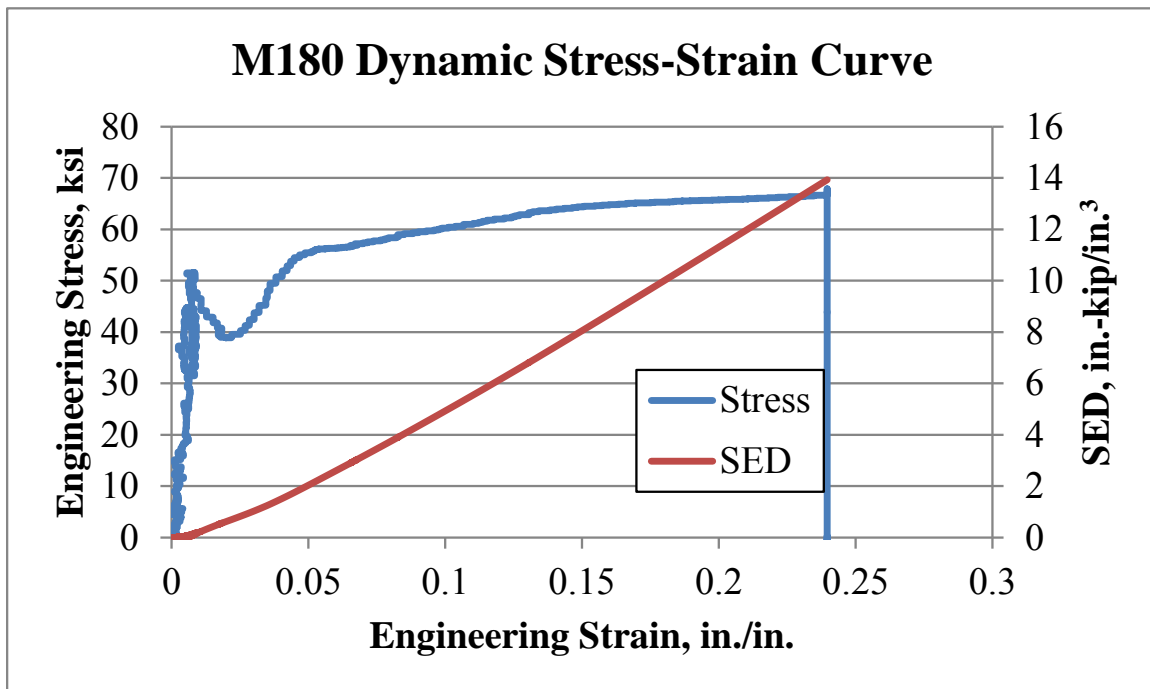


Figure 46. Stress vs. Strain, Test No. DFS-L4





Figure 47. Post-Impact Photographs, Test No. DFS-L4

#### 6.2.6 Test No. DFS-L5

During test no. DFS-L5, the bogie reached a speed of 16.0 mph (25.7 km/h), causing nearly uniaxial tension in the coupon. The thinner steel coupon ruptured along an angle of approximately 45 degrees, which occurred on the loaded side of the coupon. Very little necking was observed in the coupon.

Force-deflection and energy-deflection curves were created from the load cell data and high-speed video analysis and are shown in Figure 48. Yield occurred at 14.3 kips (63.6 kN) and increased until an ultimate force of 14.7 kips (65.4 kN) was observed at a displacement of 2.11 in. (5.4 cm), resulting in an ultimate strain of 0.216 in./in. (mm/mm) through the gauge length. At this displacement, the coupon absorbed 28.9 k-in. (3.3 kJ) of energy. The strain energy density at fracture was 13.6 in.-kip/in.<sup>3</sup> (93.9 mm-N/mm<sup>3</sup>). The stress-strain curve used in determining the SED is shown in Figure 49. Photos of coupon damage are shown in Figure 50.



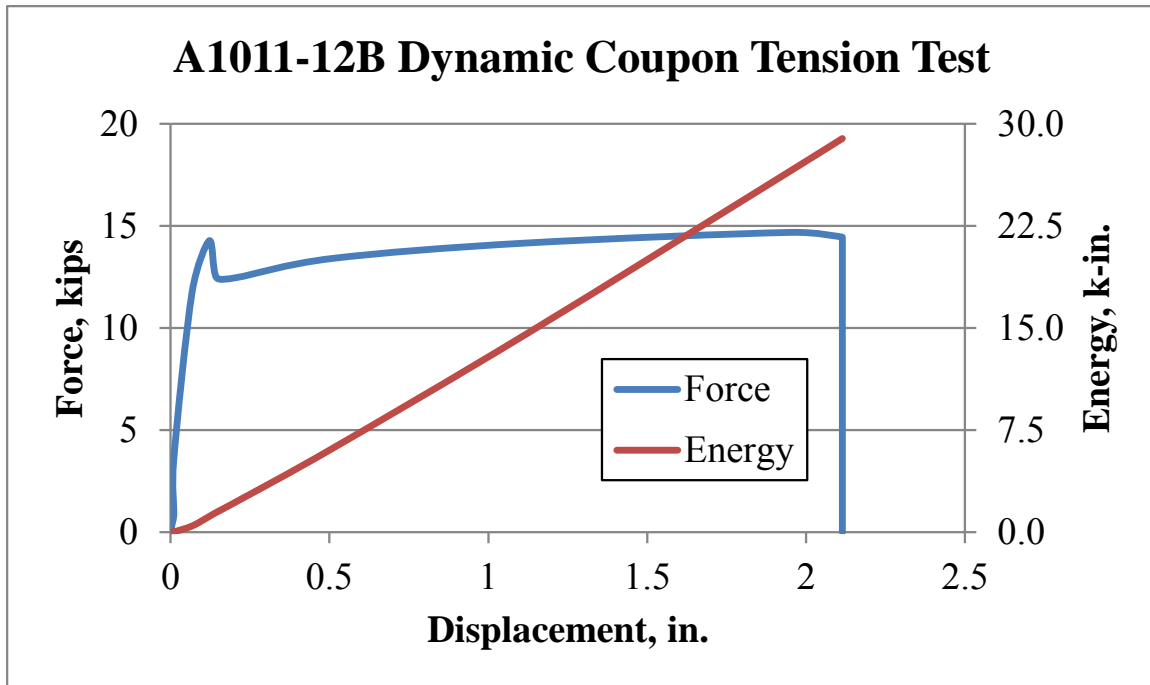


Figure 48. Force vs. Deflection and Energy vs. Deflection, Test No. DFS-L5

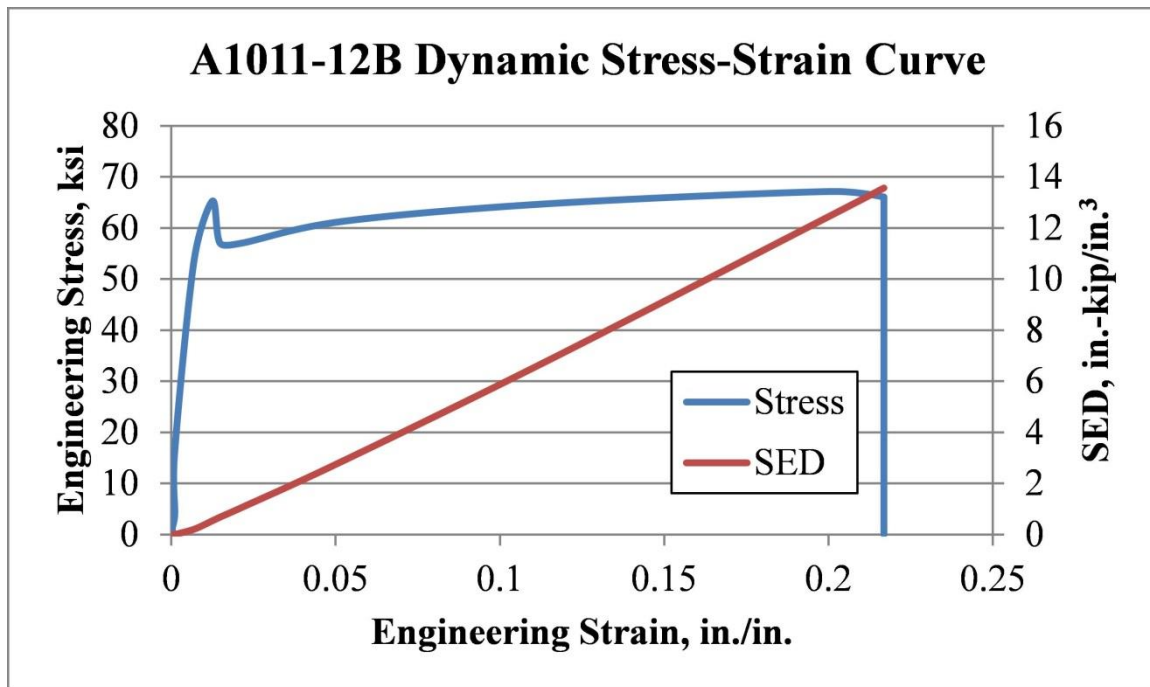


Figure 49. Stress vs. Strain, Test No. DFS-L5



Figure 50. Post-Impact Photographs, Test No. DFS-L5

#### 6.2.7 Test No. DFS-L6

During test no. DFS-L6, the bogie reached a speed of 15.2 mph (24.5 km/h), causing nearly uniaxial tension in the coupon. The coupon was loaded past its elastic limit around the hole and experienced very little necking and even less deformation away from the hole. Highly localized ductile failure was observed around the hole, and additional evidence of plasticity was found due to the plastic spray paint being melted off of the coupon near the location of the fracture; and heat generation can be significant in plastic deformation.

Force-deflection and energy-deflection curves were created from the load cell data and high-speed video analysis and are shown in Figure 51. Yield occurred at 9.9 kips (44.0 kN) and increased until an ultimate force of 11.1 kips (49.4 kN) was observed at a displacement of 0.87 in. (2.2 cm), resulting in an ultimate strain of 0.089 in./in. (mm/mm) through the gauge length. At this

displacement, the coupon absorbed 4.3 k-in. (0.5 kJ) of energy. The strain energy density at fracture was 2.4 in.-kip/in.<sup>3</sup> (16.6 mm-N/mm<sup>3</sup>). The stress-strain curve used in determining the SED is shown in Figure 52. Photographs of coupon damage are shown in Figure 53.

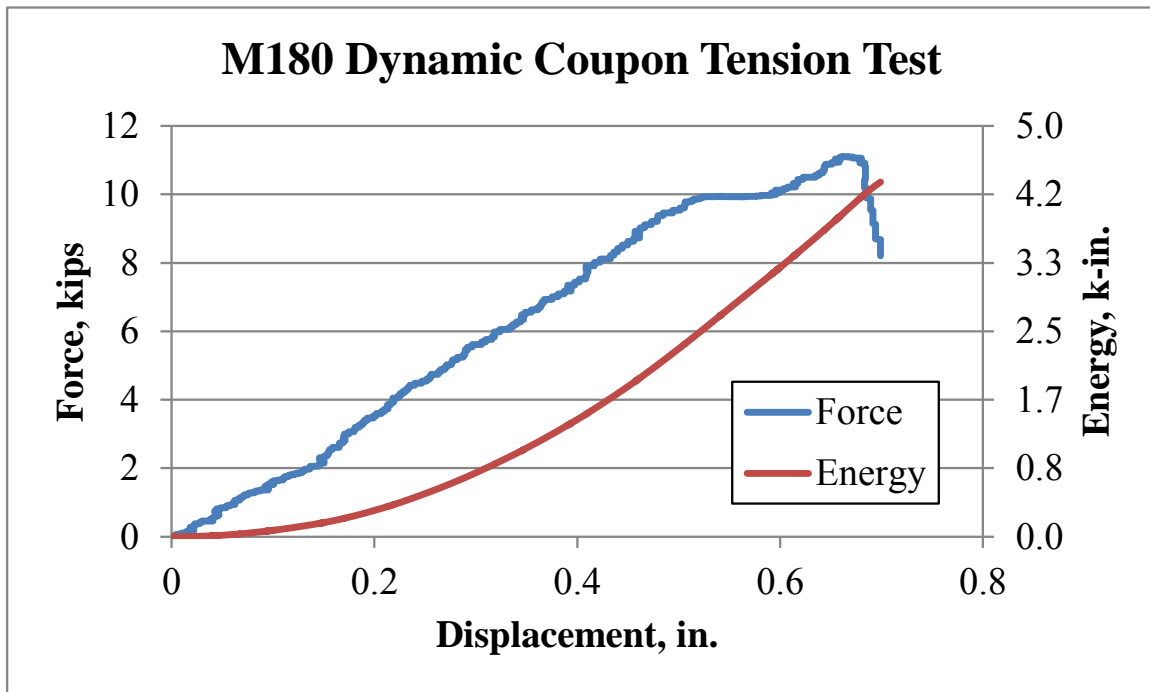


Figure 51. Force vs. Deflection and Energy vs. Deflection, Test No. DFS-L6

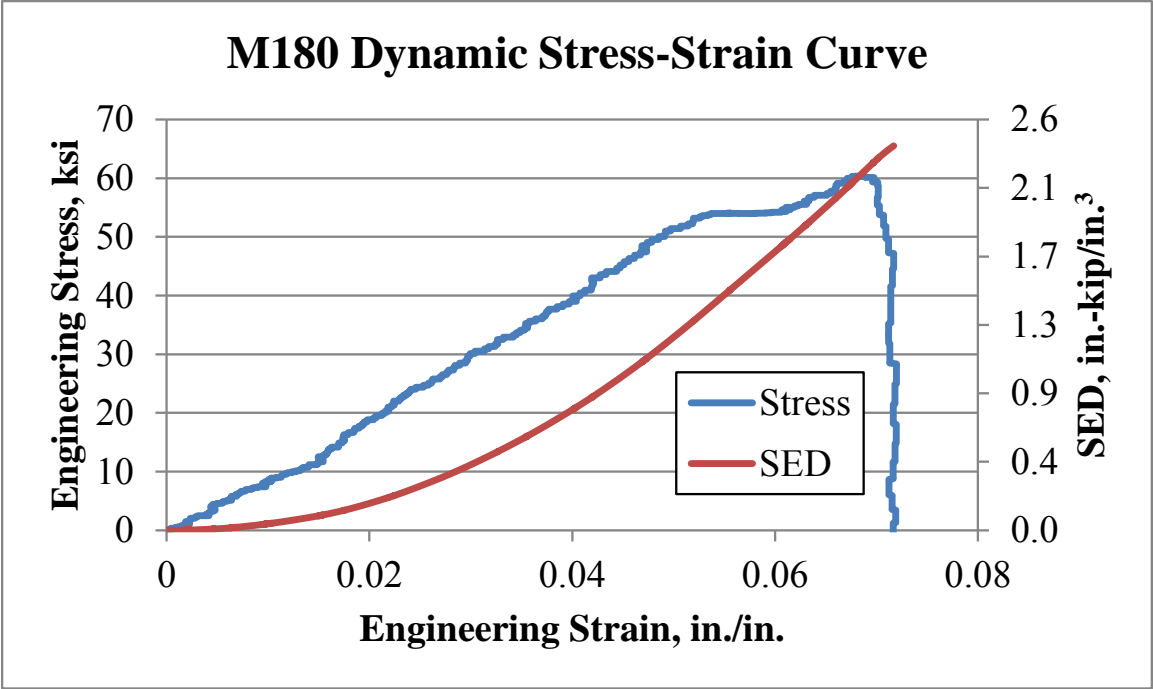


Figure 52. Stress vs. Strain, Test No. DFS-L6



Figure 53. Post-Impact Photographs, Test No. DFS-L6

### 6.2.8 Test No. DFS-L7

During test no. DFS-L7, the bogie reached a speed of 16.0 mph (25.7 km/h), causing nearly uniaxial tension in the coupon. The coupon was loaded past its elastic limit around the hole and experienced very little necking and even less deformation away from the hole. Highly localized ductile failure was observed around the hole, and additional evidence of plasticity was found in the observation that the plastic spray paint melted off of the coupon near the location of the fracture; heat generation can be significant in plastic deformation.

Force-deflection and energy-deflection curves were created from the load cell data and high-speed video analysis and are shown in Figure 54. Yield occurred at 8.6 kips (38.3 kN) and increased until an ultimate force of 10.4 kips (46.3 kN) was observed at a displacement of 0.14 in. (0.4 cm), resulting in an ultimate strain of 0.014 in./in. (mm/mm) through the gauge length. At this displacement, the coupon absorbed 1.2 k-in. (0.1 kJ) of energy. The strain energy density at fracture was 0.8 in.-kip/in.<sup>3</sup> (5.5 mm-N/mm<sup>3</sup>). The stress-strain curve used in determining the SED is shown in Figure 55. Photographs of coupon damage are shown in Figure 56.

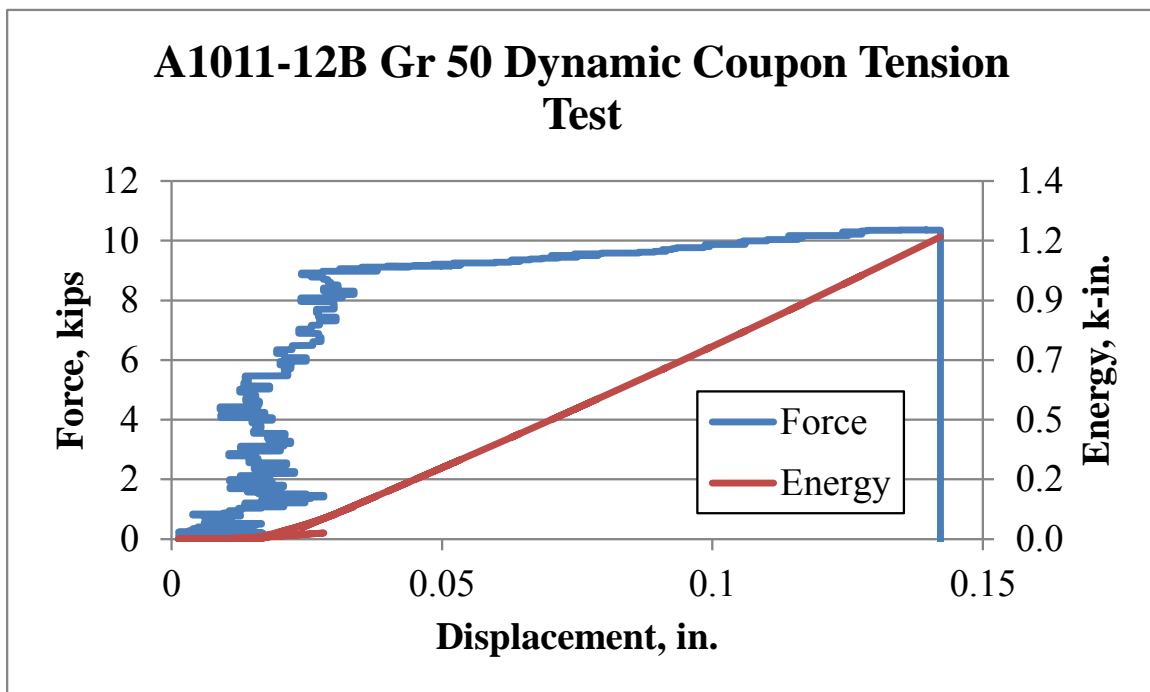


Figure 54. Force vs. Deflection and Energy vs. Deflection, Test No. DFS-L7



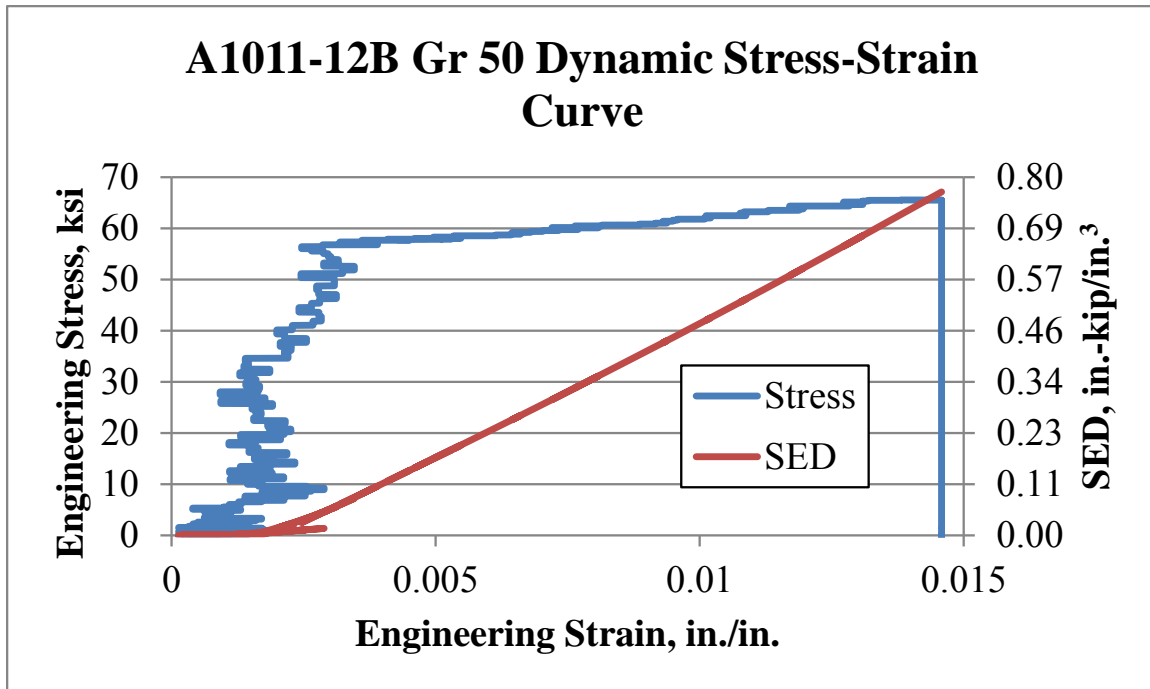


Figure 55. Stress vs. Strain, Test No. DFS-L7



Figure 56. Post-Impact Photographs, Test No. DFS-L7

### **6.2.9 Test No. DFS-T1**

During test no. DFS-T1, the bogie reached a speed of 23.5 mph (37.8 km/h), causing nearly uniaxial tension in the coupon. The coupon was loaded past its elastic limit and experienced necking in the critical section on the side of the load application. Ductile failure was observed in the coupon, wherein the surface of the fracture was nearly at a 45-degree angle. Additional evidence of plasticity was found in the plastic spray paint that was melted off of the coupon near the location of the fracture; heat generation can be significant in plastic deformation.

Force-deflection and energy-deflection curves were created from the load cell data and high-speed video analysis and are shown in Figure 57. Yield occurred at 35 kips (156 kN) and increased until an ultimate force of 37.9 kips (169 kN) was observed at a displacement of 2.93 in. (7.4 cm), resulting in an ultimate strain of 0.301 in./in. (mm/mm) through the gauge length. At this displacement, the coupon absorbed 100.3 k-in. (11.4 kJ) of energy. The strain energy density at fracture was 20.3 in.-kip/in.<sup>3</sup> (140.2 mm-N/mm<sup>3</sup>). The stress-strain curve used in determining the SED is shown in Figure 58. Photographs of coupon damage are shown in Figure 59.



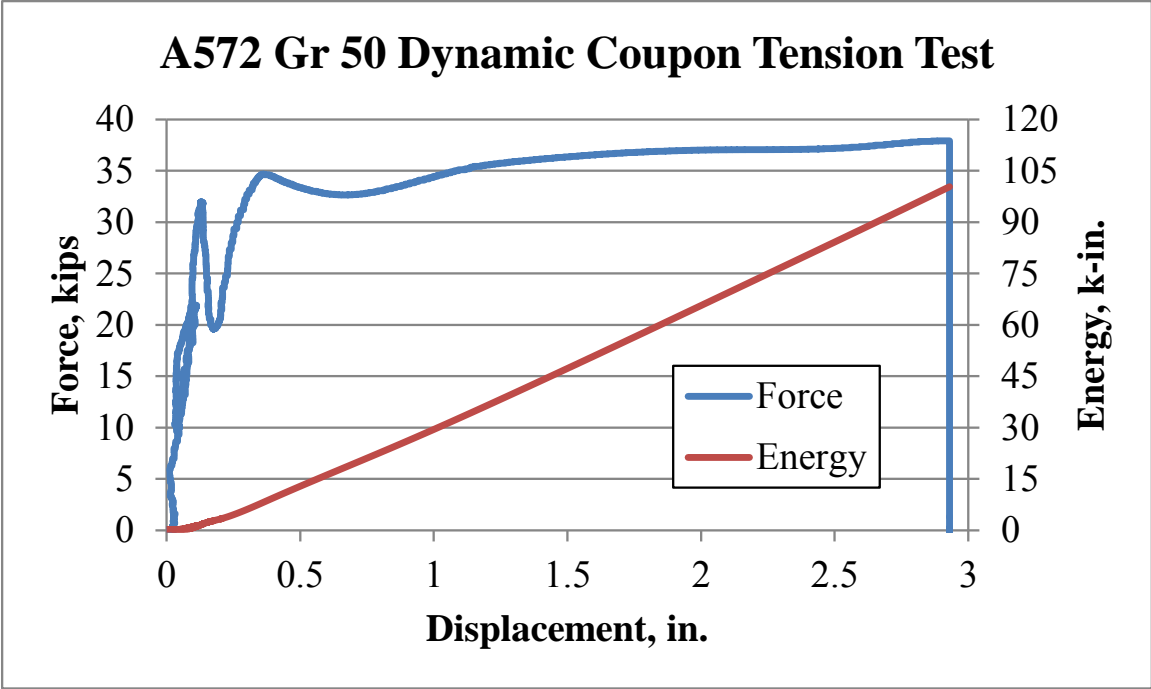


Figure 57. Force vs. Deflection and Energy vs. Deflection, Test No. DFS-T1

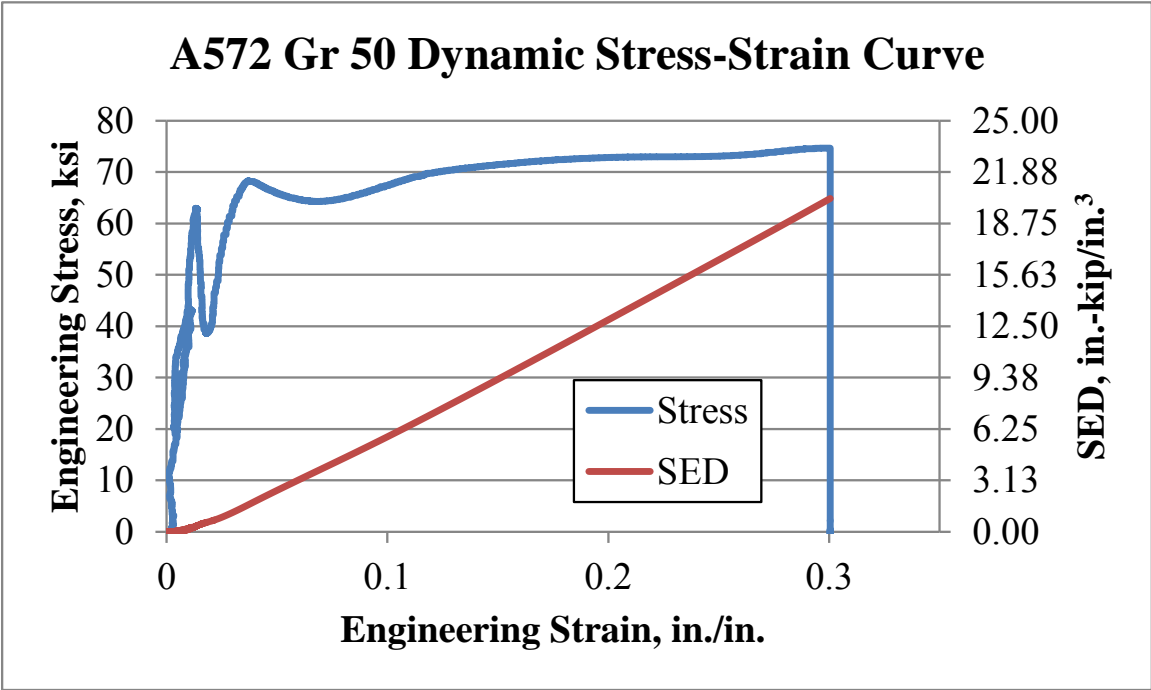


Figure 58. Stress vs. Strain, Test No. DFS-T1



Figure 59. Post-Impact Photographs, Test No. DFS-T1

#### 6.2.10 Test No. DFS-T2

During test no. DFS-T2, the bogie reached a speed of 24.1 mph (38.8 km/h), causing nearly uniaxial tension in the coupon. The coupon was loaded past its elastic limit and experienced necking in the critical section on the side of the load application. Ductile failure was observed in the coupon, wherein the surface of the fracture was nearly at a 45-degree angle. Additional evidence of plasticity was found in the plastic spray paint that was melted off of the coupon near the location of the fracture; heat generation can be significant in plastic deformation.

Force-deflection and energy-deflection curves were created from the load cell data and high-speed video analysis and are shown in Figure 60. Yield occurred at 33 kips (147 kN) and increased until an ultimate force of 38.7 kips (173 kN) was observed at a displacement of 2.51 in. (6.4 cm), resulting in an ultimate strain of 0.257 in./in. (mm/mm) through the gauge length. At this displacement, the coupon absorbed 86.8 k-in. (9.8 kJ) of energy. The strain energy density at fracture was 17.5 in.-kip/in.<sup>3</sup> (120.8 mm-N/mm<sup>3</sup>). The stress-strain curve used in determining the SED is shown in Figure 61. Photographs of coupon damage are shown in Figure 62.

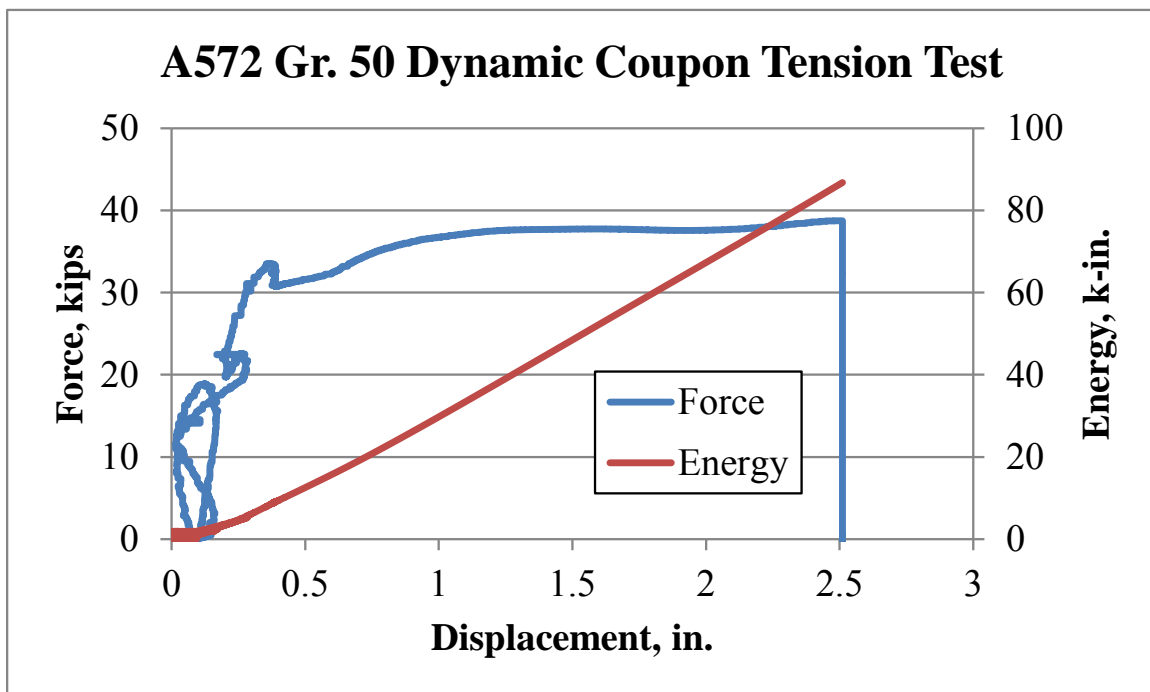


Figure 60. Force vs. Deflection and Energy vs. Deflection, Test No. DFS-T2

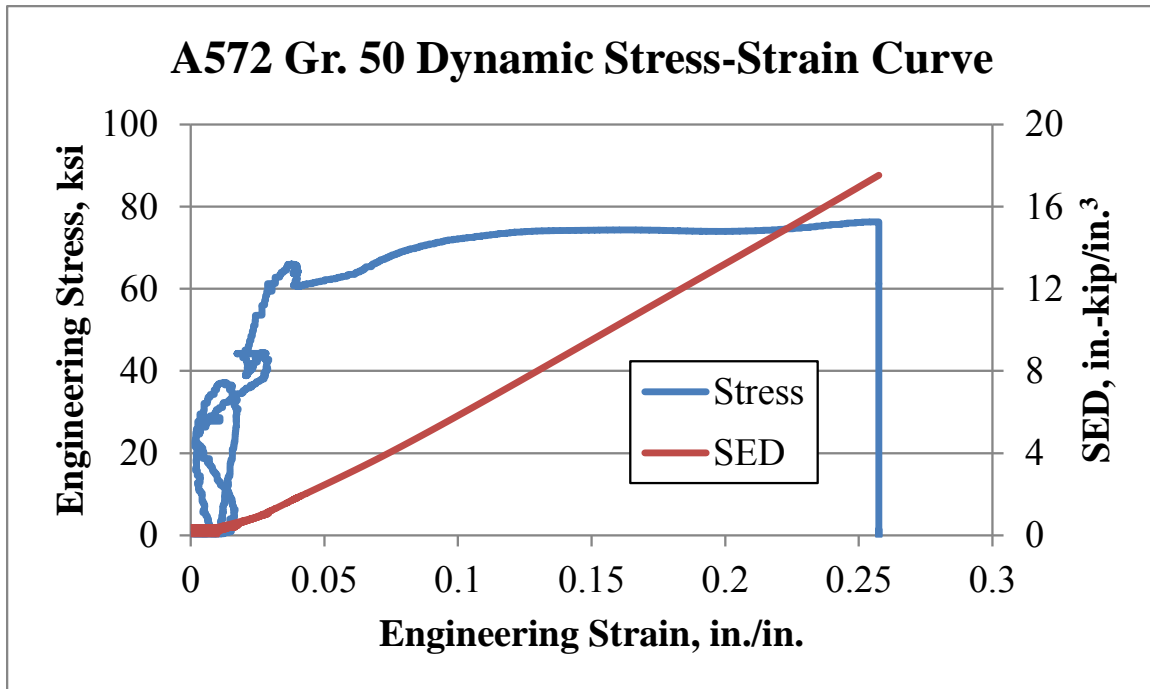


Figure 61. Stress vs. Strain, Test No. DFS-T2



Figure 62. Post-Impact Photographs, Test No. DFS-T2

### **6.2.11 Test No. DFS-T3**

During test no. DFS-T3, the bogie reached a speed of 23.1 mph (37.2 km/h), causing nearly uniaxial tension in the coupon. The coupon was loaded past its elastic limit and experienced necking in the critical section on the side of the load application. Ductile failure was observed in the coupon, wherein the surface of the fracture was nearly at a 45-degree angle. Additional evidence of plasticity was found in the plastic spray paint that was melted off of the coupon near the location of the fracture; heat generation can be significant in plastic deformation.

Force-deflection and energy-deflection curves were created from the load cell data and high-speed video analysis and are shown in Figure 63. Yield occurred at 46.4 kips (206.4 kN) and increased until an ultimate force of 47.6 kips (212 kN) was observed at a displacement of 3.04 in. (7.7 cm), resulting in an ultimate strain of 0.312 in./in. (mm/mm) through the gauge length. At this displacement, the coupon absorbed 143.7 k-in. (16.3 kJ) of energy. The strain energy density at fracture was 29.0 in.-kip/in.<sup>3</sup> (200.2 mm-N/mm<sup>3</sup>). The stress-strain curve used in determining the SED is shown in Figure 64. Photographs of coupon damage are shown in Figure 65. This performance was far different from the preceding test (test no. DFS-T2) of the same material and grain orientation, and the yield stress was so much higher than what was rated in the mill certificate, that this test was considered corrupt and was not used for subsequent comparisons or modeling.

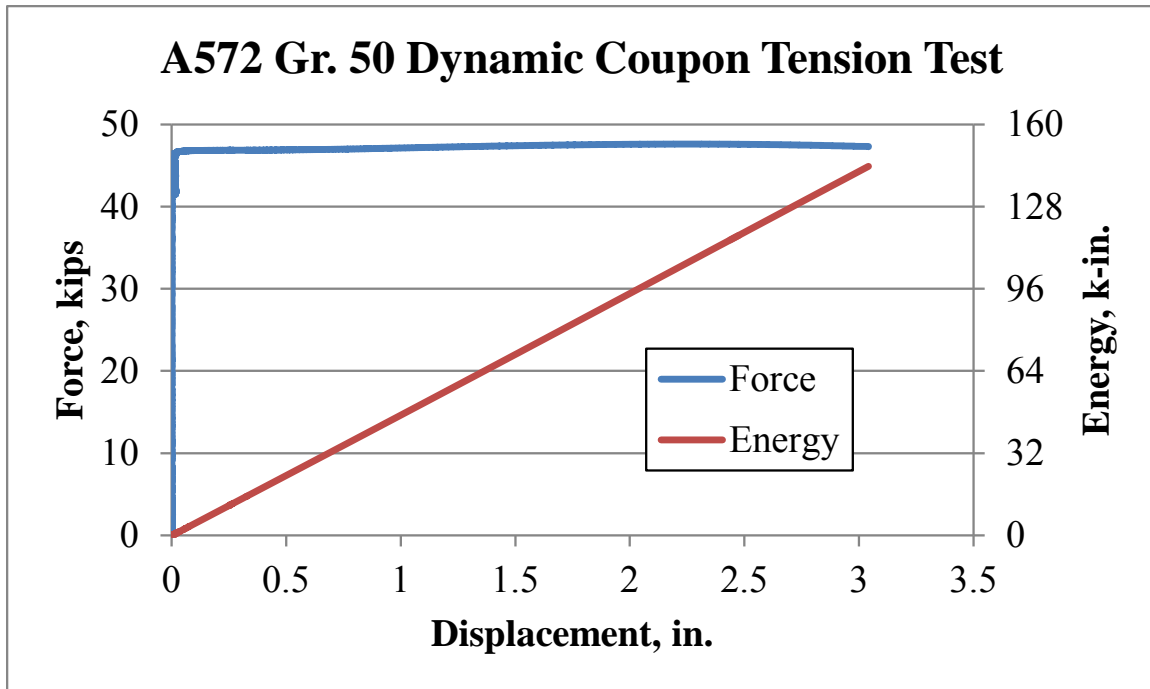


Figure 63. Force vs. Deflection and Energy vs. Deflection, Test No. DFS-T3

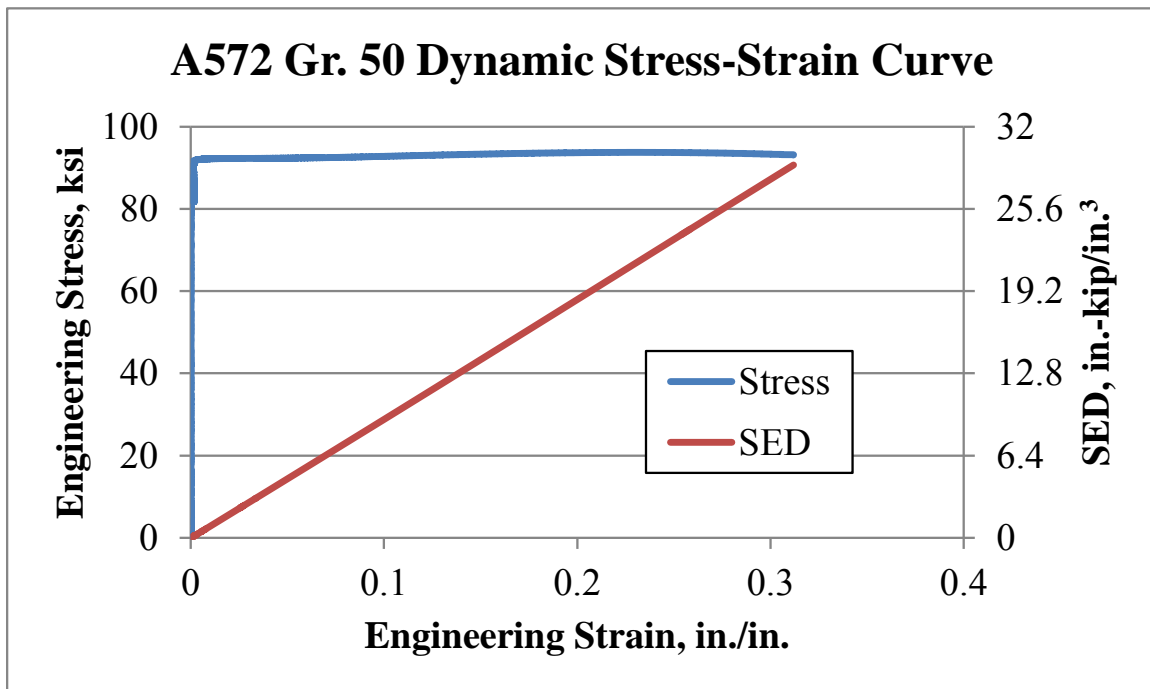


Figure 64. Stress vs. Strain, Test No. DFS-T3





Figure 65. Post-Impact Photographs, Test No. DFS-T3

### 6.3 Summary of Dynamic Tensile Tests

The area under the force-displacement curve represented the energy required to deform the coupon and to fracture it. The area under the stress-strain curve, in contrast, represented the strain energy density in the coupon through its plastic deformation until fracture. The peak loads, deflections, energies, and strain energy densities for each test are summarized in Table 9.

## 6.4 Discussion

Three steel materials were tested in this research: A572 Gr. 50, AASHTO M180, and A1011-12B Gr. 50. Thickness changes were tested, as was the presence of a stress concentration and the grain orientation.

Changes in thickness for Grade 50 steel were analyzed as well. For A572 Gr. 50, thicknesses were  $\frac{5}{16}$  in. (7.9 mm), and for A1011-12B Gr. 50, thicknesses were 10 gauge (3.4 mm). For samples without a stress concentration (test nos. DFS-L3-2 and DFS-L5), ultimate strains were 0.289 and 0.216 in./in. (mm/mm), respectively. Also, strain energy densities at fracture were 21.0 and 13.6 in.-kip/in.<sup>3</sup> (145.0 and 93.9 mm-N/mm<sup>3</sup>), respectively. The dramatic difference in strain energy density was particularly interesting, and because of the difference, this geometrical difference was modeled with LS-DYNA.

All three materials included stress concentrations in the form of holes drilled in the center of the critical cross section. For A572 Gr. 50, tests DFS-L1 and L2 had concentrations, but L3-2 did not. Ultimate strains were 0.022 and 0.032 in./in. (mm/mm), compared to 0.289 in./in. (mm/mm). Strain energy densities were 1.6 and 2.2 in.-kip/in.<sup>3</sup> (11.0 and 15.2 mm-N/mm<sup>3</sup>), compared to 21.0 in.-kip/in.<sup>3</sup> (145.0 mm-N/mm<sup>3</sup>). This order-of-magnitude difference clearly indicates the need to separately model the two cases.

Finally, grain orientation was examined for A572 Gr. 50 steel, where the thickness and continuity of the material were constants. Specifically, test no. DFS-L3-2, a longitudinal grain coupon, was compared to test nos. DFS-T1 and DFS-T2, each a transverse grain coupon. The ultimate strain to fracture for test no. DFS-L3-2 was 0.289 in./in. (mm/mm) while the ultimate strains to fracture of test nos. DFS-T1 and DFS-T2 were 0.301 and 0.257 in./in. (mm/mm), respectively. Similarly, strain energy densities at fracture for test nos. DFS-L3-2, DFS-T1, and DFS-T2 were 21.0, 20.3, and 17.5 in.-kip/in.<sup>3</sup> (145.0, 140.2, and 120.8 mm-N/mm<sup>3</sup>), respectively.



Without more testing, it could not be determined if this parameter was significant. Instead, steel was assumed to behave in an isotropic manner, and grain orientation was not considered further.

Table 9. Summary of Dynamic Tensile Test Results

Test Name	Material	Cross Sectional Area, in. <sup>2</sup> (mm <sup>2</sup> )	Peak Load, kip (kN)	Peak Displacement at Fracture, in. (cm)	Energy at Fracture kip-in. (kJ)	$\sigma_y$ , ksi (Mpa)	$\sigma_u$ , ksi (Mpa)	$\epsilon_u$ , in./in. (mm/mm)	SED at Fracture, ksi (Mpa)
DFS-L1	A572 Gr. 50	0.35 (227)	33.1 (147)	0.21 (0.5)	5.31 (0.6)	70.3 (484)	94.2 (649)	0.022	1.6 (11.0)
DFS-L2	A572 Gr. 50	0.35 (227)	31.2 (139)	0.39 (1.0)	7.5 (0.9)	56.9 (392)	88.7 (612)	0.04	2.4 (16.6)
DFS-L3	A572 Gr. 50	0.51 (328)	32.8 (146)	NA	NA	NA	NA	NA	NA
DFS-L3-2	A572 Gr. 50	0.51 (328)	38.0 (169)	2.82 (7.2)	104 (11.8)	65.0 (448)	74.8 (516)	0.289	21.0 (145.0)
DFS-L4	AASHTO M180	0.24 (152)	16.1 (71.6)	2.34 (5.9)	32.1 (3.6)	51.8 (357)	68.3 (471)	0.24	13.9 (96.0)
DFS-L5	A1011-12B Gr. 50	0.22 (141)	14.7 (65.4)	2.11 (5.4)	28.9 (3.3)	65.4 (451)	67.2 (463)	0.216	13.6 (93.9)
DFS-L6	AASHTO M180	0.18 (118)	11.1 (49.4)	0.87 (2.2)	4.3 (0.5)	54.0 (373)	60.6 (418)	0.089	2.4 (16.6)
DFS-L7	A1011-12B Gr. 50	0.15 (98)	10.4 (46.3)	0.14 (0.4)	1.2 (0.1)	56.8 (392)	68.7 (4740)	0.014	0.8 (5.5)
DFS-T1	A572 Gr. 50	0.51 (328)	37.9 (169)	2.93 (7.4)	100.3 (11.4)	68.9 (475)	74.6 (515)	0.301	20.3 (140.2)
DFS-T2	A572 Gr. 50	0.51 (328)	38.7 (173)	2.51 (6.4)	86.8 (9.8)	65.0 (448)	76.2 (525)	0.257	17.5 (120.8)
DFS-T3	A572 Gr. 50	0.51 (328)	47.6 (212)	2.51 (6.4)	97.0 (11.0)	91.4 (630)	93.7 (630)	0.312	29.0 (200.2)

## 7 NON LOCAL SED FAILURE CRITERION

### 7.1 Strain Energy Density Calculation

As a fundamental law, energy is conserved in the process of relative displacements, and these displacements require some external applied force. The relationship between force and displacement is known as the constitutive relationship. The area under the curve described by this relationship represents the strain energy in the objected being deformed. The exact nature of this energy is given in Equation 7.1:

$$U = \int_0^D F dD \quad (7.1)$$

Where  $U$  = strain energy  
 $F$  = force as a function of the displacement  
 $D$  = displacement

The total strain energy is dependent on the volume of the material, in that a larger object would require more energy than a smaller object to produce the same displacement. Therefore, the strain energy density becomes a more general, and therefore, useful tool. Conceptually, the strain energy density is the strain energy per unit of volume and can be described according to the area under the stress-strain curve, as in Equation 7.2:

$$u = \int_0^\varepsilon \sigma d\varepsilon \quad (7.2)$$

Where  $u$  = strain energy density or SED  
 $\sigma$  = stress  
 $\varepsilon$  = strain

Fracture was predicted when the strain energy density at a location exceeded some critical value particular to that material. A potential disadvantage of this approach is the dependency on mesh density. As aforementioned, the strain energy density is the strain energy per unit of volume. Therefore, as the size of an element gets exceedingly small, the strain energy density increases rapidly, potentially leading to premature fracture prediction. Similarly, if elements are too large, the SED will be too small for the fracture criterion to be met.

To circumvent this drawback, a non-local methodology was adopted, wherein the length scale that defined the non-locality was established to reduce mesh sensitivity in the approximated solution. This length scale was defined as a radius around each node in the body. Conceptually, there was a link between the center node and every other node within that radius that acted like a linearly elastic – perfectly plastic spring. Imagine this spring stretches according to the schematic shown in Figure 66.

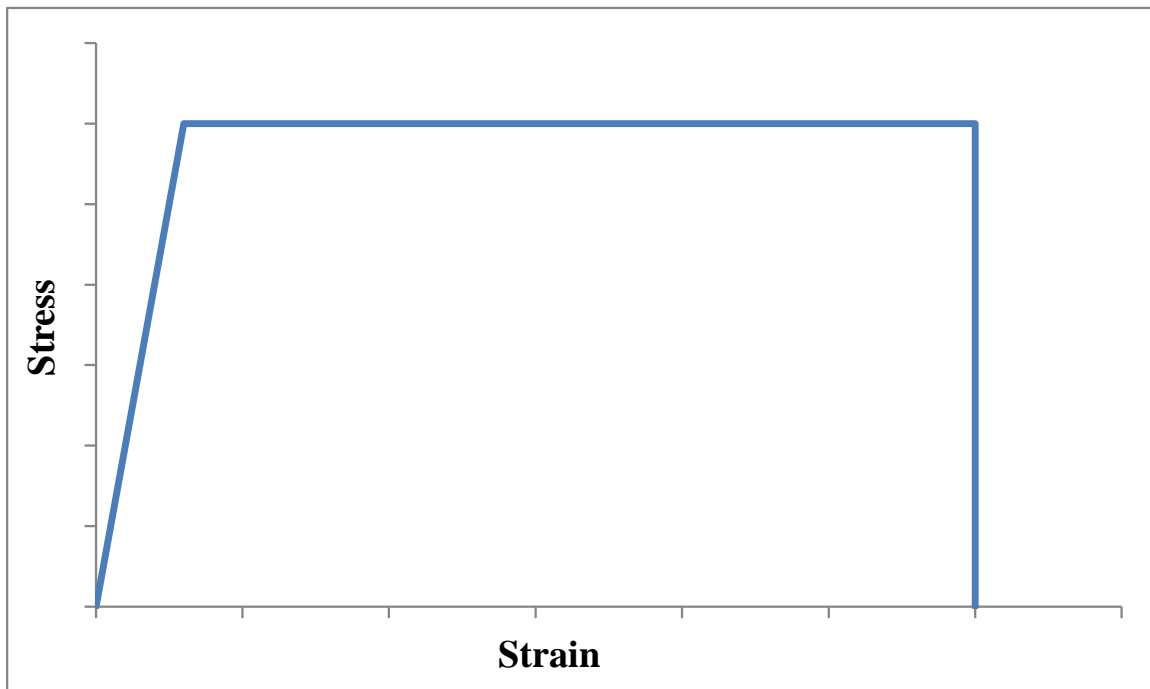


Figure 66. Stress-Strain Curve between Two Nodes

This conceptual stress-strain curve was applied to each node within a radius around a node. The distribution of the nodes throughout a material does not need to be uniform. However, for the sake of demonstration, a uniform grid with a corresponding highlighted length scale is shown in Figure 67. The springs that contribute to the center node are highlighted with bold, dark lines.

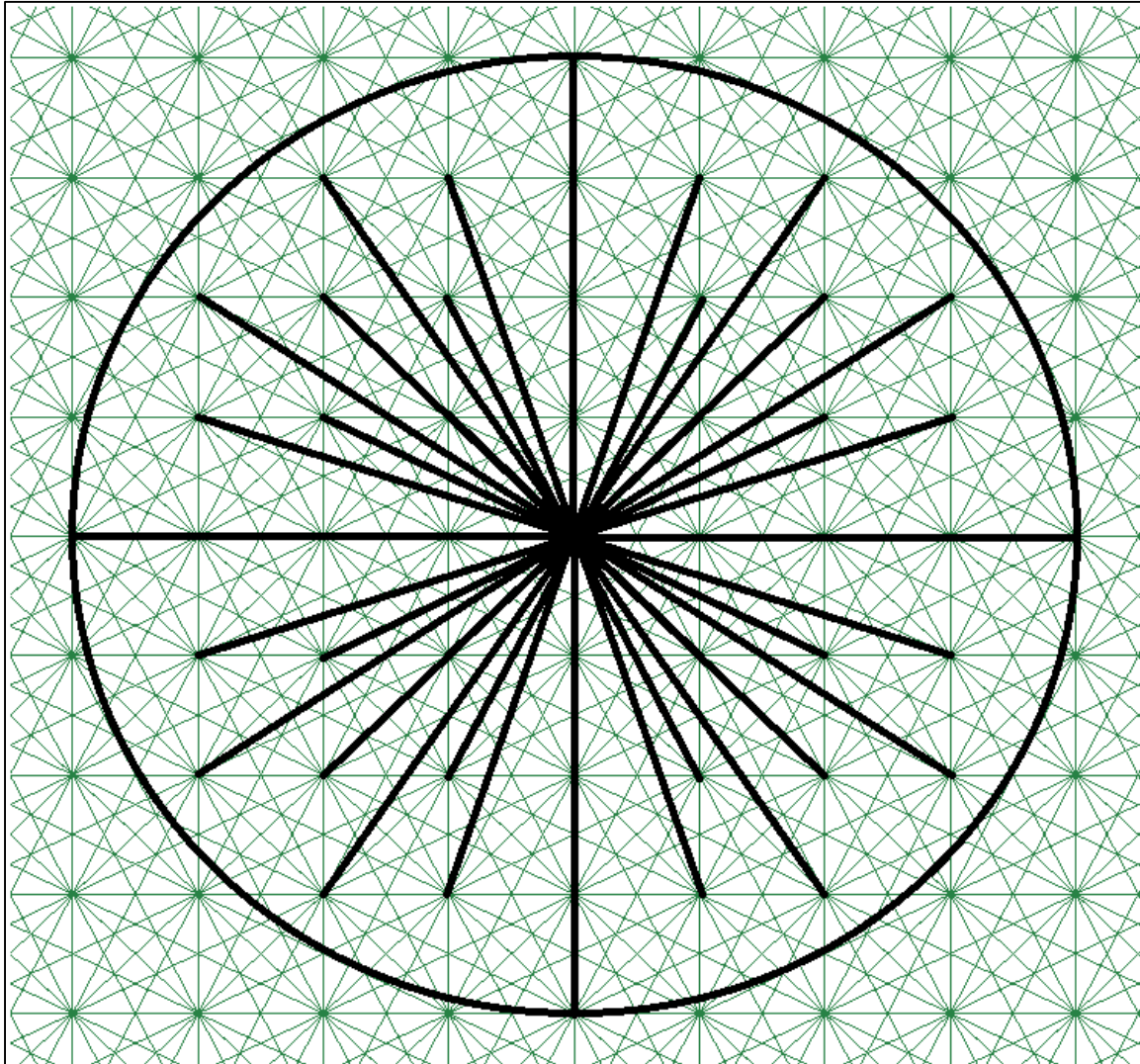


Figure 67. Schematic of Non-Locality around a Node

The strain energy density at the center node is the summation of the strain energy densities in the springs attached to it. Therefore, the spring SEDs were derived from the stress-strain curve

in Figure 66. Recall, the SED is the energy under that curve. Therefore, the SED of each truss is described in Equation 7.3:

$$u_{tr} = \begin{cases} \frac{1}{2}E_{tr}\varepsilon^2 \\ E_{tr}\varepsilon_y(\varepsilon - \varepsilon_y) \end{cases} \quad (7.3)$$

Where  $u_{tr}$  = strain energy density between two nodes, like a truss  
 $E_{tr}$  = truss modulus between two nodes  
 $\varepsilon_y$  = yield strain of the material between two nodes  
 $\varepsilon$  = current strain between two nodes.

Finally, the SED around each node was calculated by summing the SEDs calculated with Equation 7.3. This summation is described in Equation 7.4:

$$u_{node} = \sum_{i=1}^n (u_{tr})_i \quad (7.4)$$

Where  $n$  = number of nodes within the length scale  
 $i$  = node-of-interest

## 7.2 Calculating $E_{tr}$

The stress-strain relationship between two nodes comprises a part of the sum for the non-local methodology. This relationship has an elastic part and a plastic part. The elastic part is governed by the stiffness of the truss, whereas the plastic part was assumed to be a perfectly plastic model, as shown in Figure 66. Therefore, the elastic stiffness of the truss needed to be determined, but its influence on the total calculations would be minimal, since the strain energy through the elastic region is much smaller than the contribution from the plastic region. Macek and Silling

developed a coupled version of the FEM with a non-local method known as peridynamics [52].

To do so, the relationship between two nodes was, in part, described by the following stiffness:

$$E_{tr} = c\Delta x^4 \quad (7.5)$$

$$c = \frac{18E}{\pi\delta^4} \quad (7.6)$$

Where  $E_{tr}$  = effective stiffness of the truss  
 $\Delta x$  = nodal spacing of a uniform mesh  
 $c$  = force-stretch compliance of a truss  
 $E$  = Young's Modulus of the material

To account for weakness in the modulus near free edges, Macek and Silling proposed an increase factor based on eigenvalues for an infinitely large plate and the same eigenvalues for the plate being investigated [52]. A similar increase was adopted in this research, but the approach was simplified by increasing the modulus according to the number of trusses defined within the length scale. This was essentially done by determining the number of possible trusses in a body at a point sufficiently far from the edge, and then this maximum value was divided by the number of trusses within the length scale of the node-of-interest. For nodes far from the edge, the factor was 1.0. However, for nodes close to free edges, the effective stiffness in the trusses was defined by Equation 7.7, where it was assumed that  $\delta = 3\Delta x$ :

$$E_{tr}(i) = \frac{2E}{9\pi} \left[ \frac{count_{max}}{count(i)} \right] \quad (7.7)$$

Where  $E_{tr}(i)$  = effective stiffness of the truss at node  $i$   
 $count_{max}$  = number of trusses around a node far from any edges  
 $count(i)$  = number of trusses around node  $i$

## **7.3 Failure Criterion**

### **7.3.1 General**

High, localized strains near the point of failure in a steel tensile sample indicate that the overall strain energy density in the sample is also high and localized. Applying this principle to the non-local SED technique, the length scale was instrumental in determining the overall effect of necking on the failure of the part. In particular, for very large length scales, the behavior of the material inside the length scale would not be significantly different from the overall behavior of the material. In other words, the overall global SED at fracture would be uniform through the material, effectively filtering the localized deformation from necking out of the analysis. Therefore, a proposed critical non-local SED was developed empirically by setting the length scale equal to a prescribed increment of the nodal spacing and altering the critical SED until the overall behavior of the model matched the SED behavior of the physical testing for the A572 steel coupon. Initially, a factor had to be applied to increase the global SED such that the failure in the post-processing code matched the overall failure of the physical tests. For length scale radii of 2, 3, 4, and 5 times the nodal spacing, a logarithmic relationship was developed between this scaling factor and the nodal spacing itself, as shown in Figure 68, where the logarithmic expressions are for radii of 5, 4, 3, and 2 in descending order.



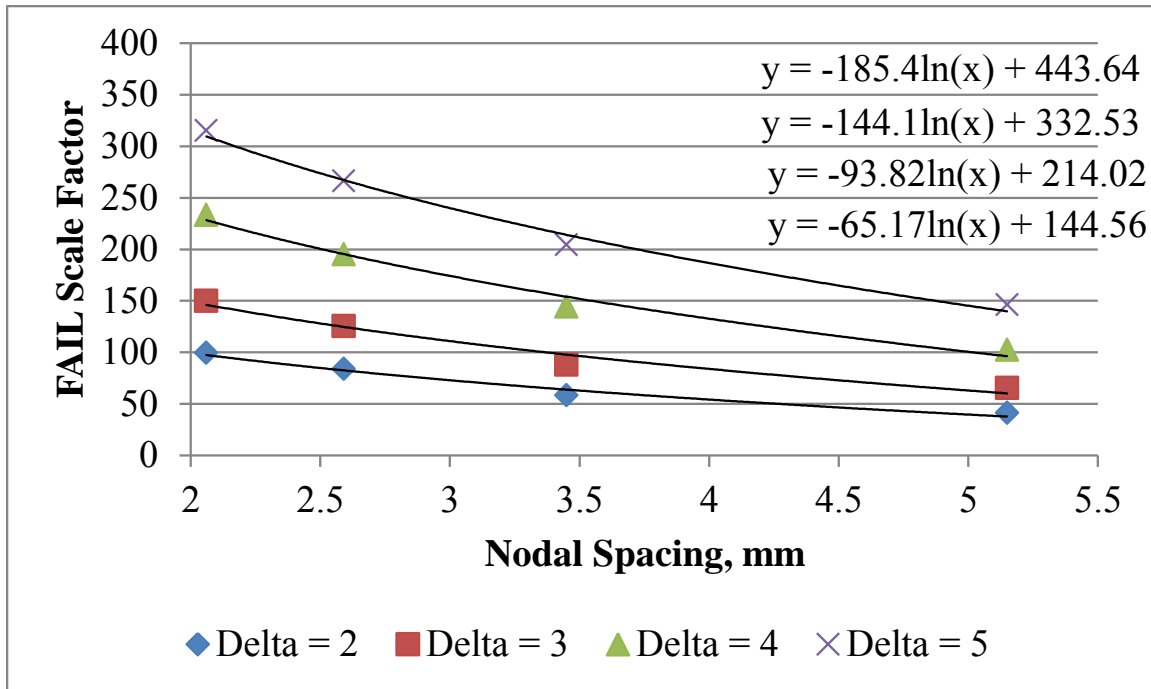


Figure 68. Logarithmic Expressions of Non-Local Critical SED

The coarsest mesh did not follow the trends established by the other four meshes and was excluded from further analysis, therefore requiring at least more than 4 elements through the narrowest portion of the model. From Figure 68, the differences at each individual nodal spacing are approximately exponential in nature. Therefore, a simplified expression was developed using  $\delta = 5.0$  as a baseline, from which the scale factor for the failure parameter can be determined. The exponential proportions are reported in Table 10, and shown graphically in Figure 69, where the exponential expression was determined from the average proportions at each delta magnifier.

Table 10. Exponential Proportion of the Scaled Failure Parameter

Delta Magnifier	Mesh 2	Mesh 3	Mesh 4	Mesh 5	Averages
2	0.315	0.314	0.284	0.280	0.298
3	0.476	0.471	0.431	0.450	0.457
4	0.740	0.733	0.706	0.700	0.720
5	1.000	1.000	1.000	1.000	1.000

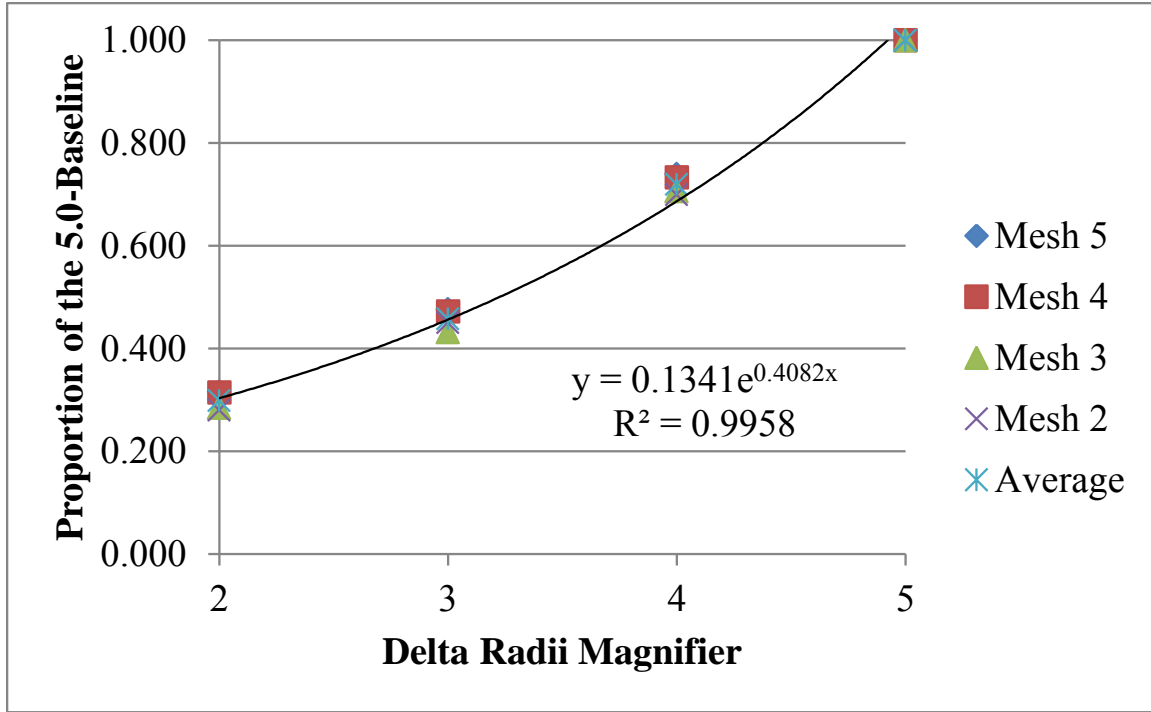


Figure 69. Exponential Proportion of the Scaled Failure Parameter

Finally, the proposed failure parameter was determined from the non-local length scale, which was defined as the nodal spacing multiplied by the delta magnifier. The critical SED in the non-local radius was a function of the delta magnifier and the nodal spacing, as shown in Equation 7.8:

$$SED_{crit} = SED_{fail}(-185.4 \ln(\Delta x) + 443.64) \times 0.1341e^{0.4082D} \quad (7.8)$$

Where

- $SED_{crit}$  = non local SED at the initiation of fracture
- $SED_{fail}$  = global SED at the initiation of fracture
- $\Delta x$  = nodal spacing in millimeters
- $D$  = delta magnifier

The failure criterion holds that when the non-local strain energy density, as determined by Equation 7.4, exceeds some critical value, then a fracture surface has been created at or near the center node. Mathematically, this is described in Equation 7.9:

$$SED_{crit} - u_{node} \leq 0 \quad (7.9)$$

The critical SED must be determined for each material. In this study, steel tensile data was used to calibrate the model such that the global strain energy density in the model matched the global strain energy density of the physical tensile test. Here, the reference to the global strain energy density was an average SED at the point of fracture. Therefore, the SED is not uniform, else fracture would occur simultaneously at numerous points. Since this does not happen, it holds that the SED at fracture must be higher than the overall SED in the material, as assumed in Equation 7.8. It also holds that the critical SED in the model is a function of the length scale.

Using LS-DYNA, nodal displacements through the gauge length were recorded and output as an ASCII file called “nodout.” This file was read by a post-processing program written by the author and included in Appendix C. This program also requires an LS-DYNA-style input deck for the \*NODE card describe the initial positions of all the nodes in the gauge length. An example of the nodal position input file is given in Appendix D. Finally, an input text file is required to enter specifics of the model, and an example is given in Appendix E.

### **7.3.2 A572 Gr 50**

Each delta magnifier was studied with each mesh density to determine mesh sensitivity for internal energy of the gauge length, cross-sectional force, gauge length displacement, and SED. The plots of each of these are given in Figures 70 through 73.

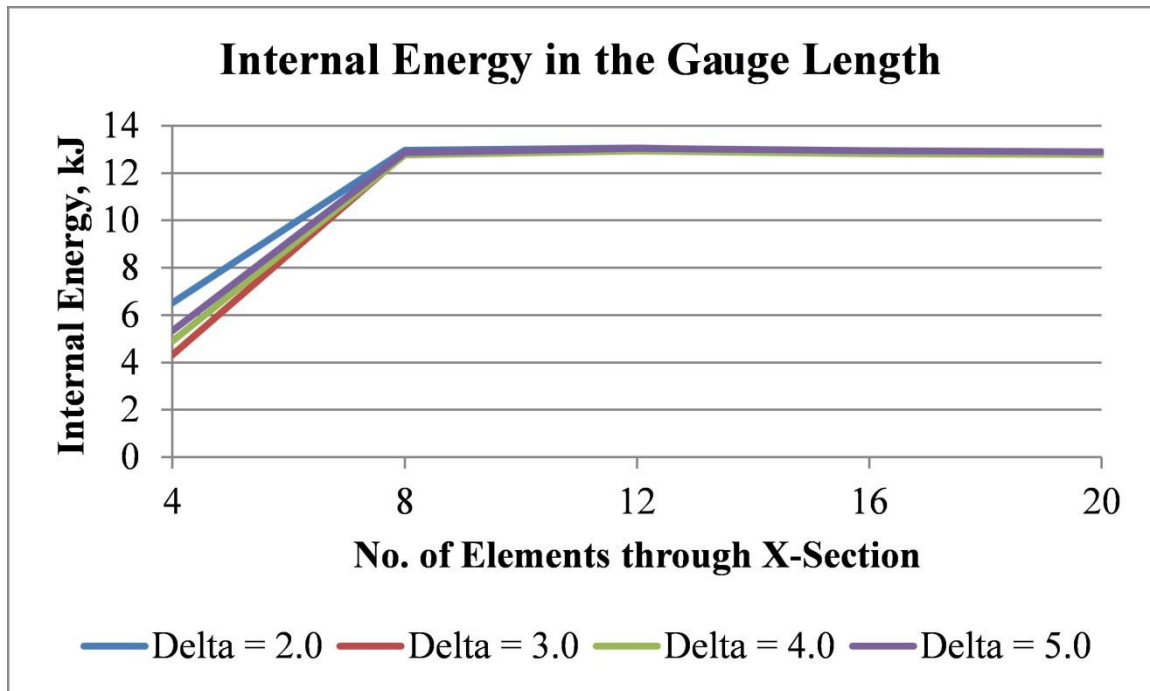


Figure 70. Internal Energy for Various Delta Magnifiers

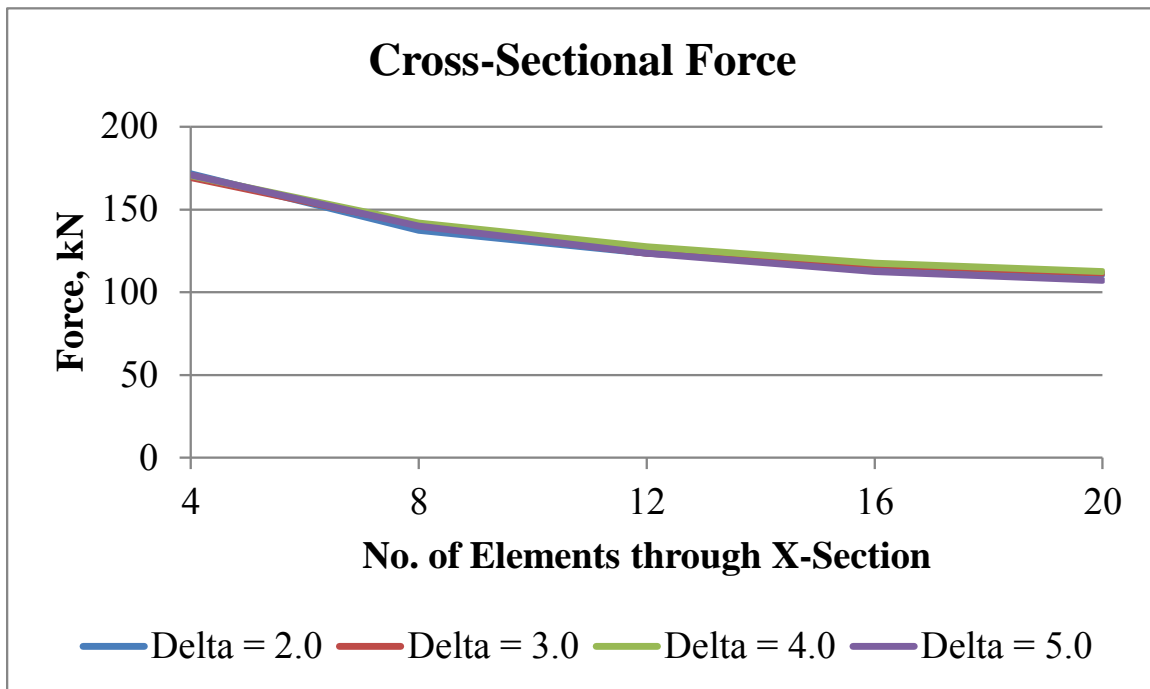


Figure 71. Cross-Sectional Force for Various Delta Magnifiers

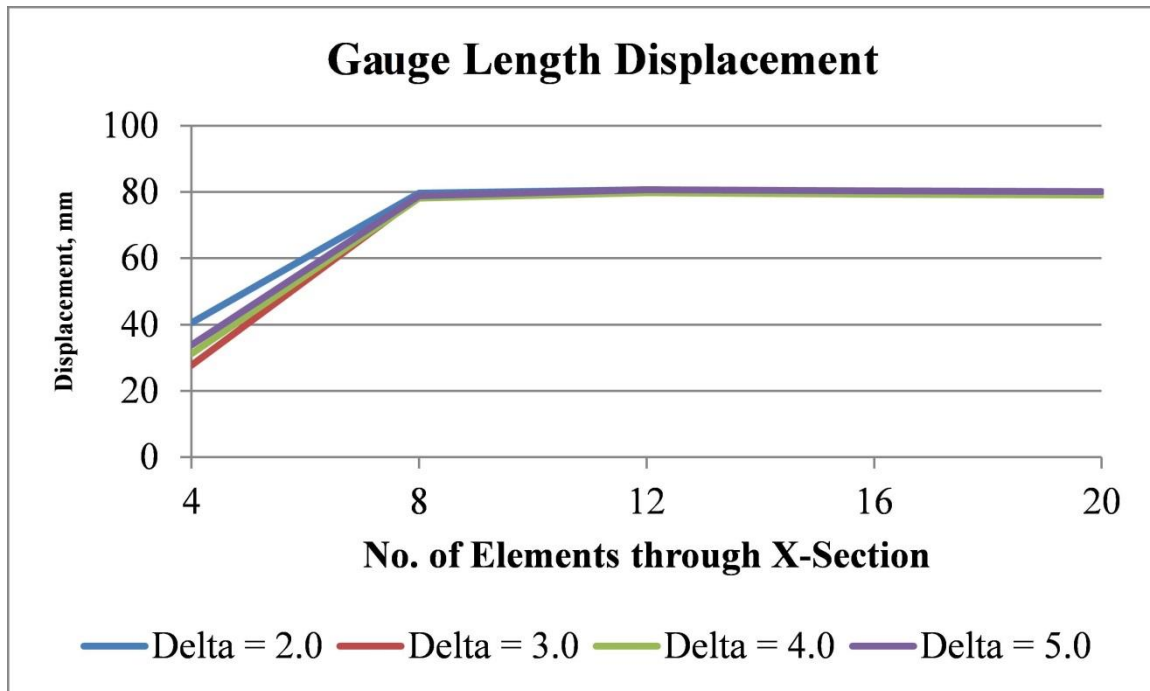


Figure 72. Gauge Length Displacement for Various Delta Magnifiers

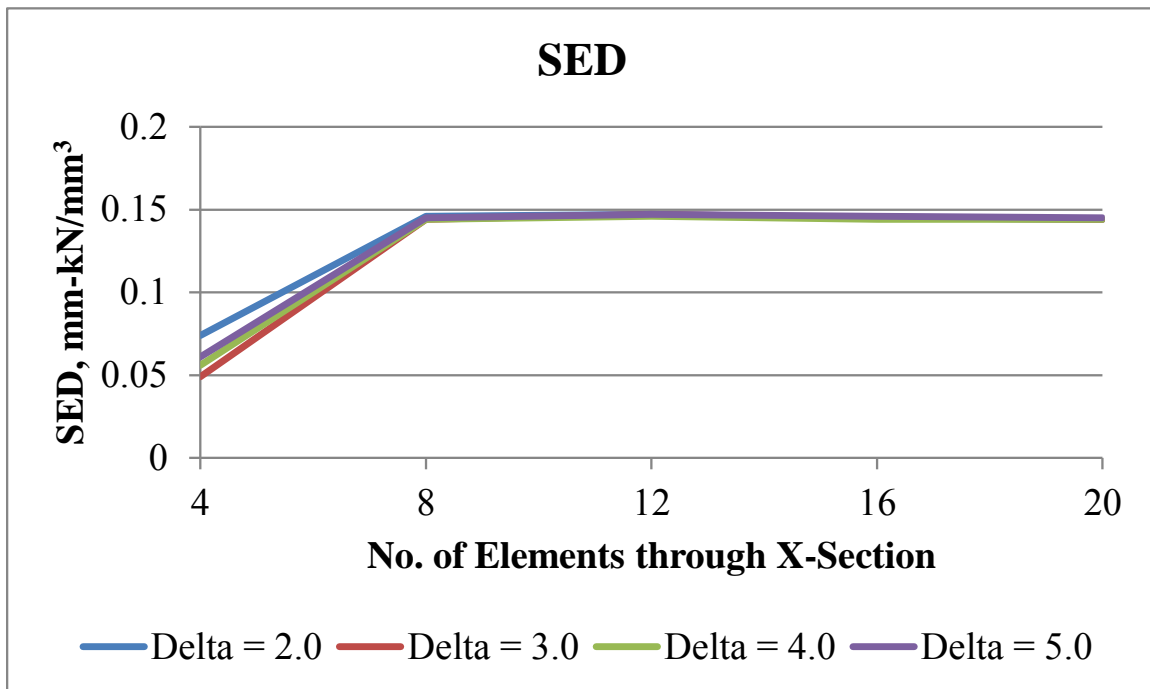


Figure 73. SED for Various Delta Magnifiers

With the exception of cross-sectional force, the results converged to a solution very quickly, requiring only 8 elements through the cross section. This was an improvement over the

convergence rates of the four existing techniques investigated in chapter 4. For a comparison, the results for internal energy, cross-sectional force, gauge length displacement, and SED for a delta magnifier of 3.0 were plotted with the results of the original four techniques in Figures 74 through 77.

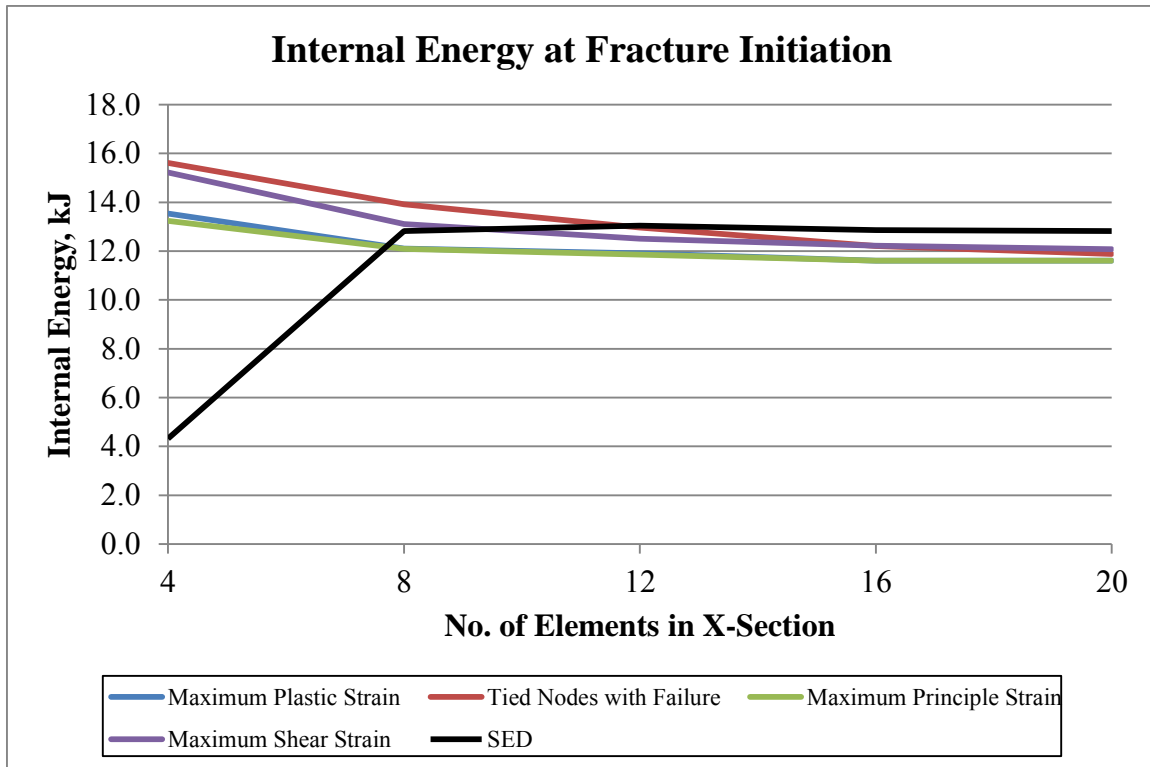


Figure 74. Convergence Comparison for Internal Energy

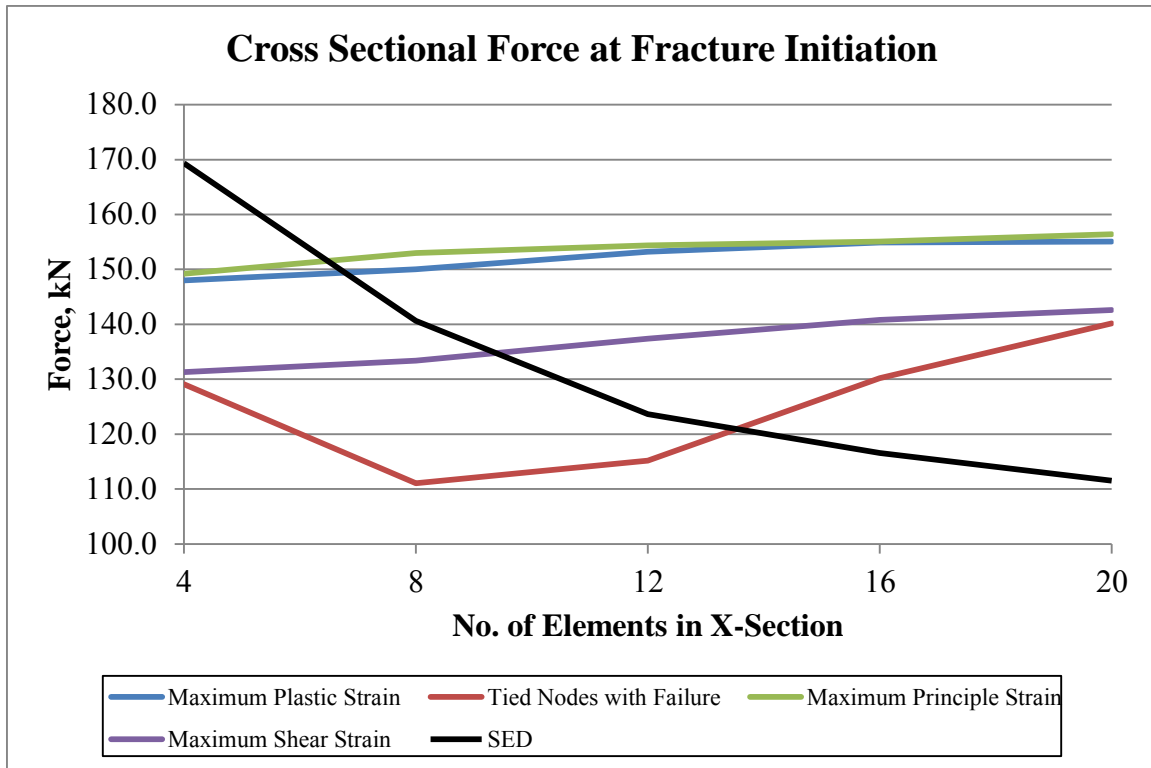


Figure 75. Convergence Comparison for Cross-Sectional Force

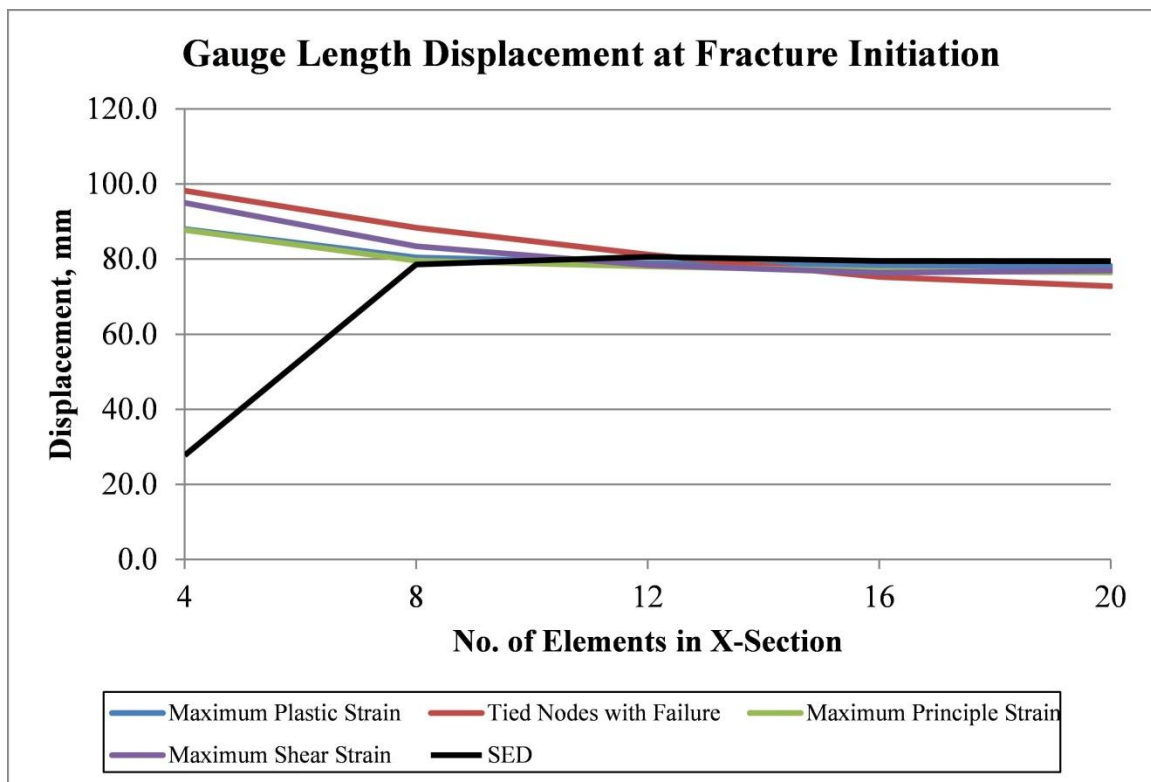


Figure 76. Convergence Comparison for Gauge Length Displacement

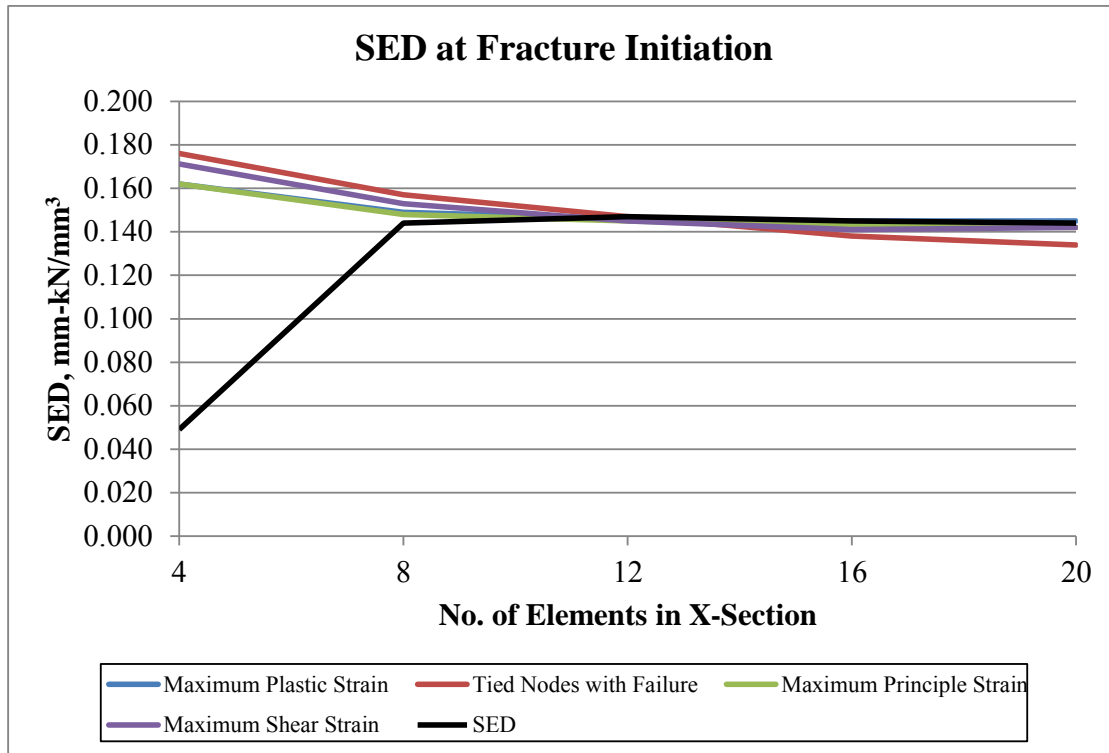


Figure 77. Convergence Comparison for SED

The convergence study for the prior four techniques revealed that for each parameter, the models did not converge entirely on a solution. A simple comparison of the relative difference in solution for meshes 2 and 5 were used to demonstrate the SED technique's effectiveness as a fast-converging method with less dependency on mesh density. Percent differences of the internal energy, cross-sectional force, gauge length displacement, and SED for the two mesh densities are shown in Table 11 for the four prior techniques and the new non-local SED technique.

Table 11. Percent Differences between Mesh 2 and Mesh 5 for Each Technique

Percent Difference of Mesh 2 Relative to Mesh 5				
Technique	Internal Energy	Force	Displacement	SED
Max Plastic Strain	4.17%	3.29%	2.94%	2.76%
Max Principle Strain	4.15%	2.17%	4.05%	4.23%
Max Shear Strain	8.57%	6.45%	8.31%	7.75%
Tied Nodes with Failure	17.23%	20.76%	21.43%	17.16%
Strain Energy Density	0.05%	26.11%	0.99%	0.00%



The strain energy density technique demonstrated the closest Mesh 2 solutions, relative to Mesh 5, for internal energy, gauge length displacement, and SED, as highlighted in yellow. For cross-sectional force, the Mesh 2 solution was not close to the Mesh 5 solution, but rather, the maximum principle strain technique demonstrated the closest solution.

Cross-sectional force was difficult to accurately capture in the model, regardless of the technique employed. The steel coupon underwent a phenomenon known as necking, where a highly-localized extreme cross-sectional area reduction occurred. A more interesting measurement would have been the peak force in the sample, which occurred immediately prior to the beginning of necking. However, this term was optimized in the material model and was identical for each technique. Therefore, a comparison of the peak force would not have aided in comparing the techniques. Due to the volatile behavior of the force in the cross section just prior to fracture initiation, and due to the seeming lack of convergence for this parameter, further investigation may be warranted.

#### **7.4 Additional Material Failure Criterion**

For AASHTO M180 steel, a typical stress-strain curve from literature [60] was used to determine the SED at fracture initiation in the steel coupon, which was 15.8 in.-kip/in.<sup>3</sup> (108.7 mm-N/mm<sup>3</sup>). For A1011-12B Gr. 50 steel, the stress-strain curve used to model this material was estimated by scaling the quasi-static steel data from the A572 Gr. 50 steel material. Scaling was done according to the yield stress. The SED at fracture initiation was 18.5 in.-kip/in.<sup>3</sup> (127.8 mm-N/mm<sup>3</sup>). Finally, using a length scale of  $3\Delta x$  with the third-coarsest mesh and Equation 7.8, the force-deflection curves using the non-local SED technique were plotted for each material with the physical test results for coupons without stress concentrations. The same formulation derived from the A572 Gr 50 steel material was used for the alternative materials, except the global SED was

substituted according to the material's property. The results are presented in the following sections, comparing the modeled results with physical testing.

## **7.5 Comparison to Physical Testing**

In this section, comparisons to coupons without any defects are made. This included test nos. DFS-L3-2, DFS-L4, DFS-L5, DFS-T1, DFS-T2, and DFS-T3. Categories for comparison were defined based on material type. Therefore, the three categories for comparison were A572, M180, and A1011. In each category, the force-deflection curves of the physical tests and of the corresponding simulations are presented and discussed. Also, the gauge length displacements for the models were shortened to represent the gauge lengths in the physical tests. This was done by tracking the longitudinal displacement of two nodes, and the selection of the nodes was done by ensuring that the necked region was included and that the initial separation distance was 9.75 in. (247.7 mm).

### **7.5.1 A572**

Test nos. DFS-L3-2, DFS-T1, DFS-T2, and DFS-T3 utilized A572 Gr 50 steel. The corresponding force-deflection curves are shown in Figure 78. For post-processing, a delta magnifier of 3.0 was used with Mesh 3 to determine the length scale. The width of the coupon was 1.675 in. (42.55 mm), resulting in a nodal spacing of 0.135 in. (3.43 mm) and a radius of 0.405 in. (10.3 mm). This length scale provided a scale factor of 98.16 to apply to the global SED at fracture initiation, according to Equation 7.8.

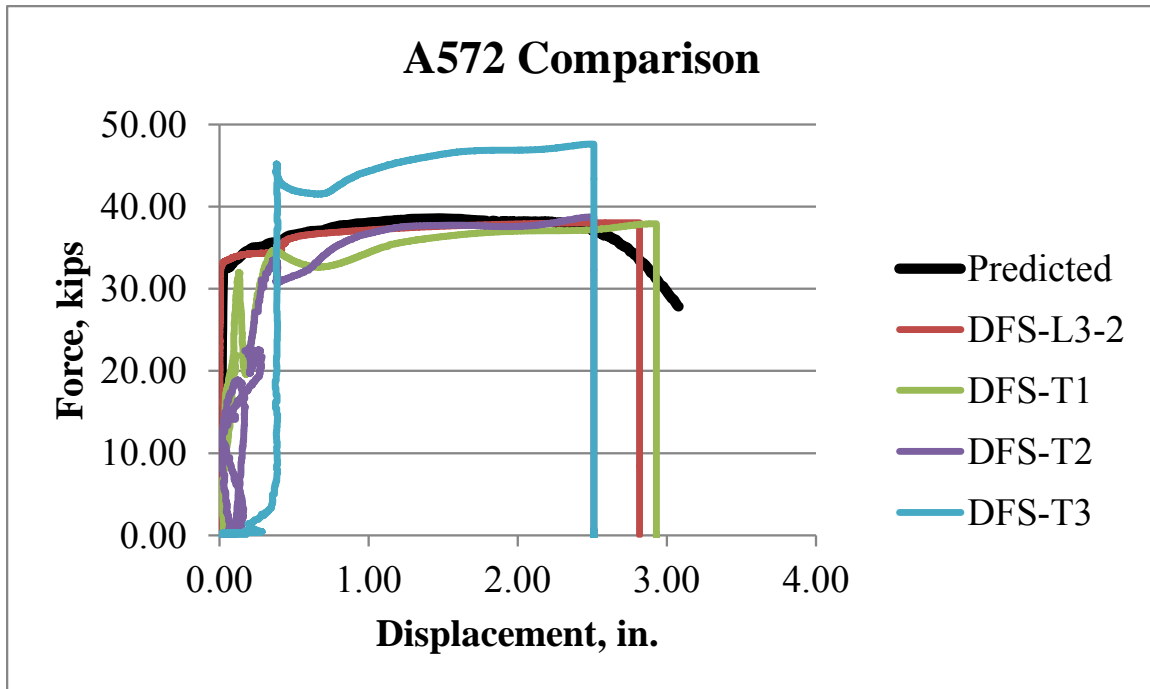


Figure 78. Force-Deflection Comparisons for A572 Gr 50 Steel without a Hole

### 7.5.2 M180

Test no. DFS-L4 utilized AASHTO M180 steel. The corresponding force-deflection curves are shown in Figure 79. For post-processing, a delta magnifier of 3.0 was used with Mesh 3 to determine the length scale, but this coupon was cut with a width of 2¼ in. (57.2 mm), resulting in a nodal spacing of 0.1875 in. (4.76 mm) and a radius of 0.5625 in. (14.3 mm). This length scale provided a scale factor of 70.4 to apply to the global SED at fracture initiation, according to Equation 7.8.

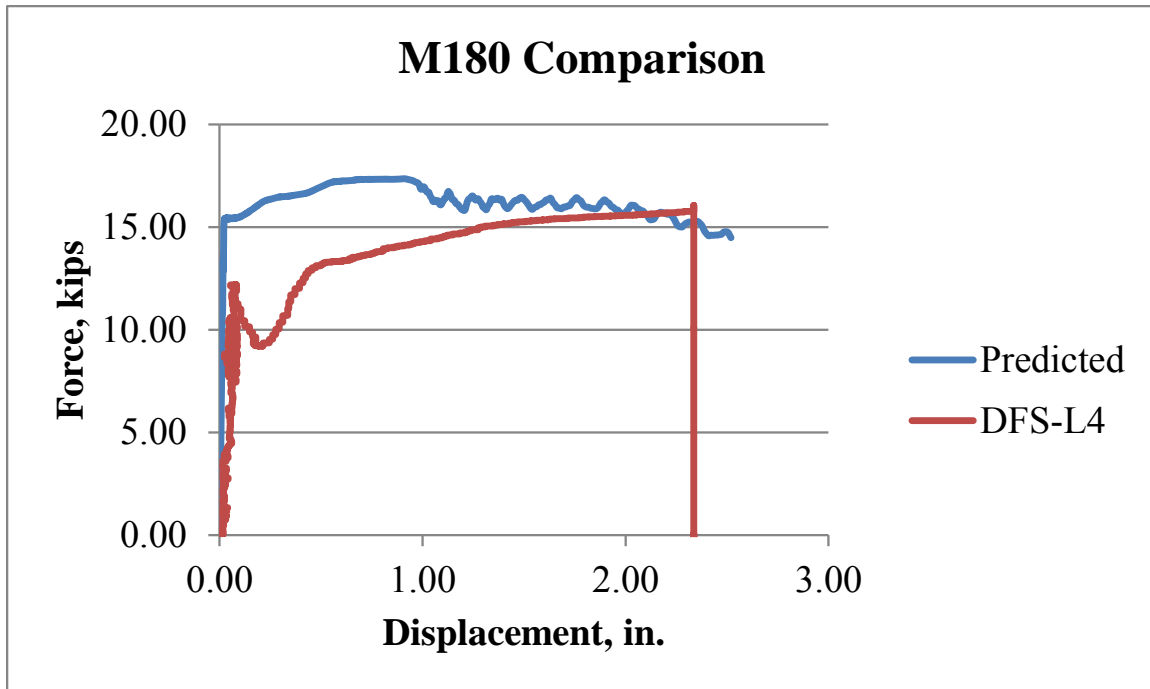


Figure 79. Force-Deflection Comparisons for M180 Steel without a Hole

### 7.5.3 A1011

Test no. DFS-L5 utilized A1011-12B Gr 50 steel. The corresponding force-deflection curves are shown in Figure 80. For post-processing, a delta magnifier of 3.0 was used with Mesh 3 to determine the length scale. The discretization was the same as for the A572 model, so the nodal spacing was 0.135 in. (3.43 mm), and the radius was 0.405 in. (10.3 mm). This length scale provided a scale factor of 98.16 to apply to the global SED at fracture initiation, according to Equation 7.8.

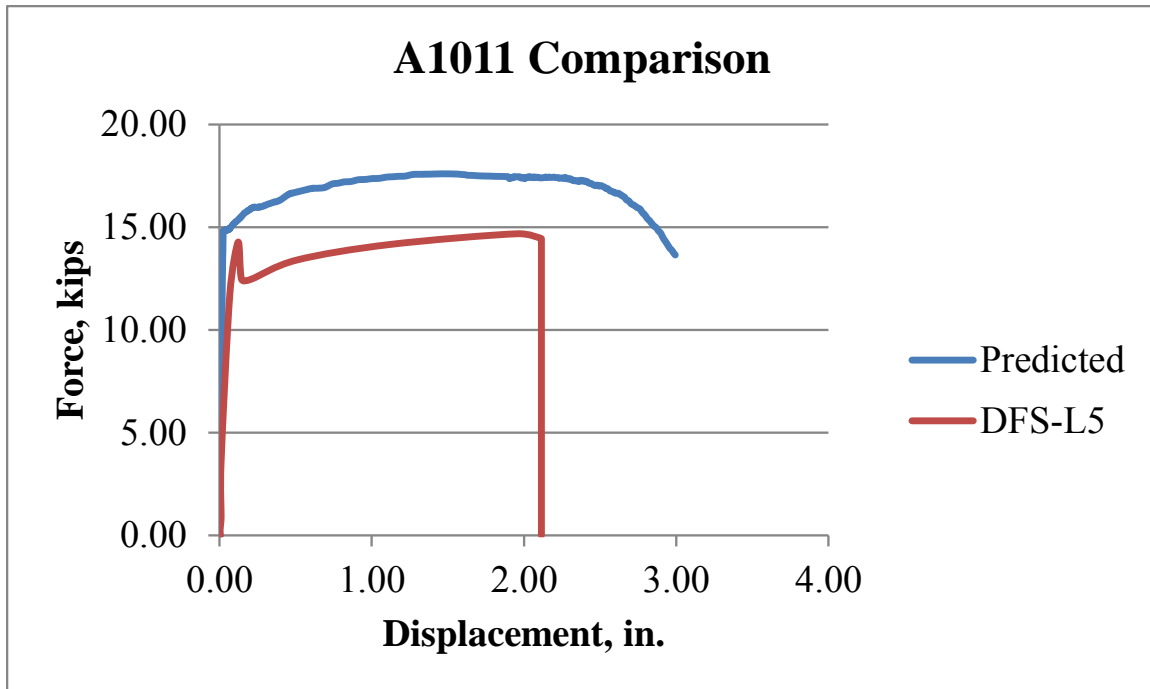


Figure 80. Force-Deflection Comparison for A1011-12B Gr 50 Steel without a Hole

## 7.6 Discussion

Five mesh densities were studied with the non-local SED technique, similar to the analysis conducted for the four common techniques described in chapter 4. The coarsest mesh utilized only four elements through the width of the critical section of the coupon. This coarse discretization demonstrated severe inaccuracies for all measurable parameters. However, for eight or more elements through the width, the measurable parameters were nearly identical, demonstrating very fast convergence and an improved degree of mesh insensitivity. From this sensitivity analysis, it is especially important to note that there is a minimum number of elements required through the width of the coupon in order for the non-local SED technique to be valid. This implies that there is a minimum number of nodes that need to be included in the non-local length scale in order for the technique to be valid. This is self-evident, considering that as the number of nodes within the length scale approaches 1 (the central node alone), the technique approaches a local discretization,

conceptually. However, in this case, with only one node, there is no meaning to the method since the FEM requires at least two nodes to define a beam element and three to define a shell element.

When stress-strain data was available to calibrate the failure parameter for the non-local SED technique, a close correlation existed in the force-deflection behavior, as demonstrated for A572 Gr 50 steel in Figure 78. The non-local SED technique predicted a deflection of 3.08 in. (78.2 mm) through the gauge length. The average displacement of the four tests was 2.69 in. (68.3 mm), with a maximum of 2.93 in. (74.4 mm). The physical force-deflection data showed very limited amounts of necking, and had this phenomenon been included, the displacements may have increased. Nevertheless, the non-local SED provided a close approximation for the initiation of fracture in the A572 Gr. 50 steel coupons.

Results for AASHTO M180 steel were not as precise. However, there was a large range of possible strength parameters. A stress-strain curve presented in literature was selected and applied to the material at hand. However, the actual stress-strain relationship may have differed enough to bring the simulation results closer to the physical results. In addition, only one coupon was tested in this category, and material properties can be highly variable. Despite these contingencies, the model predicted a displacement of 2.52 in. (64.0 mm), and the physical results showed displacements of 2.34 in. (59.4 mm). Therefore, if provided with precise stress-strain data, the non-local SED technique may perform satisfactorily for this alloy.

Results for the A1011-12B Gr 50 steel did not demonstrate close correlation. However, the stress-strain curve for this material was unavailable. Instead, an estimated stress-strain curve was used by scaling the same curve from the A572 Gr 50 model according to yield stresses. Also, during testing, there arose a complication with the data-capturing technology, such that the digital data was lost. Only a screen shot of the voltage versus time curve from the load transducers was available. Therefore, no conclusive statement could be made with regard to the effectiveness of

the non-local SED technique for this alloy. However, one major difference between this alloy and the A572 Gr. 50 steel was the thickness of the coupon. An issue for further investigation is that the thickness may play a critical role in the non-local SED technique; specifically, a 2D simplification of the technique may not be suitable for thick materials. Exactly what defines a suitable thickness was outside the scope of this project.

## 8 ADDITION OF A STRESS CONCENTRATION

### 8.1 Stress Concentration Factor

Defects in a material can introduce stress concentrations, inducing failure, significantly sooner than if the defect was omitted. For example, when a perfectly circular hole is cut in the center of a large plate, stresses can be as high as three times the applied stress for uniaxial tension [72]. In general, the stress concentration factor is the ratio of observed stress to the stress that would be present without a stress concentration factor, as in Equation 8.1:

$$K_t = \frac{\sigma_{max}}{\sigma_{nom}} \quad (8.1)$$

Where  $K_t$  = stress concentration factor  
 $\sigma_{max}$  = maximum observed stress in the material  
 $\sigma_{nom}$  = nominal stress without a defect

The stress concentration factor for a large plate with an elliptical hole in the center and a uniaxial stress applied on one boundary was derived at great length by Inglis in 1913 [73]. Because the dimensions of the plate were much larger than the dimensions of the hole, Saint Venant's principle could be applied, such that the edges of the plate did not influence the stress field near the hole. Inglis's equation for the stress concentration factor for an ellipse is given in Equation 8.2:

$$K_t = 1 + 2 \frac{a}{b} \quad (8.2)$$

Where  $a$  = half the length of the major axis of an ellipse  
 $b$  = half the length of the minor axis of an ellipse



For a circle, the major and minor axes of an ellipse are equal; thus, the stress concentration factor is 3 for a perfect circle whose diameter is sufficiently small relative to the width and length of the plate.

## **8.2 Application to SED**

Without modifying the post-processing procedure described in chapter 7, the SED approach to predicting failure very closely matched the physical results of test nos. DFS-L1 and DFS-L2. The hole drilled in the middle of the coupon significantly reduced the strength of the material, such that for a given applied far-field stress, the stresses acting around the circle were greatly amplified. The cross-sectional area was reduced relative to the hole-free coupons, so the cross-sectional force was divided by a smaller area, and the stresses to yield and failure were similar. However, the extreme concentration of stresses induced failure at engineering strains that were significantly smaller than the hole-free tests. In other words, strains around the hole became highly localized, similar to the phenomenon of necking observed in the hole-free coupons, and because of the stress concentration, this localization of strain occurred much earlier, relative to the hole-free coupons.

However, the non-local SED technique was not dependent on stresses alone, but on the combined effect of stress and strain. Therefore, it was hypothesized that no alteration was needed, even in the presence of a stress concentration. Similarly, it was hypothesized that the length scale, as a function of the nodal spacing and delta magnifier, was also independent of the stress concentration.

## **8.3 Post-Processing Parameters**

Input requirements included the number of nodes in the model, time steps to analyze, nodal spacing, delta magnifier, Young's Modulus, critical global SED, and the material yield stress. Each of these parameters is defined in Table 12.

Table 12. Post-Processing Parameters for Models with Holes

Parameter	A572	A1011	M180
No. of Nodes	2,676	2,676	2,172
No. of Steps	300	150	1,000
Nodal Spacing	3.43	3.43	3.81
Delta Magnifier	3.0	3.0	3.0
Young's Modulus (GPa)	200	200	200
Global Critical SED (kN-mm/mm <sup>3</sup> )	0.145	0.1278	0.1087
Yield Stress (GPa)	0.439	0.468634	0.449

## 8.4 Comparison to Physical Tests

In this section, comparisons are made with physical coupons that contained a defect in the center. This comparison effort included test nos. DFS-L1, DFS-L2, DFS-L6, and DFS-L7. As before, comparisons were made according to material type and included A572, M180, and A1011.

### 8.4.1 A572

Forces and displacements were greatly reduced when a hole was drilled into the center of the coupon. Displacements were an order of magnitude less. The non-local SED failure criterion predicted large reductions in both parameters as well, but the physical results were not consistent. However, deflections were reliably measured and the simulated results were plausible compared to the physical results. The average displacement from the tests was 0.299 in. (7.6 mm), and the simulated displacement was 0.331 in. (8.4 mm), a difference of 9.7 percent. The comparison of force-deflection curves is given in Figure 81.

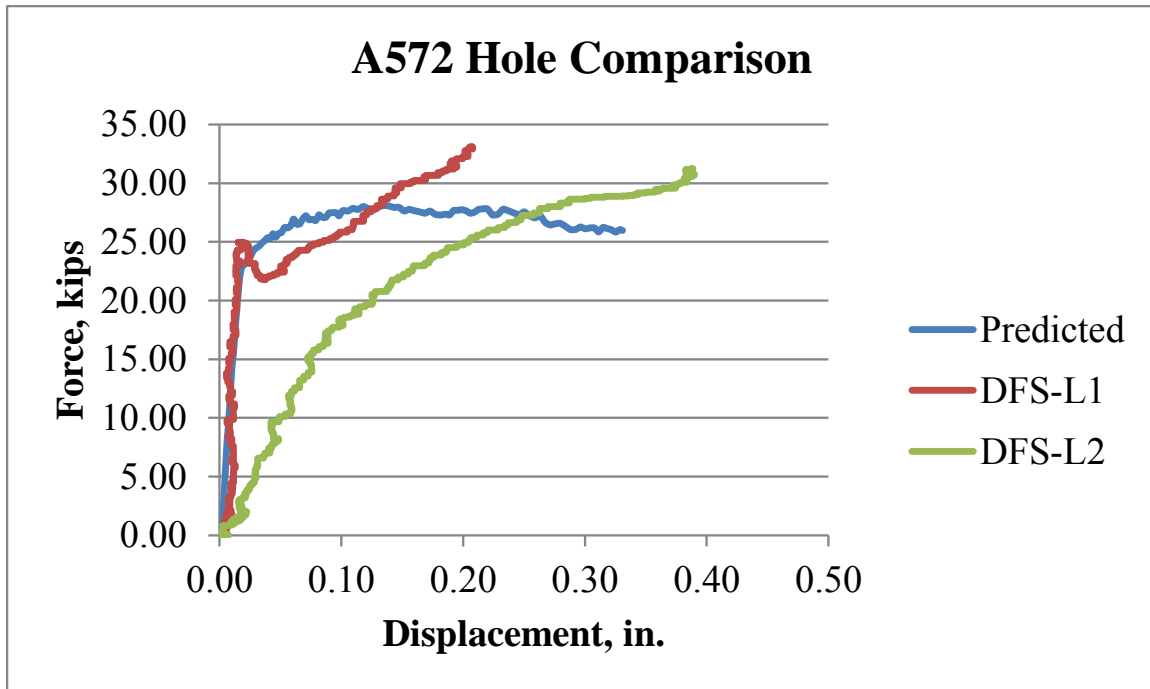


Figure 81. Force-Deflection Comparison for A572 Gr 50 with a Hole

#### 8.4.2 M180

Material modeling concerns for this material were documented in chapter 7. Notably, the stresses were significantly larger in the model than in the physical test results. This translates directly to forces as well. The modeled displacement was 0.495 in. (12.6 mm). The single test conducted in this report produced a displacement of 0.702 in. (17.8 mm), a difference of 29.5 percent. The force-deflection comparisons are given in Figure 82.

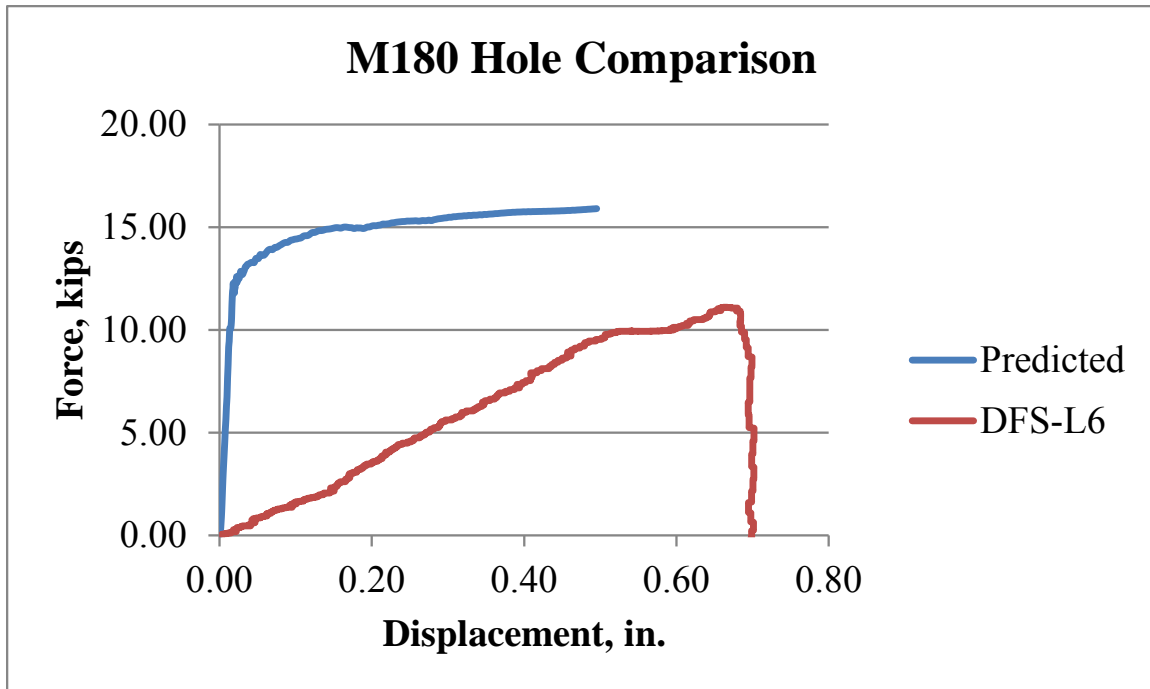


Figure 82. Force-Deflection Comparison for M180 with a Hole

#### 8.4.3 A1011

Recall that the stress-strain curve was estimated by scaling the stresses according to the yield stresses of A572 Gr 50 steel and A1011-12B Gr 50 steel. They should have similar yield stresses. However, the force-deflection curves in Figure 83 show an upward shift in strength and an exaggerated displacement in the gauge length for the simulated results, similar to the hole-free coupon. This sample had a reduced through-thickness, and it was assumed that the non-local SED technique could perform adequately without modification. However, these results indicate otherwise.

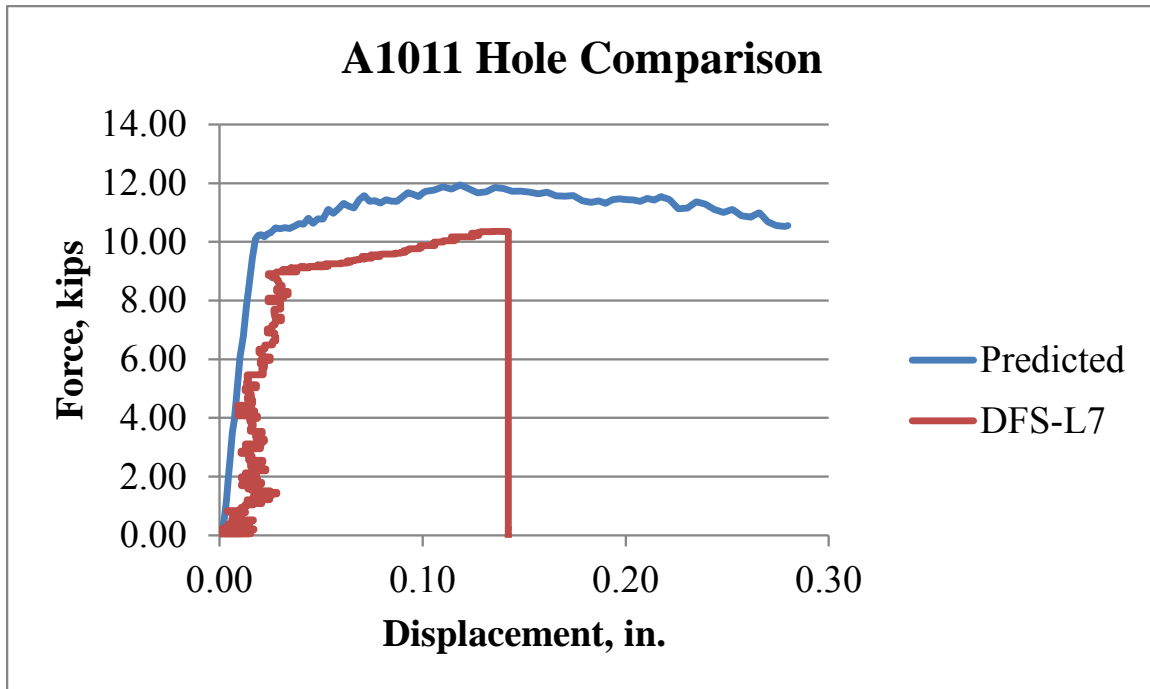


Figure 83. Force-Deflection Comparison for A1011-12B Gr 50 with a Hole

## 8.5 Discussion

The results of the A572 Gr. 50 steel simulation and physical tests demonstrated plausibility in the technique. In fact, the forces were very close to each other and deflections at fracture initiation were within 10 percent, comparing the simulation to the average of the physical tests. This was the only material that was calibrated with actual test data, and as such represents the best-case scenario for comparative analyses.

However, data collection or analysis for the AASHTO M180 sample did not appear to be accurate, given the unusual response of the steel. Therefore, no conclusive statement can be made about the non-local SED technique with regards to this alloy.

Finally, the results of the A1011 12-B Gr. 50 steel showed that the approximated stress-strain relationship used in the model was not indicative of the actual samples, and as such, forces carried by the coupon in the model were higher than what was observed. Additionally, the predicted displacement through the gauge length was nearly twice as large as the displacement

observed in the physical test. This coupon's most significant difference from previous coupons (notably the A572 Gr. 50 coupons) was its thickness, which was less than half that of the A572 coupons. Therefore, considering that no correction was made for thickness, the only conclusion that can be derived from this material is that thickness plays a critical role in the non-local SED technique.

## 9 EXAMPLE APPLICATION – W-BEAM GUARDRAIL

### 9.1 Background Research

Quasi-static tensile testing has been conducted on standard W-beam guardrail splices using a large uniaxial tension device [74]. In this series of testing, Ray reported a maximum tensile force of 98.5 kips (438 kN). However, maximum tensile forces in full-scale crash testing from previous testing done at the Texas Transportation Institute (TTI) [74] never exceeded 73.3 kips (326 kN). Also, in the quasi-static tests, failure occurred as bolts were pulled out of the holes and some longitudinal tearing occurred. There was no lateral rupture, like that observed in full-scale crash tests. Therefore, it was concluded that rail rupture was not likely related to the axial capacity of the rail. A photograph of the quasi-static tensile test results alongside the results of TTI's study are shown in Figure 84 [75].



Figure 84. Rail Splice Failures: Quasi Static Tensile Test Results (Left) and TTI Full-Scale Testing Results (Right) [74,75]

Rail splice rupture was observed in a full-scale crash test where the guardrail system was installed over a curb [76]. The test was conducted using a 4,363-lb (1,979-kg) pickup truck, an impact angle of 24.5 degrees, and a speed of 64.1 mph (103.2 km/h). The rail ruptured at a splice,

allowing the vehicle to pass behind the test article and, ultimately, causing the test to fail. A photo of the rail rupture is shown in Figure 85.



Figure 85. Ruptured Rail Installed Over a Curb [76]

In an effort to improve the shape of a W-beam guardrail section, a series of quasi-static tensile tests were conducted at the Midwest Roadside Safety Facility in the late 1990s [77]. Unlike the results reported by Ray et al, the failure mechanism in these tests was similar to that shown in Figure 85. In fact, tensile loads ranged from 113.6 to 126.3 kips (505.3 to 561.8 kN). Rail rupture resulting from these loads can be seen in Figure 86.





Figure 86. Rail Rupture from Quasi-Static Tension Testing at MwRSF [77]

Finally, an ongoing research effort involving a W-beam guardrail system was crash-tested near the upstream end of the system. The 2270P vehicle induced enough load in the rail to cause rupture away from any splice or rail slot location. Since there was no stress concentration in the geometry of the rail, the only explanation for the rupture was that the impact vehicle created a stress concentration in the rail by penetrating it with a sharp, rigid point. Had this event been avoided, rail rupture may have still occurred, but it would have been at a splice location. The question is, assuming rail rupture was a certainty, how much longer the rail would have remained intact. A picture of the ruptured rail element is shown in Figure 87. Similar to the curb testing, this rail rupture allowed the vehicle to pass behind the rail element, subsequently leading to the failure of the test article.



Figure 87. Rail Rupture from 2270P Impact

## 9.2 Modeling with SED Failure Criterion

The potential for using the SED failure criterion was demonstrated with a model of a 12.5-ft (3.8-m) section of standard W-beam guardrail. Each end of the beam was constrained with a boundary condition, where one end was fixed against motion and the other end was prescribed a translational motion along the axis of the beam. A load curve was used to define the motion, where at 0.1 ms, the velocity was 22.4 mph (10 mm/ms), and this velocity was maintained throughout the simulation. The model included 68,742 shell elements and 66,755 nodes. The average nodal spacing was approximately 0.22 in. (5.5 mm).

A piecewise plastic material model was used to govern the relationship between stresses and strains in the model. The material card used eight data points to describe the constitutive relationship, identical to the material model used previously for AASHTO M180 steel. The typical ultimate strength reported by Schmidt, et al [60] was 80.8 ksi (557 MPa). With a cross-sectional

area of 1.52 in.<sup>2</sup> (979.6 mm<sup>2</sup>) through the rail at the location of the splice bolts, the expected maximum force in the guardrail was 122.7 kips (546 kN).

### **9.2.1 Splice Holes**

Nodal displacements were recorded around one set of splice holes in the rail. For robustness, the nodal displacements around the rail slots were also recorded, but the reduced cross-sectional area at the splice location would intuitively indicate that it was the point of rail rupture. The failure strain in the material model was set to 10.0, sufficiently larger than the plastic failure strain in the material. Then, once the LS-DYNA model was finished simulating, the nodal displacements were analyzed with a non-local delta magnifier of 3.0, resulting in a radius for the non-local length scale of 0.66 in. (16.8 mm).

Four models were created, each with a different material card, where the theoretical low strength, theoretical high strength, baseline strength, and existing strength from literature were modeled according to Schmidt, et al [60]. The true stress-strain curves implemented in LS-DYNA are shown in Figure 88.

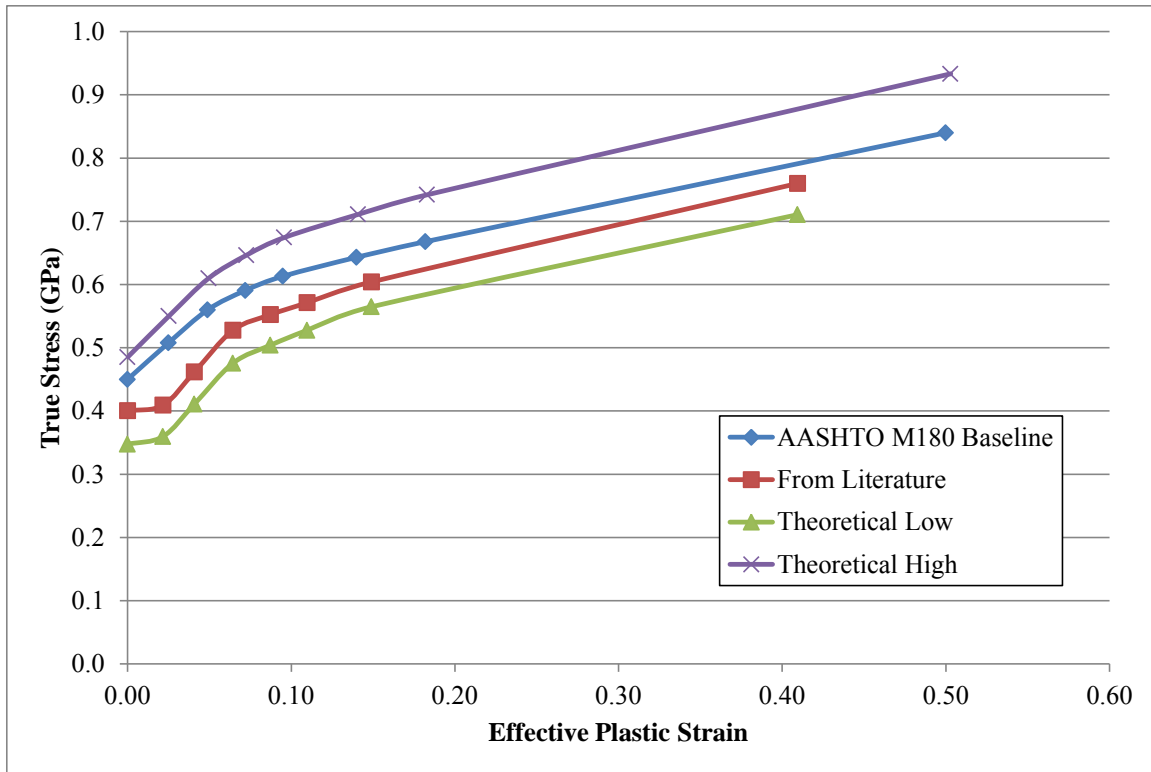


Figure 88. Stress-Strain Curves Implemented in LS-DYNA for W-Beam Models

For the baseline model, the SED failure criterion predicted crack initiation at node 71802 with a force of 136 kips (605 kN) and a deflection of 1.883 in. (47.8 mm) measured between the centers of the splices. The total energy at the time of failure was 219.8 kip-in. (24.8 kJ). The modeled rail and location of the fracture initiation are shown in Figure 89. The force-deflection curve and energy-deflection curves are shown in Figure 90.

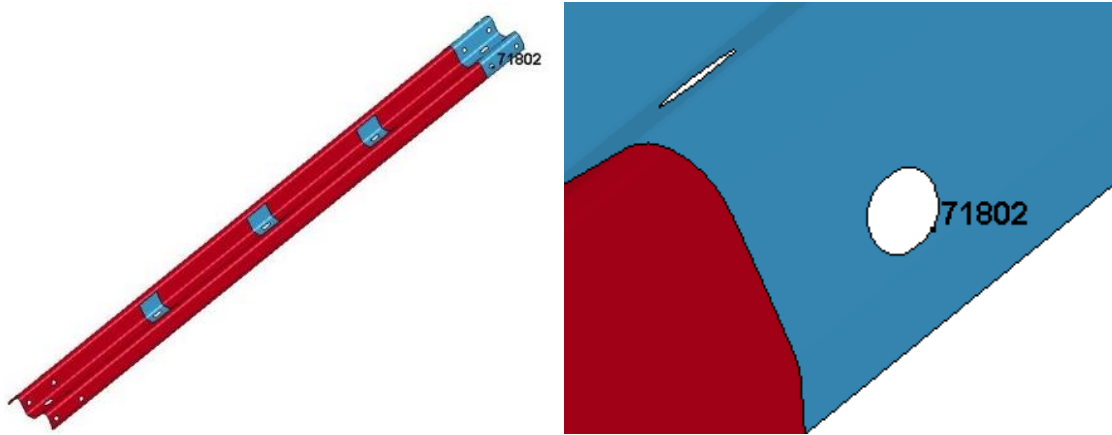


Figure 89. W-Beam Guardrail Model – Splice Failure

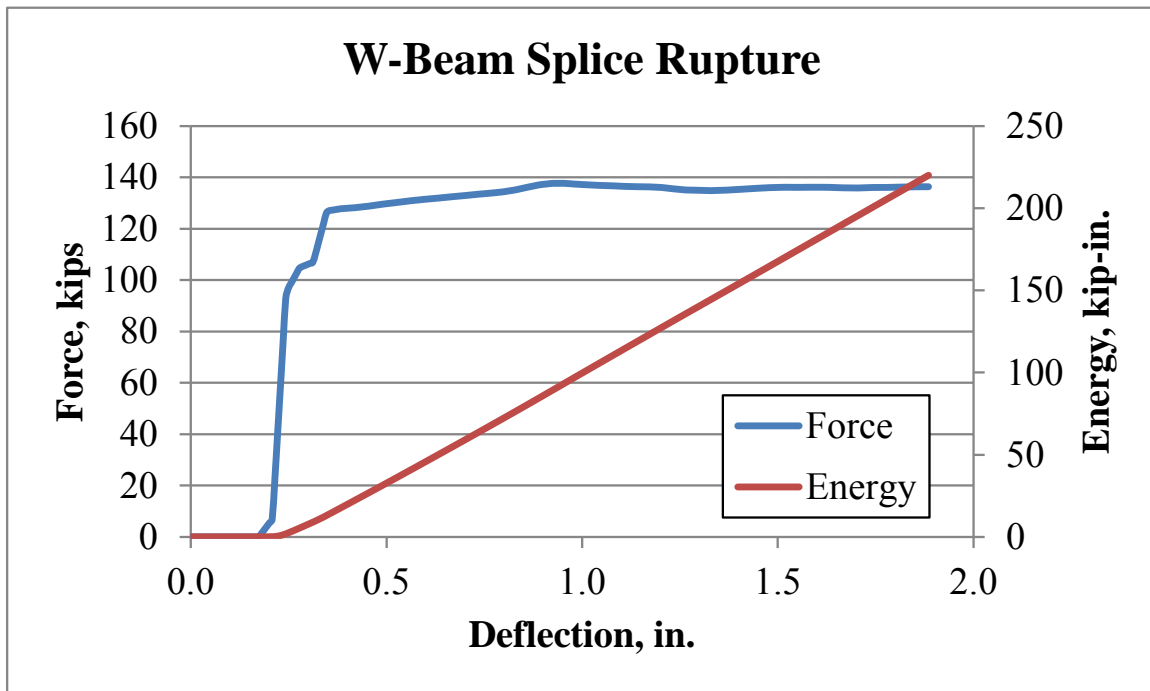


Figure 90. Force-Deflection and Energy-Deflection Curves for W-Beam Rail Splice

The 136-kip (605-kN) tensile force predicted by the model with the SED failure criterion was about 8% higher than the maximum force reported by MwRSF [77]. Therefore, a bracketed model, including theoretically low and high strengths, was created and analyzed. The critical, global SED for each model was scaled using the area under the curves in Figure 88. The baseline model was used for AASHTO M180 steel coupons, as documented in this report. The areas under

the curves for the theoretically low and high curves, as well as the curve taken from literature, were 10.1, 17.2, and 11.1 in.-kip/in.<sup>3</sup> (69.7, 118.8, and 76.8 mm-N/mm<sup>3</sup>), respectively. Upon doing so, the model with the critical, global SEDs predicted a theoretically low force of 103 kips (458 kN) and a theoretically high force of 147 kips (654 kN). The constitutive model taken from literature predicted a force of 117 kips (520 kN).

### **9.3 Discussion**

The force at which rail rupture will occur has been the subject of multiple investigations, and a clear answer has not been readily found. Quasi-static testing may not even induce the correct failure mechanism observed in full-scale crash testing. In other cases, quasi-static testing did reproduce the correct failure mechanism observed in full-scale crash testing, which is known to be lateral rupture starting at a bolt hole on the W-beam corrugation.

Full-scale crash tests where the rail was instrumented indicated rail tension forces less than 73.3 kips (326 kN). However, loads from these tests can be applied over very small areas, effectively puncturing the rail and creating additional stress concentrations and weaker cross-sections. Bending moments in the rail element may also contribute to exceptionally high stress in the material, effectively requiring less far-field applied stress on the rail to induce rupture at a stress concentration.

If dynamic effects are not considered, as they were neglected in the coupon modeling, then the results published by MwRSF in the late 1990s may be indicative of the forces in a W-beam rail in pure tension, owing to the failure mechanism observed in their tests. Forces ranged from 113.6 to 126.3 kips (505.3 to 561.8 kN). Both of these tested values fall within the theoretical low and high forces predicted by the model with the SED failure criterion, which ranged from 103 to 147 kips (458 to 654 kN).

## **9.4 Conclusion and Recommendations**

The SED failure criterion was shown to predict the initiation of fracture. This conclusion is based on a wide range between the theoretical low and high forces, which covered a wide range of tensile test data. However, to ensure confidence in the model, a standard-sized coupon should be cut out of the rail of interest and tested quasi-statically. Uncertainty in the constitutive relationship was shown in chapters 7 and 8 to significantly reduce accuracy in the models, as expected. Thus, a new model should be created with a FEM program, such as LS-DYNA, and the critical, non-local SED should be adjusted until the global SED in the modeled coupon matches the corresponding physical data. To make this calibration, a minimum of 8 elements should be used through the width of the material, with a delta magnifier of at least 2.0.

Crack propagation was not investigated in this research. Therefore, for a complete application to modeling W-beam fracture in full-scale crash testing, a more in-depth study needs to be completed to determine propagation tendencies and their relations to the non-local SED.

## 10 CONCLUSIONS AND RECOMMENDATIONS

### 10.1 Summary

Mesh sensitivity in crack prediction has inherently limited the applicability of traditional failure criteria in the FEM. However, in recent years, the implementation of non-local modeling platforms has generated precise models of crack onset and propagation. However, in general, these platforms are computationally demanding and not currently suited to large-scale models, such as a 175-ft (53.3-m) W-beam guardrail system. Therefore, a non-local technique was implemented in a commercial FEM code, LS-DYNA, wherein the strain energy density was estimated at each node in the model and compared to a critical strain energy density unique to that material.

The critical SED for the material was determined from quasi-static tensile testing obtained in literature. The model itself was simulated using shell elements and a plastic material model where the failure parameter was set significantly high. The nodal displacements were recorded in an output file every 0.01 ms and were used in a post-processing code developed by the author. This code is described in chapter 7, and the source code is given in Appendix C. A length scale was described as a function of the nodal spacing in the model, and each node within that length scale was used to determine the SED at the central node. The relationship between each pair of nodes was assumed to be similar to an elastic, perfectly plastic spring. The SED calculated between each pair of nodes was summed up over the region with a radius equal to the length scale. When this summation equaled or exceeded the critical SED for the material, the node was said to be the site of fracture initiation if it were the first to meet the failure criterion.

The SED failure criterion was determined for A572 Gr. 50 plate steel, A1011-12B Gr 50 plate steel, and standard W-beam guardrail steel (meeting AASHTO M180 specifications). Then dynamic component tests were conducted using bogie test vehicles to apply tensile load. Deformations were captured with high-speed video and used to determine strain as a function of



time. Load cells were used to capture the force in the coupon, also as a function of time. Then, the two were cross-plotted to obtain force-displacement data, which was converted into engineering stress-strain curves. The area under the stress-strain curves was identical, by definition, to the strain energy density and was used to validate the model for the two material types.

Additionally, a stress concentration and a reduced cross-sectional thickness were modeled and tested for each material. Nothing but the geometry of the part was changed in the model, including the calculation of the non-local SED failure criterion.

Mesh sensitivity was investigated in common failure criteria used in LS-DYNA. Then the same investigation was applied to the non-local SED failure criterion. This was done for a coupon with and without a hole.

Next, the SED failure criterion was applied to a full-length, standard section of W-beam guardrail. Nodal displacements around splice bolt holes were recorded and post-processed using the critical, global SED failure criterion for AASHTO M180 steel.

## **10.2 Conclusions**

High-strength steel does not exhibit significant strain rate effects, as shown by test nos. DFS-L3 and DFS-L3-2. Therefore, strain rate effects were not considered relevant in the current formulation of the SED failure criterion. However, this inclusion could be made with further investigation for other material types, such as polymers or viscoplastic materials.

In addition, the grain orientation caused by the direction of rolling in the manufacturing process did not influence the material's behavior. Therefore, the steel could be considered isotropic, so long as it was standard structural plate steel. This may not be the case for structural shapes requiring multiple rolls and other deformations, which may enhance the effect of grain orientation.

Within the realm of virtual reality, several failure criteria were studied to obtain the SED at fracture in several different mesh densities. It was demonstrated that these failure techniques induce mesh dependence and, at best, have limited convergence for the densest mesh. In contrast, the SED failure criterion demonstrated a rapid convergence with coarse even meshes. As a result, this procedure may potentially be implemented, without undue expense, to predict the onset of fracture in a material.

In addition to reduced mesh sensitivity, the SED failure criterion was able to predict the onset of fracture in a material with a stress concentration without recalibrating the failure parameter, specifically for A572 Gr. 50 steel, for which more data was available for the material model.

The reduced strength and ductility predicted by the SED failure criterion with a stress concentration can potentially be associated with a stress concentration factor. However, the early onset of localized straining around the holes, known as necking, led to high non-local SED values at the nodes around the hole, and as such, no additional considerations were required to account for the stress concentration.

The non-local SED calculated at a node said to be in failure could be as much as 100 times larger than the global failure SED for the material. This was inherently a function of the length scale, where large length scales incorporated more slightly deformed areas, thus lowering the overall strain energy density. Effectively, the non-local SED is a composite average within the radius, and the more non-deformed portions that are included, the smaller the non-local SED at the node will be. For large length scales, the critical SED for a node would have to be increased, possibly due to the fact that more nodes are contributing to the summation used to calculate the SED. This relationship was not studied in depth and should be considered in future studies.

It was thought that a length scale needed to be determined for the coupon, either as a function of geometry or of mesh density. Formulations relying solely on geometric considerations could not be derived as part of this research effort, but they do represent a possible avenue for further investigation. When formulations were based on nodal spacing, the size of the radius fundamentally governed the calculation of the non-local SED. Therefore, an empirical relationship was developed to adjust the failure parameter for the SED based on the radius of the length scale. Upon doing so, results for internal energy, gauge length displacement, and global strain energy density were nearly identical for meshes with 8 elements and 20 elements through the critical section of the coupon.

When the same approach was applied to coupons with stress concentrations in the form of holes, the results were approximately as precise as without stress concentrations. This indicates the plausibility of using the non-local technique without adjusting it to account for the stress concentration. However, further testing is required to more fully evaluate the model.

Finally, when the SED failure criterion was applied to a standard-length section of W-beam guardrail, tensile forces at rupture theoretically ranged from 103 to 147 kips (458 to 654 kN). When the material model that was found in literature was used, the SED failure criterion predicted a tensile force at rupture of 117 kips (520 kN). Tensile testing reported in literature indicated a failure load between 113.6 to 126.3 kips (505.3 to 561.8 kN). Therefore, it was concluded that the non-local SED failure criterion, using the material model found in literature, was able to accurately predict the maximum load in the rail prior to rupture. However, with such large ranges for constitutive relationships, it is evident that specific tensile testing should be conducted based on coupons that have been cut from the same heat of steel used to make the W-beam rail. With this data, more conclusive evidence could be ascertained for comparison with the model.

### 10.3 Recommendations

The results contained herein are especially pertinent to A572 Gr. 50 steel, whose certified yield stress is near 63.7 ksi (439 MPa). The material tested in this report had a carbon content near the bottom of the range applicable to this grade of steel. If the yield and ultimate stresses of the material are close, then it is recommended that the effective plastic stress-strain curves used in LS-DYNA be scaled up or down, accordingly. However, if the differences are deemed significant, quasi-static tensile test data should be obtained for the material.

Likewise, if the A1011-12B steel or W-beam material properties are known and differ significantly from those used in this report, then accurate data should be obtained. As demonstrated by Schmidt et al. [60], this is a highly probable scenario.

When steel rupture is a legitimate concern, an analysis should be conducted to ensure this potentially catastrophic failure mechanism is avoided. Traditionally, this would call for over-designed elements, since a reliable and usable method for predicting fracture has not been readily available. The non-local SED failure criterion provides a solution to this enigma and should be employed whenever fracture is possible (intentionally or otherwise). An example was given wherein rail rupture was predicted to happen in a section of W-beam guardrail.

Mesh sensitivity comparisons for the non-local SED technique showed that 4 elements through the width of the critical section was an inadequate number to define a non-local length scale. At 8 elements through the critical section, the technique demonstrated remarkable insensitivity to mesh density as it pertains to the prediction of displacement, internal energy, and strain energy density of the steel at the point of fracture initiation.

Early attempts to produce user-defined material models for LS-DYNA were stalled when it was discovered that the architecture of the code disallowed for the possibility of storing the strain energy density of an element as a history variable. Had this not been the case, the user-defined

FORTTRAN code could have been altered to examine a certain number of elements defined by a length scale at one time, rather than a single element at a time. This would convert the local discretization into a non-local discretization. Then the SED of all the elements in the new length scale would contribute to the failure criterion of the central element. A modification to the user-defined material model code has been recommended to and received by the support staff at LSTC.

## **11 LIMITATIONS AND FUTURE WORK**

### **11.1 Limitations to the Current Work**

As few as one coupon was available to compare physical tests with the simulated results. Material variability alone can significantly alter the properties of any given sample. With more coupons available for testing, an aggregate average could be used for comparison to the model, and theoretical low and high strength values could be assessed. With this effort, an analyst would be able to determine if the material would be safe from rupture (theoretical low strength) or if the material would certainly rupture (theoretical high strength).

High-speed dynamic tensile tests were conducted on a common structural steel grade, but the observed yield and ultimate stresses matched the quasi-static test results reported in the mill certificate of conformity. As a result, strain rate effects were neglected. However, if the material of interest exhibits significant strain rate effects, an allowance in the calculation of the SED would be required.

Also, testing was conducted in temperatures well above the ductile-to-brittle transition temperature for steel. However, if the temperature is significantly different from room temperature (where quasi-static testing was done), and if that significant difference induces dissimilar material behavior, then quasi-static testing may need to be repeated at the desired temperature. This holds true for all materials, where if a material is subjected to extreme cold, but normally tested at room temperature, the test procedure may need to be altered.

Grain orientation was altered in this study for A572 Gr. 50 plate steel. Coupons were cut either perpendicular or parallel to the roll direction. However, the material behaved the same for both directions, implying that grain orientation was insignificant for plate steel under dynamic loading. However, other steels are subjected to multiple rolls and deformations to produce a desired shape. For example, A500 Gr. C steel is commonly used in tubes. This material can have

a reduction of nearly 50% in toughness when the grain orientation is perpendicular to the direction of applied load. Therefore, if the material under consideration is highly susceptible to grain orientation, then quasi-static tensile testing needs to be conducted for the grain orientation of interest.

Only tensile loads were applied in the current implementation of the SED failure criterion. This produced primarily Mode I failure in the material. Similarly, the physical testing phase did not extend to other loading modes. As a result, before confidence can be assured in mixed-mode loading, more testing is required in various load configurations.

Thin shells were assumed for each model, despite the fact that the thickest coupons were  $\frac{5}{8}$  in. (7.9 mm). When the thickness was reduced for a different material with the same nominal yield stress, the results of the non-local SED did not adhere to physical test results. This indicates that the non-local SED loses accuracy much the same way that an assumption of plane stress loses accuracy if the material is too thick. Therefore, the current formulation of the non-local SED is limited to thin materials, where plane stress is an acceptable assumption.

## **11.2 Recommendations for Future Work**

The XFEM has demonstrated the potential for crack modeling, both initiation and propagation, for implicit applications. Specifically, the theory has been implemented in ABAQUS. However, the implementation of the theory in LS-DYNA has only recently been made. At the time of the current research effort, the XFEM shell section card in the LS-DYNA input deck required the use of a specific material model, which was only applicable to solid elements. The conflict of element type prevented an in-depth investigation of the theory. When the explicit version of the XFEM in LS-DYNA is made functional, it should be investigated as a potential solution to fracture problems in roadside safety engineering. For it to be beneficial, it should demonstrate a level of mesh independence similar to the non-local SED failure criterion outlined in this report.

In addition, peridynamics has been implemented in ABAQUS via truss elements, which were representative of the bonds described in the peridynamic theory. Truss elements can also be used in LS-DYNA to the same end. Trusses can be controlled with a user-defined material model, such that the constitutive relationship adheres to the peridynamic theory, which would include a provision for failure. The current limitation to this approach is in the contact performance of surfaces modeled with trusses. In roadside safety applications, this contact can be crucial given the level of entropy often experienced in such applications. Perhaps the truss elements can be embedded in null shell elements, where the latter would provide the contact definitions.

In the current research effort, the SED failure criterion was implemented with a post-processing, user-developed program. Nodal displacements were calculated in LS-DYNA and used to calculate the non-local SED at each node for each time step. However, failure in the model was defined by the first node to meet the SED failure criterion. As a result, results that followed were no longer valid and crack growth could not be studied. This finding was considered acceptable in the scope of the project, wherein fracture onset was desired.

Fracture prediction could become more robust if the SED failure criterion is implemented directly into LS-DYNA. One possible avenue to do so lies in the algorithm for constrained, tied nodes with failure. Currently, this option requires a failure strain to release nodes from one another. This failure flag could be modified to access a subroutine that takes for its input a non-local length scale, a material yield stress and Young's modulus, and a non-local SED at failure. Then it would output the result of the failure check to the tied nodes algorithm, wherein if the failure criterion is met, the nodes would be released from one another. Application of this procedure would require a non-local modification to the standard method of element calculations, which are inherently local.

Another possible avenue for implementing the SED approach in LS-DYNA may lie in the user-defined failure subroutine for some material models, such as \*MAT\_024. If the failure strain



is set to a negative number, the code looks to a subroutine in a FORTRAN source code that can control failure in several ways. Currently, only the incremental change in the SED is fed into the subroutine and there are no history variables available to the user. Therefore, the cumulative SED for the element cannot be determined and used as a failure criterion. Additionally, the material model is inherently local. This could be mitigated by using \*MAT\_NONLOCAL, where the user could specify a length scale similar to the one recommended in this study. Combining this additional material description with a two-dimensional history variable (say HSV[i,j]), the SED between the central node, i, and all other nodes within the length scale, j, could be stored. Then a second one-dimensional history variable could be used to track the summation of pairwise SEDs. This summation would be the non-local SED at the central node and would be compared to the critical non-local SED.

Also, the non-local SED technique has exhibited a dependence on thickness. Therefore, more consideration needs to be given to a 3-dimensional formulation of the technique. This can be simply accomplished by replacing shell elements in the local FEM model with solid elements. Then, instead of defining a length scale with x and y coordinates forming a circle, the length scale would be described by all three coordinates, forming a sphere. This would increase the number of nodes within the length scale a great deal and as a result, was not attempted in the current research effort. It was shown that there is a minimum number of nodes required within the non-local length scale for the 2-dimensional formulation. Therefore, it follows that there is also a minimum number of nodes in all three directions, indicating that there may be a minimum number of solid elements needed through the thickness of the part.

The derivation contained herein was for A572 Gr. 50 steel, and it was empirically determined. From the relationships of the empirical data, it appeared that the critical SED around a node had to be scaled up to account for the summation of several nodes within the length scale.

This scaling was accomplished using natural logarithmic and exponential operations. The coefficients and constants used in the scaling formula were only based on empirical data. Further efforts should be undertaken to more fully understand the physical meaning of these parameters.

Lastly, more physical tests need to be conducted to ensure that the material behavior is not an extreme example. Likewise, stress-strain data needs to be gathered and implemented to provide confidence in predictive capability, as opposed to estimating strengths according to a scaling process of yield stresses. If these additions to the test matrix still do not solve the disparities in the predicted-versus-tested results for coupons with stress concentrations, then the possibility of modifying the post-processor algorithm may need to be discussed.

## 12 REFERENCES

1. Reid, J.D., Rohde, J.R., and Sicking, D.L., "Box-Beam Burster Energy-Absorbing Single-Sided Crash Cushion," *Transportation Research Board*, TRR 1797, Paper No. 02-2531, Washington, D.C, 2002.
2. Griffith, A.A., "The Theory of Rupture," *Proceedings of the First International Congress for Applied Mechanics*, Edited by C.B. Biezeno and J.M. Burgers, Delft, 1924.
3. Anderson, T.L., *Fracture Mechanics: Fundamentals and Applications*, 3<sup>rd</sup> ed., CRC Press, Taylor & Francis Group, Boca Raton, FL, 2005.
4. Irwin, G.R., "Onset of Fast Crack Propagation in High Strength Steel and Aluminum Alloys," Naval Research Laboratory, Mechanics Division, NRL Report No. 4763, Washington, D.C., May 24, 1956.
5. Janssen, M., Zuidema, J., and Wanhill, R.J.H., *Fracture Mechanics*, 2<sup>nd</sup> ed., VSSD, The Netherlands, 2006.
6. Elices, M., Guinea, G.V., Gomez, J., and Planas, J., "The cohesive zone model: advantages, limitations, and challenges," *Engineering Fracture Mechanics*, Vol. 69, Issue 2, pp. 137-163, January 2002.
7. Irwin, G.R., "Analysis of Stresses and Strains Near the End of a Crack Traversing a Plate," *Journal of Applied Mechanics*, Vol. 24, pp. 361-364, 1957.
8. Rice, J.R., "A Path Independent Integral and the Approximate Analysis of Strain Concentration by Notches and Cracks," *Journal of Applied Mechanics*, Vol. 35, pp. 379-386, 1968.
9. Wells, A.A., "Unstable Crack Propagation in Metals: Cleavage and Fast Fracture," *Proceedings of the Crack Propagation Symposium*, Vol. 1, Paper 84, Cranfield, UK, 1961.
10. Gere, J.M., *Mechanics of Materials*, 6<sup>th</sup> ed., Brooks/Cole, a division of Thomson Learning, Inc., Belmont, CA, 2004.
11. Sih, G.C., "Some basic problems in fracture mechanics and new concepts," *Engineering Fracture Mechanics*, Vol. 5, No. 2., pp. 365-377, 1973.
12. Sih, G.C., "Energy-density concept in fracture mechanics," *Engineering Fracture Mechanics*, Vol. 5, No. 4, pp. 1037-1040, 1973.
13. Sih, G.C., "Strain-energy-density factor applied to mixed-mode crack problems," *International Journal of Fracture*, Vol., 10, No. 3, pp. 305-321, 1974.
14. Gdoutos, E.E., *Fracture Mechanics: An Introduction*, 2<sup>nd</sup> ed., Springer, the Netherlands, Chapter 7, pp. 195-238, 2005.

15. Sih, G.C., and Macdonald, B., "Fracture Mechanics Applied to Engineering Problems – Strain Energy Density Fracture Criterion," *Engineering Fracture Mechanics*, Vol. 6, No. 2, pp. 361-386, 1974.
16. Alturi, S.N. and Nishioka, T., "Numerical studies in dynamic fracture mechanics," *International Journal of Fracture*, Vol. 27, pp. 245-261, 1985.
17. Kanninen, M.F., "A critical appraisal of solution techniques in dynamic fracture mechanics," *Numerical Methods in Fracture Mechanics*, pp. 612-634, 1978.
18. Aminjikai, S.B. and Tabiei, A., "Automated dynamic fracture procedure for modelling mixed-mode crack propagation using explicit time integration brick finite elements," *Engineering Materials & Structures*, Vol. 32, pp. 357-377, 2009.
19. Langseth, M., Lindholm, U.S., Larsen, P.K., and Lian, B., "Strain-Rate Sensitivity of Mild Steel Grade St52-3N," *Journal of Engineering Mechanics*, Vol. 117, No. 4, pp. 719-732, April 1991.
20. Fish, J. and Belytschko, T., *A First Course in Finite Elements*, John Wiley & Sons, Ltd., The Atrium, Southern Gate, Chichester, West Sussex, England, 2007.
21. Song, J-H, Wang, H., and Belytschko, T., "A comparative study on finite element methods for dynamic fracture," *Computational Mechanics*, Vol. 42, Issue 2, pp. 239-250, July 2008.
22. Kojima, S., Ishibashi, K., Yasuki, T., and Arimoto, H., "Development of Tied Overlapping Shell Technique to Simulate the Path of Crack Propagation in Polymer Parts," *12<sup>th</sup> International LS-DYNA Users Conference*, Simulation(1), June 2012.
23. Hallquist, J.O., *LS-DYNA Theoretical Manual*, Livermore Software Technology Corporation (LSTC), March 2006.
24. Erhart, T., "An Overview of User Defined Interfaces in LS-DYNA," *LS-DYNA Forum*, Bamberg, 2010.
25. Guo, Y. and Wu, C.T., "XFEM and EFG Cohesive Fracture Analysis for Brittle and Semi-Brittle Materials," *11<sup>th</sup> International LS-DYNA Users Conference*, Simulation(2), June 2010.
26. *LS-DYNA Keyword User's Manual*, Version 971, Livermore Software Technology Corporation (LSTC), May 2007.
27. Hillerborg, A., Modeer, M., and Petersson, P.-E., "Analysis of crack formation and crack growth in concrete by means of fracture mechanics and finite elements," *Cement and Concrete Research*, Vol. 6, Issue 6, pp. 773-781, November 1976.
28. Alfano, M., Furguele, F., Leonardi, A., Maletta, C., and Paulino, G.H. "Cohesive Zone Modeling of Mode I Fracture in Adhesive Bonded Joints," *Key Engineering Materials*, Vols. 348-349, pp. 13-16, September 2007.

29. Kregting, R. "Cohesive zone models towards a robust implementation of irreversible behaviour," A Thesis, University of Technology, Eindhoven, February 2005.
30. Agwai, A., Guven, I., and Madenci, E., "Predicting crack propagation with peridynamics: a comparative study," *International Journal of Fracture*, Vol. 171, Issue 1, pp. 65-78, September 2011.
31. Chikazawa, R., Komamura, T., Yamamoto, S., Yasuki, T., and Kojima, S., "Application of Crack Propagation Simulation of Windshield to Roof Strength Analysis," *12<sup>th</sup> International LS-DYNA Users Conference*, Automotive(2), June 2012.
32. Moes, N., Dolbow, J., and Belytschko, T., "A Finite Element Method for Crack Growth Without Remeshing," *International Journal for Numerical Methods in Engineering*, Vol. 46, Issue 1, pp. 131-150, September 1999.
33. Prabel, B., Marie, S., and Combescure, A., "Using the X-FEM method to model the dynamic propagation and arrest of cleavage cracks in ferritic steel," *Engineering Fracture Mechanics*, Vol. 75, Issue 10, pp. 2984-3009, July 2008.
34. Belytschko, T., Chen, H., Xu, J., and Zi, G., "Dynamic crack propagation based on loss of hyperbolicity and a new discontinuous enrichment," *International Journal for Numerical Methods in Engineering*, Vol. 53, pp. 1873-1905, 2003.
35. Comi, C. and Driemeier, L., "A nonlocal model for size effect and localization in plasticity," *Latin American Journal of Solids and Structures*, Vol. 2, No. 2, pp. 153-165, 2005.
36. Alder, B.J. and Wainwright, T.E., "Studies in Molecular Dynamics. I. General Method," *The Journal of Chemical Physics*, Vol. 31, Issue 2, pp. 459-466, February 1959.
37. Rahman, A., "Correlations in the Motion of Atoms in Liquid Argon," *Physical Review*, Vol. 136, Number 2A, pp. A405-A411, October 1964.
38. Bytnar, J., Kucaba-Pietal, A., and Walenta, Z., "Verification and Validation of Molecular Dynamics Simulations," *V European Conference on Computational Fluid Dynamics*, Lisbon, Portugal, June 2010.
39. Silling, S.A. and Lehoucq, R.B., "Peridynamic Theory of Solid Mechanics," Sandia National Laboratories, Report No. SAND 2010-1233J, Albuquerque, NM, April 2010.
40. Silling, S.A., "Reformulation of elasticity theory for discontinuities and long-range forces," *Journal of the Mechanics and Physics of Solids*, Vol. 48, pp. 175-209, April 1999.
41. Foster, J.T., "Dynamic Crack Initiation Toughness: Experiments and Peridynamic Modeling," Sandia National Laboratories, Report No. SAND 2009-7217, Albuquerque, NM, 2009.
42. Silling, S.A. and Lehoucq, R.B., "Convergence of Peridynamics to Classical Elasticity Theory," *Journal of Elasticity*, Vol. 93, Issue 1, pp. 13-37, October 2008.

43. Bobaru, F., Yang, M., Alves, L.F., Silling, S.A., Askari, E., and Xu, J., "Convergence, adaptive refinement, and scaling in 1D peridynamics," *International Journal for Numerical Methods in Engineering*, Vol. 77, Issue 6, pp. 852-857, August 2008.
44. Silling, S., "Peridynamic Modeling of the Failure of Heterogeneous Solids," *ARO Workshop on Analysis and Design of New Engineered Materials and Systems with Applications*, Sandia National Laboratories, Albuquerque, NM, February 2005.
45. Hu, W., "Peridynamic Models for Dynamic Brittle Fracture," Doctorate of Philosophy Dissertation, University of Nebraska-Lincoln, Lincoln, NE, March 2012.
46. Silling, S.A. and Askari, E., "A meshfree method based on the peridynamic model of solid mechanics," *Computers and Structures*, Vol. 83, pp. 1526-1535, March 2005.
47. Foster, J.T., Silling, S.A., and Chen, W.W., "Viscoplasticity using peridynamics," *International Journal for Numerical Methods in Engineering*, Vol. 81, Issue 10, pp. 1242-1258, August 2009.
48. Silling, S.A., Epton, M., Weckner, O., Xu, J., and Askari, E., "Peridynamic States and Constitutive Modeling," *Journal of Elasticity*, Vol. 88, pp. 151-184, July 2007.
49. Foster, J.T., Silling, S.A., and Chen, W., "An Energy Based Failure Criterion for Use with Peridynamic States," *International Journal for Multiscale Computational Engineering*, Vol. 9, Issue 6, pp. 675-687, 2011.
50. Ha, Y.D. and Bobaru, F., "Studies of dynamic crack propagation and crack branching with peridynamics," *International Journal of Fracture*, Vol. 162, pp. 229-244, January 2010.
51. Agwai, A., Guven, I., and Madenci, E., "Drop-Shock Failure Prediction in Electronic Packages by Using Peridynamic Theory," *IEEE Transactions on Components, Packaging and Manufacturing Technology*, Vol. 2, No. 3, pp. 439-447, March 2012.
52. Macek, R.W. and Silling, S.A., "Peridynamics via finite element analysis," *Finite Elements in Analysis and Design*, Vol. 43, Issue 15, pp. 1169-1178, November 2007.
53. Lall, P., Shantaram, S., and Panchagade, D., "Peridynamic-Models using Finite Elements for Shock and Vibration Reliability of Leadfree Electronics," *12<sup>th</sup> IEEE Intersociety Conference on Thermal and Thermomechanical Phenomena in Electronic Systems*, June 2010.
54. Beckmann, R., Mella, R., and Wenman, M.R., "Mesh and timestep sensitivity of fracture from thermal strains using peridynamics implemented in Abaqus," *Computational Methods in Applied Mechanics and Engineering*, Vol. 263, pp. 71-80, 2013.
55. Kilic, B. and Madenci, E., "Coupling of Peridynamic Theory and the Finite Element Method," *Journal of Mechanics of Materials and Structures*, Vol. 5, No. 5, pp. 707-733, December 2010.

56. Agwai, A., Guven, I., and Madenci, E., "Damage Prediction for Electronic Package Drop Test using Finite Element Method and Peridynamic Theory," *Proceedings – Electronic Components and Technology Conference*, 2009.
57. Oterkus, E., Madenci, E., Weckner, O., Silling, S., Bogert, P., and Tessler, A., "Combined finite element and peridynamic analyses for predicting failure in a stiffened composite curved panel with a central slot," *Composite Structures*, Vol. 94, Issue 3, pp. 839-850, February 2012.
58. Paulsen, G.W., Pfeifer, B.G., Holloway, J.C., and Reid, J.D., "Design and Testing of a Dual Support Breakaway Sign," Final Report to the Missouri Highway and Transportation Department, Transportation Research Report No. TRP-03-48-95, Midwest Roadside Safety Facility, University of Nebraska-Lincoln, September 6, 1995.
59. Paulsen, G.W., "Obtaining Stress/Strain Curves by Tensile Testing of Coupon Samples: No Theory, No Unneeded Discussion, Just Simple Instructions," Final Report to the Mechanical Engineering Department at the University of Nebraska-Lincoln, August 11, 1995.
60. Schmidt, J.D., Reid, J.D., Bielenberg, R.W., and Faller, R.K., "Numerical Investigation on the Performance of Steel Guardrails with Varied Mechanical Properties," Final Report to Advanced Coatings & Construction Solutions, Transportation Research Report No. TRP-03-290-13, Midwest Roadside Safety Facility, University of Nebraska-Lincoln, July 25, 2013.
61. Gurtin, Moron E., "An Introduction to Continuum Mechanics," *Mathematics in Science and Engineering*, Vol. 158, Edited by William F. Ames, Academic Press, San Diego, CA, 2003.
62. Spencer, A.J.M., *Continuum Mechanics*, Dover Publications, Mineola, NY, 1980.
63. Chadwick, P., *Continuum Mechanics: Concise Theory and Problems*, Dover Publications, Mineola, NY, 1976.
64. Rolfe, S.T. "Fracture and Fatigue Control in Steel Structures," *Engineering Journal*, American Institute of Steel Construction, First Quarter, 1977.
65. "Inspection, Evaluation, and Repair of Hydraulic Steel Structures," Engineer Manual, US Army Corps of Engineers, Engineering and Design, EM 1110-2-6045, Department of the Army, Washington, D.C., December 1, 2001.
66. Hallquist, J.O., "LS-DYNA Keyword User's Manual," Livermore Software Technology Corporation (LSTC), May 2007.
67. Davis, J.R., *Alloying: Understanding the Basics*, ASM International, Materials Park, Ohio, pp. 193-202, 2001.
68. ASTM Standard A572/A572M-12a, 2012, "Standard Specification for High-Strength Low-Alloy Columbium-Vanadium Structural Steel," ASTM International, West Conshohocken, PA, 2003, DOI: 10.1520/A0572\_A0562M-12A, [www.astm.org](http://www.astm.org).

69. Reid, J.D., Lechtenberg, K.A., and Stolle, C.S., "Development of Advanced Finite Element Material Models for Cable Barrier Wire Rope," Final Report to Mid-America Transportation Center, Report No. MATC-UNL:220, Transportation Research Report No. TRP-03-233-10, Midwest Roadside Safety Facility, University of Nebraska-Lincoln, August 2, 2010.
70. Baxter, J.R., Federal Highway Administration (FHWA), "Acceptance Letter – NCHRP Report 350 TL-3 Testing of the Tie-Down Steel H-Section Temporary Barrier," HAS-10/B-117, September 12, 2003.
71. "Instrumentation for Impact Test – Part 1: Electronic Instrumentation," *SAE J211/I*, SAE – Society of Automotive Engineers, Inc., 2007.
72. Young, W.C. and Budynas, R.G., *Roark's Formulas for Stress and Strain*, 7<sup>th</sup> ed., McGraw-Hill, New York, NY, 2002.
73. Inglis, C.E., "Stresses in a Plate Due to the Presence of Cracks and Sharp Corners," *Transactions of the Institute of Naval Architects*, Vol. 55, pp. 219-241, 1931.
74. Ray, M.H., Engstrand, K.E., Plaxico, C.A., and McGinnis, R.G., "Improvements to the Weak-Post W-Beam Guardrail," Transportation Research Board, Paper No. 01-2282, Washington, D.C., January 2001.
75. Buth, C.E., Menges, W.L., and Schoeneman, S.K., "NCHRP Report 350 Test 3-11 of the Modified PennDOT Type 2 Guide Rail," Report No. 473750-1, Texas Transportation Institute, The Texas A&M University System, College Station, TX, January 2000.
76. Polivka, K.A., Sicking, D.L., Reid, J.D., Faller, R.K., Rohde, J.R., and Holloway, J.C., "Guardrail and Guardrail Terminals Installed Over Curbs," Final Report to Midwest State's Regional Pooled Fund Program, Nebraska Department of Roads, Transportation Research Report No. TRP-03-83-99, Midwest Roadside Safety Facility, University of Nebraska-Lincoln, Lincoln, NE, March 21, 2000.
77. Pfeifer, B.G., Reid, J.D., Faller, R.K., Sicking, D.L., and Holloway, J.C., "Development of a Test Level 3 Guardrail System," Final Report to Mr. William A. Weseman, Federal Highway Administration, Transportation Research Report No. TRP-03-58-96, Midwest Roadside Safety Facility, University of Nebraska-Lincoln, Lincoln, NE, April 1996.



## **13 APPENDICES**

### **Appendix A. Dynamic Component Test Setup Details**

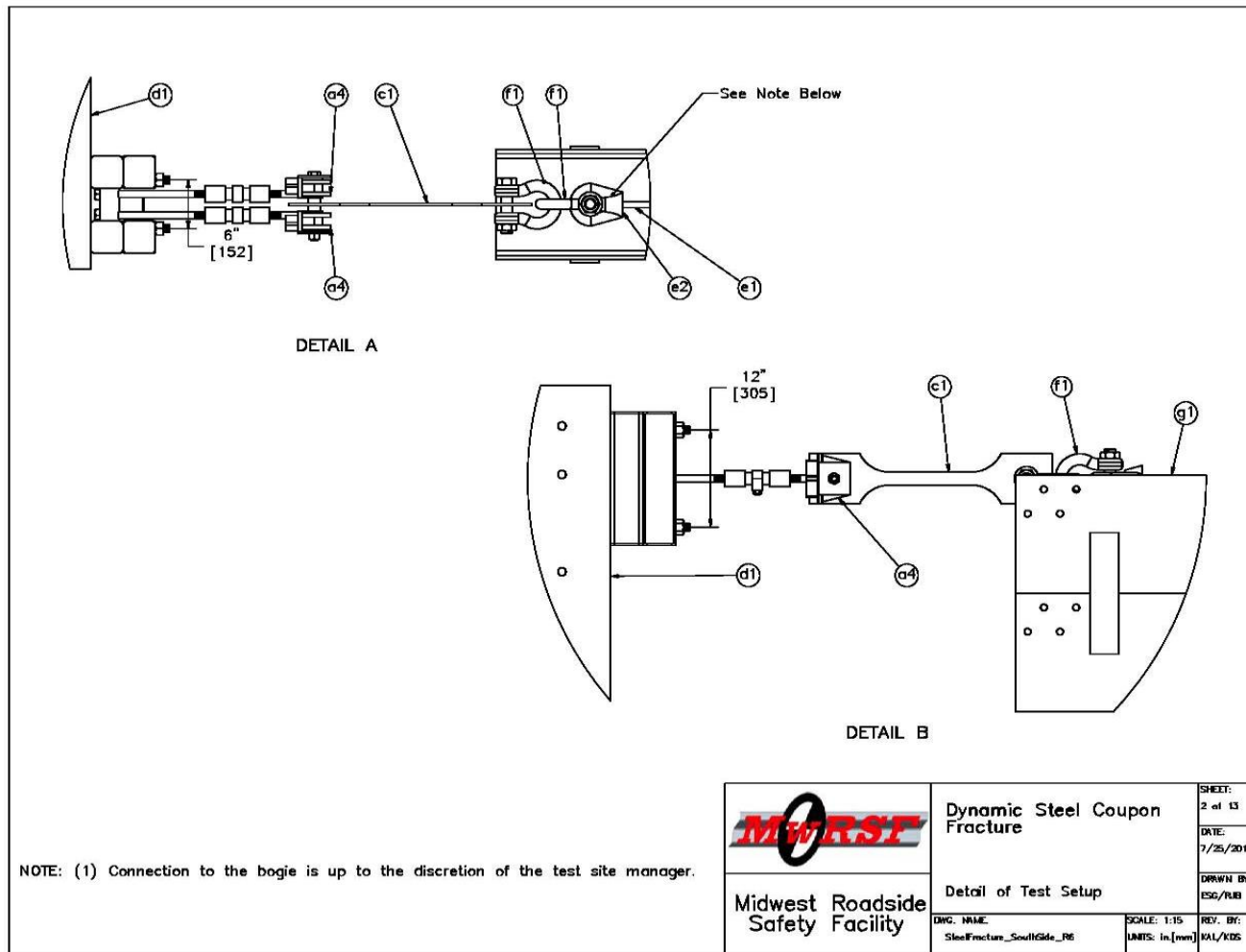


Figure A-1. Detail of Test Setup

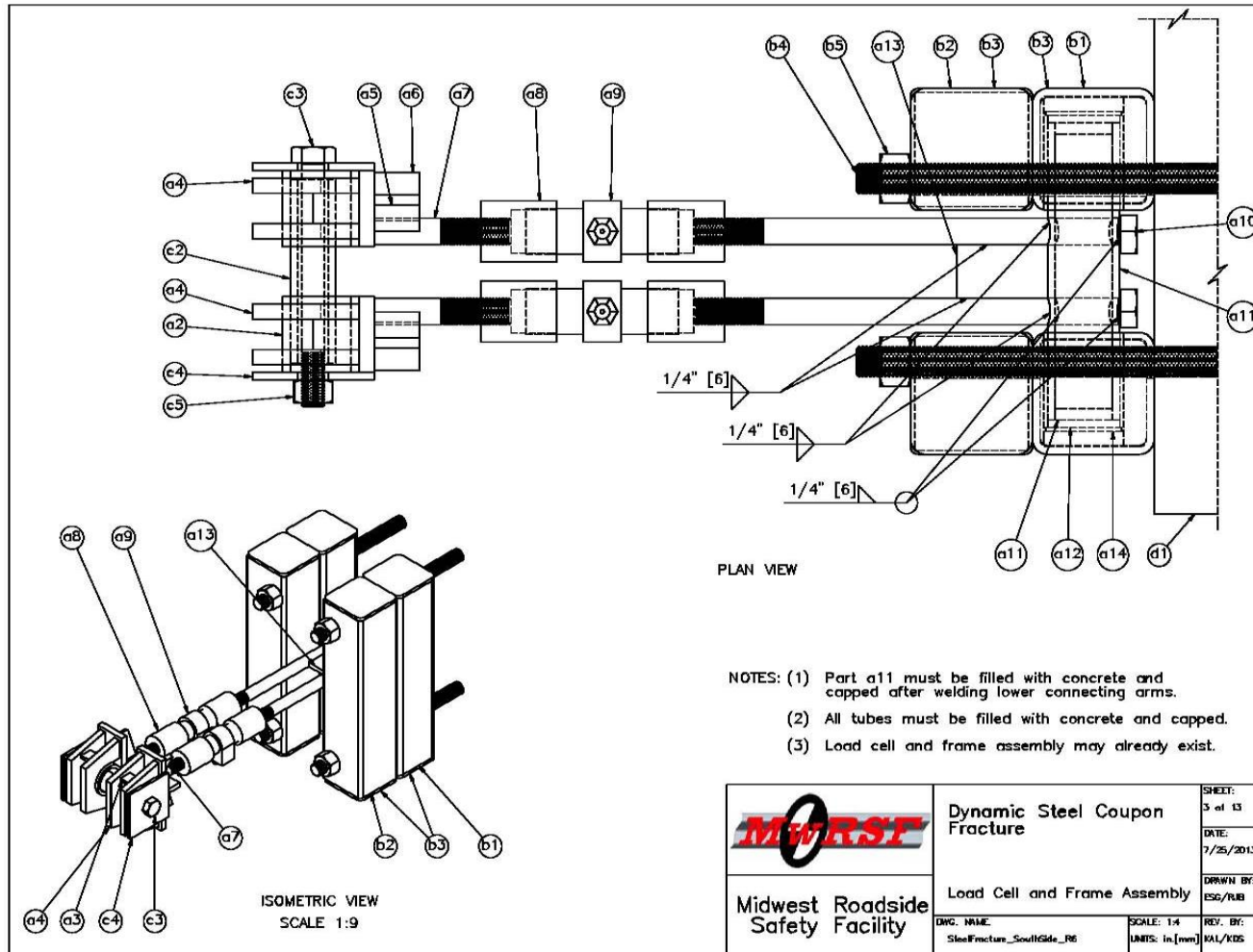


Figure A-2. Load Cell Assembly and Coupon Mounting Frame

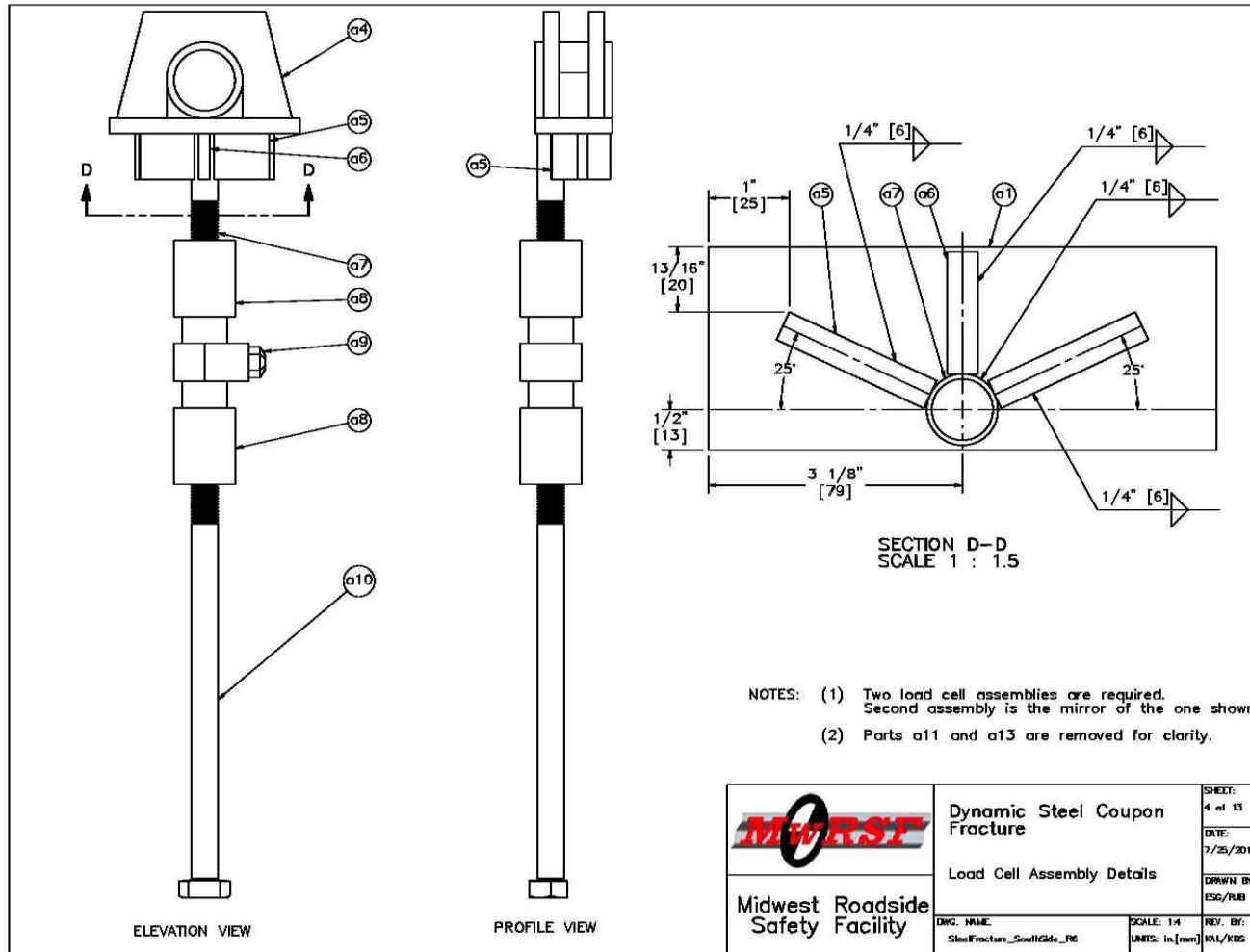


Figure A-3. Load Cell Assembly Details

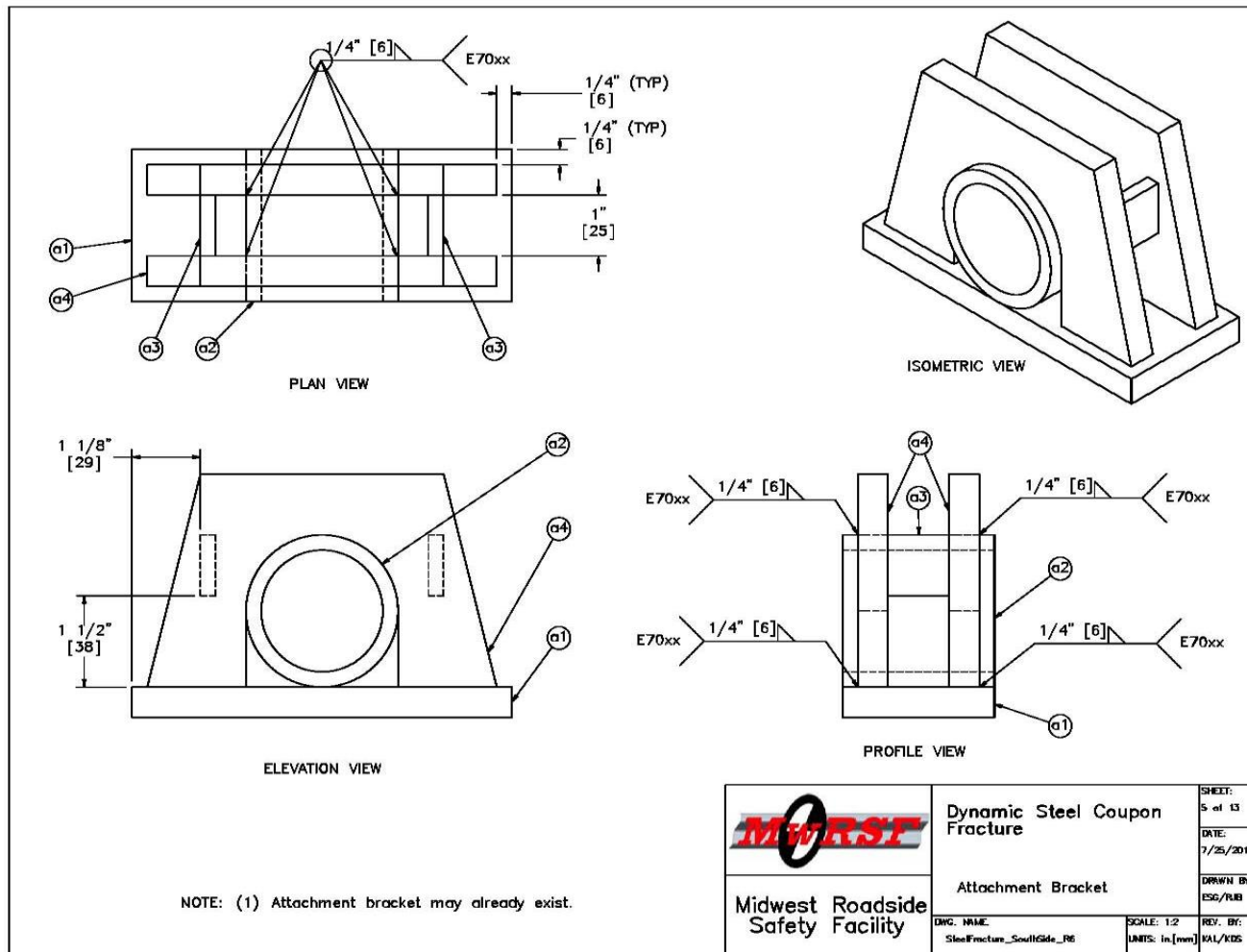


Figure A-4. Coupon Mounting Bracket Details

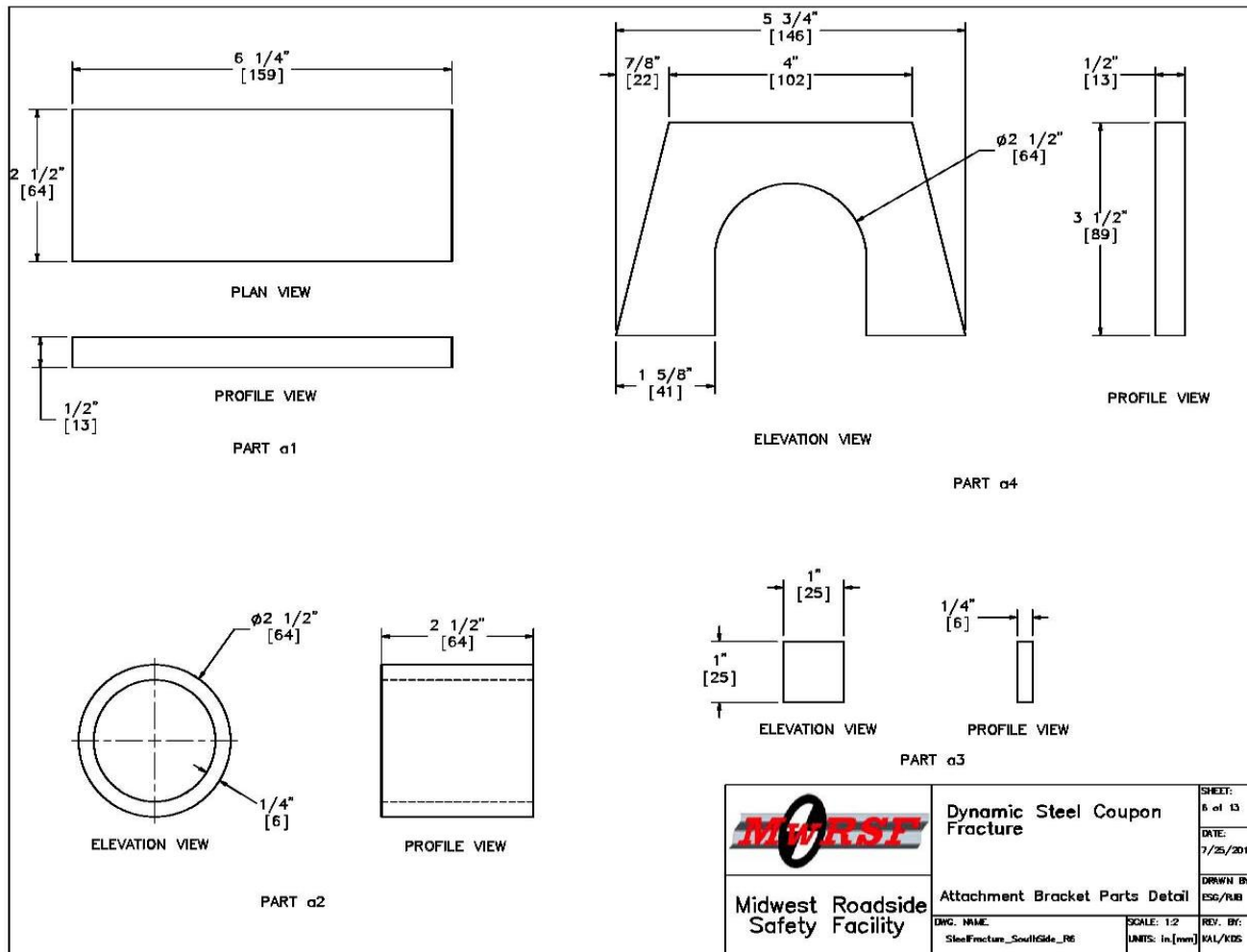


Figure A-5. Coupon Mounting Bracket Part Details

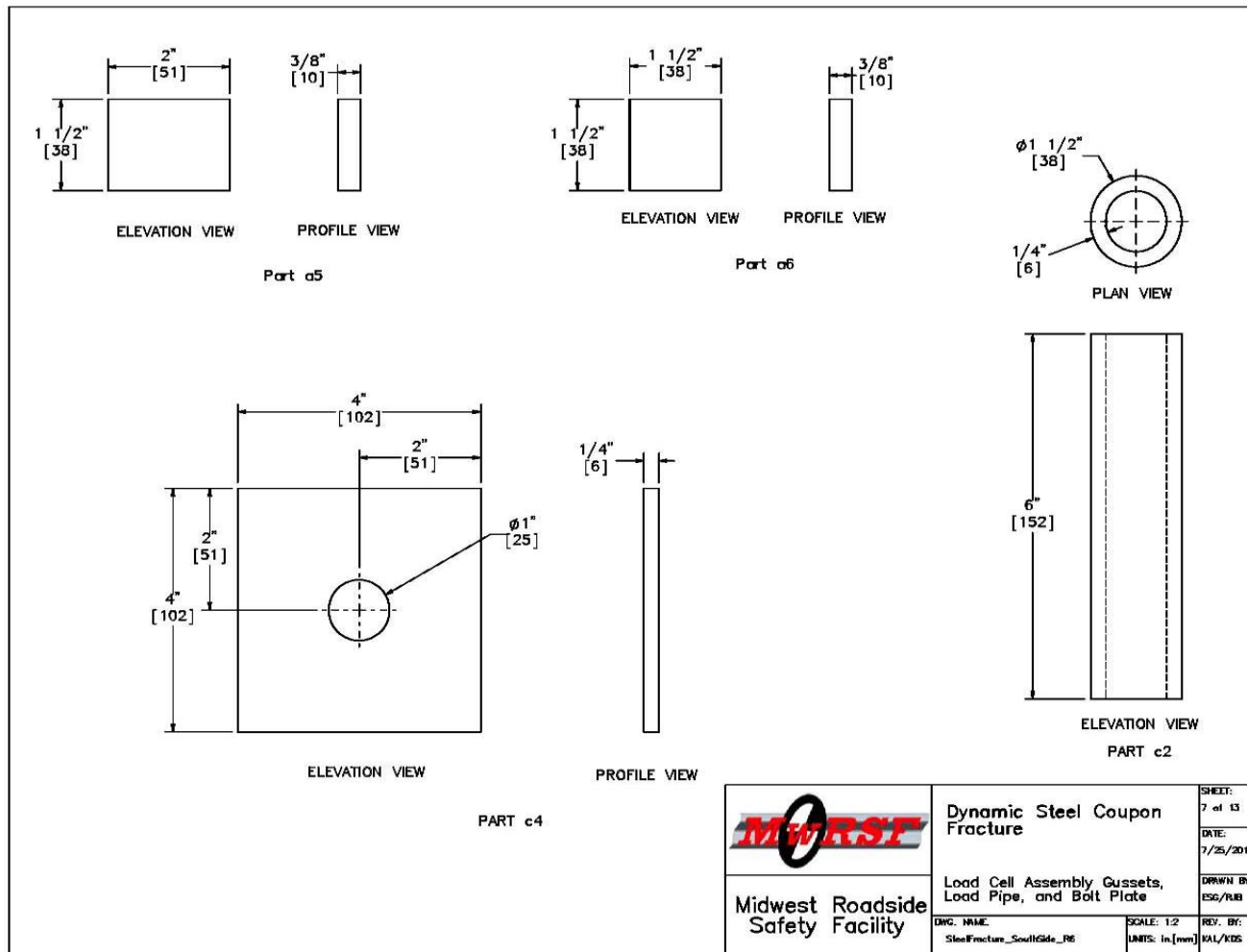


Figure A-6. Part Details for the Load Cell Assembly

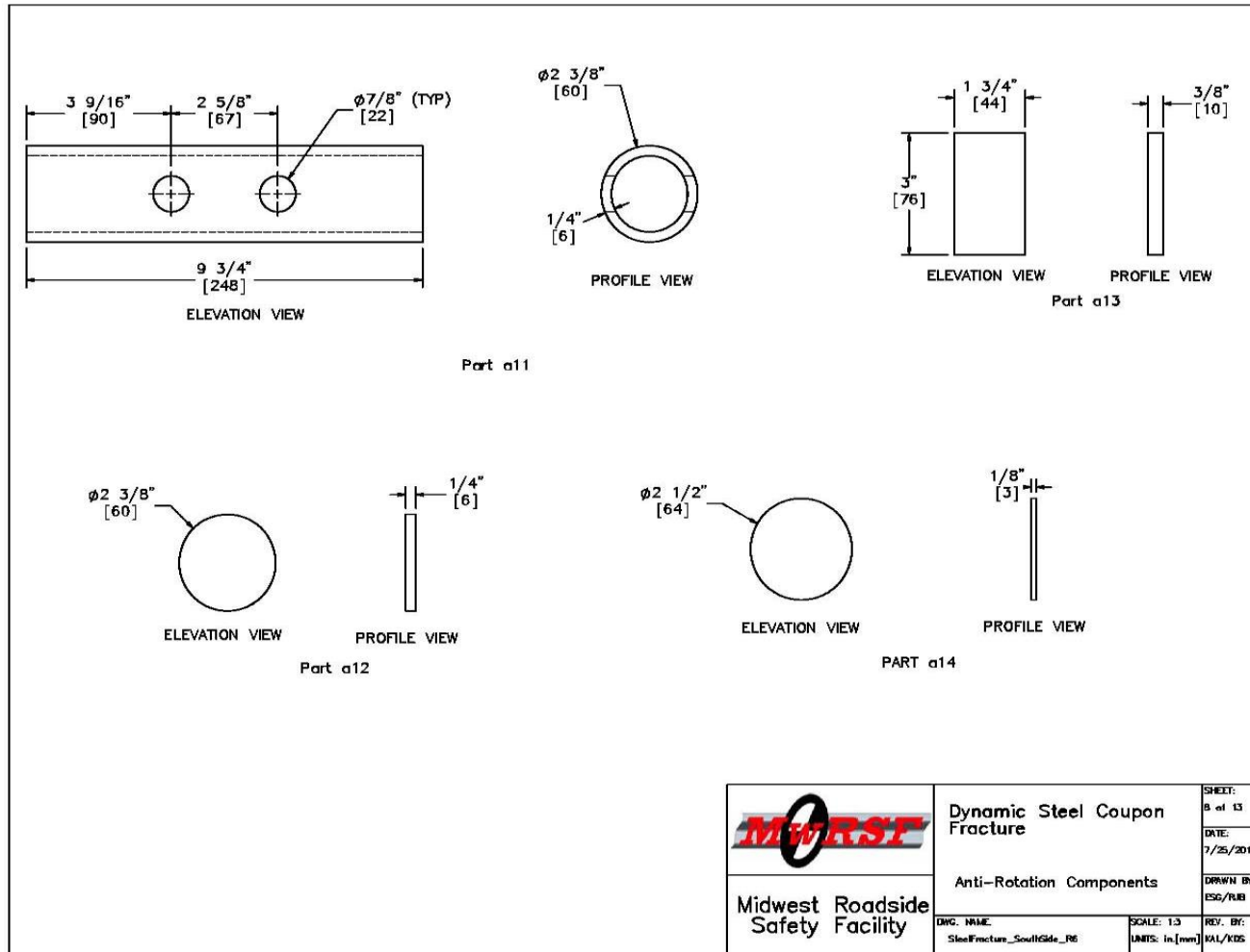


Figure A-7. Anti-Rotation Components of Load Cell Assembly



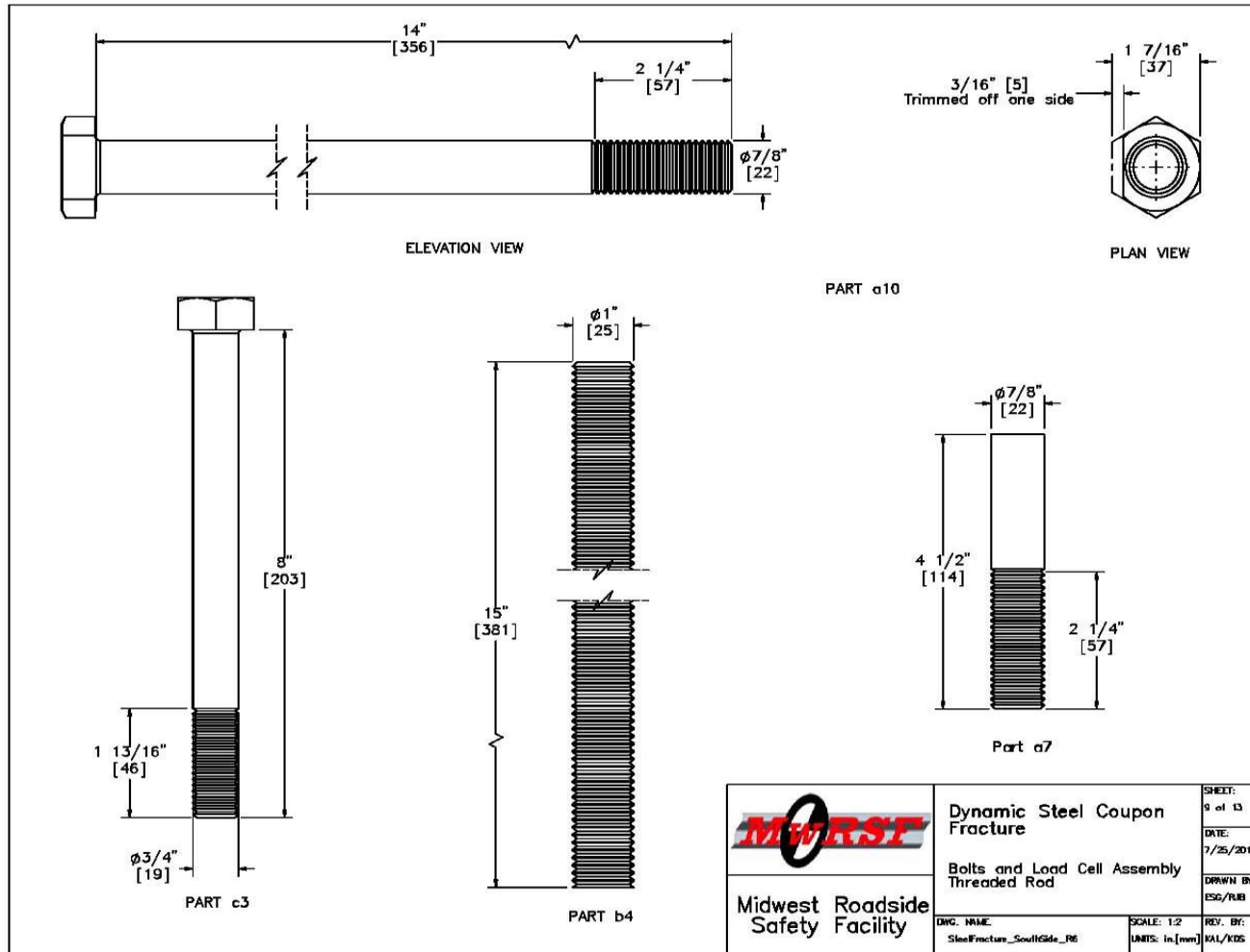


Figure A-8. Bolts and Threaded Rod of the Load Cell Assembly

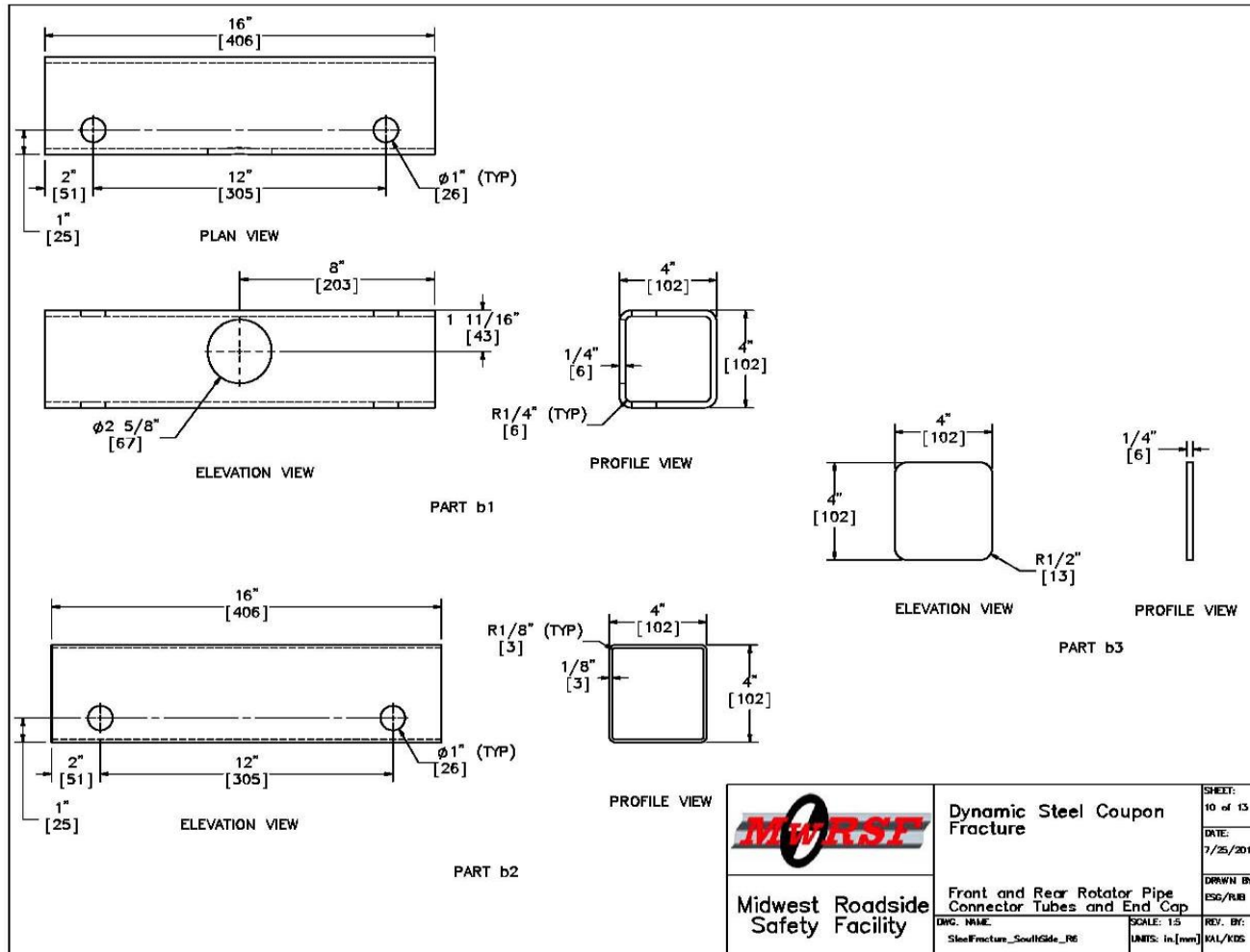


Figure A-9. Concrete-Filled Tubes Attached to the Bogie Block

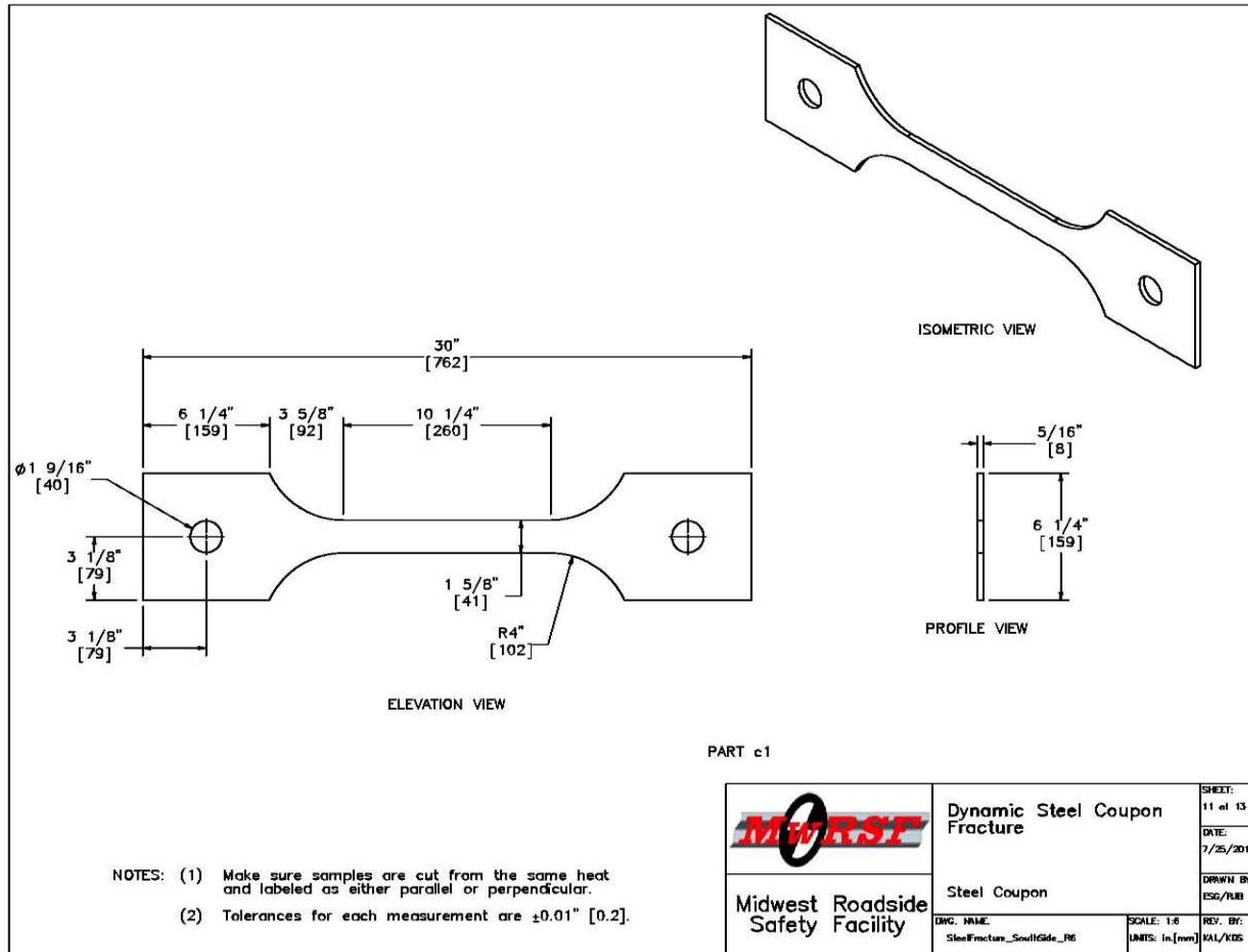


Figure A-10. Enlarged A572 Gr 50 Steel Coupon

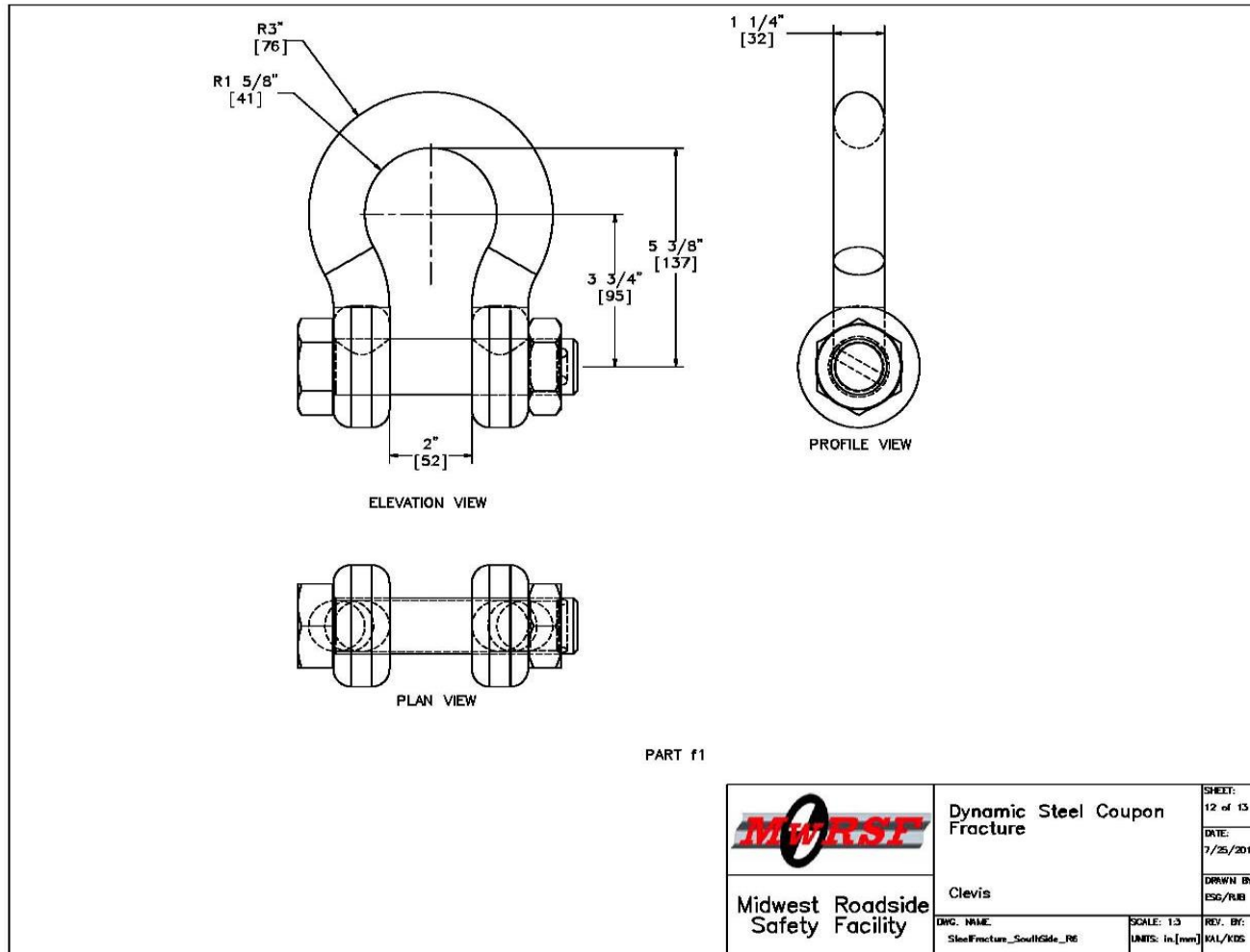


Figure A-11. Detail of Clevis Used to Connect Coupon to Bogie

Item No.	QTY.	Description	Material Specification
a1	2	Tensile Bracket Baseplate	ASTM A36
a2	2	Tensile Bracket Load Pipe	ASTM A36
a3	4	Tensile Bracket Spacer	ASTM A36
a4	4	Tensile Bracket Rib	ASTM A36
a5	4	Angled Gusset	ASTM A36
a6	2	Center Gusset	ASTM A36
a7	2	7/8" [22] dia., -9 UNC, 6" [152] Long Threaded Rod	ASTM A325
a8	4	Load Cell Coupler	Pre-Fabricated
a9	2	50 kip Tension Load Cell	TLL-50K-PTB
a10	2	7/8" [22] dia., -9 UNC, 14" [356] Long Bolt	ASTM A325
a11	1	Rotator Pipe	Located in Shop
a12	2	Rotator Pipe Cap	ASTM A36
a13	1	Rotator Pipe Gusset	ASTM A36
a14	2	Neoprene Bearing Pad	Neoprene
b1	2	Long Lower Support Tube	Located in Shop
b2	2	Long Upper Support Tube	Located in Shop
b3	8	Long Tube End Cap	ASTM A36
b4	4	1" [25]-8 UNC, 15" [381] Long Threaded Rod	ASTM A325
b5	4	1" [25]-8 UNC Heavy Hex Nut	ASTM A325
c1	1	Steel Coupon	A500 Grade C or A572 Grade 50
c2	1	Load Pipe	ASTM A36
c3	1	3/4" [19]-10 UNC, 8" [203] Long Bolt	ASTM A325
c4	2	Load Pipe Bearing Plate	ASTM A36
c5	1	Load Pipe Connector Nut	ASTM A325
d1	1	Bogie Block	Pre-Fabricated
e1	1	Cable (up to the discretion of the test site manager)	-
e2	1	Cable Connector (up to the discretion of the test site manager)	-
f1	2	Crosby G2130 or S2130 Bolt Type Shackle - 1 1/4" [32] Dia. with thin head bolt, nut, and cotter pin, Grade A, Class 3	Stock Nos. 1019597 and 1019604 - As Supplied
g1	1	240" [6096] Long H-Barrier	Pre-Fabricated
i1		Concrete for Rotator Pipe and Rotator Pipe Connector Tubes	min f'c=3 ksi [20.7MPa]


 Midwest Roadside Safety Facility	Dynamic Steel Coupon Fracture		SHEET: 13 of 13
	Bill of Materials		DATE: 7/25/2013
	DWG. NAME: SteelFracture_SouthSide_R6	SCALE: NONE UNITS: in./mm	DRAWN BY: ESG/RJB
		REV. BY: KAL/KDS	

Figure A-12. Bill of Materials for Dynamic Component Testing

## **Appendix B. Material Specifications**

bl-466

Heat - A213858  
Order-Line - 9566101 / 1

BL - 61081121  
Load - 1725220

07-10-2013 21:53  
Sioux City Foundry  
Cust. PO - 153005W

## Metallurgical Certification

Order Number: 198086  
Order Dimensions: 0.3650X72.0000 (IN)  
Ordered Product: A572 GRADE 50 TYPE 1  
Part Number: HOT ROLLED BLACK - PRIME  
Alt Part#: HR .3650X72.0000\*

Chemical Analysis:

Coil Number:	Heat:	C	Mn	P	S	Si	Cu	Sn	Ni	Cr	Mo	Al	N	V	Cb	Ti	B	Ca	C(eq)
A213858-02	A213858	.06	.62	.008	.003	.02	.10	.0060	.04	.04	.010	.023	.0062	.003	.027	.001	.0003	.0014	.120

Mechanical Properties:

	English	Metric
Yield Strength	63.7 ksi	439 MPA
Tensile Strength	71.9 ksi	496 MPA
Elongation	33 %	33 %
N-Value	.00	.00
Hardness - Rb	0	0
Direction	T	T
Linear Footage	539 F	164 M

Certificate Date: 11/21/2012

Certified by: Sabyasachi Bandyopadhyay  
Sabyasachi Bandyopadhyay  
Quality Manager

We hereby certify the above is correct as contained in the records of the company. All tests performed according to ASTM standard E8, A370, E18, E415, and E1019 (yield strength determined using 0.2% offset method) or JIS Z2241.

THIS PRODUCT WAS MELTED AND MANUFACTURED IN THE USA

4283199

Figure B-1. A572 Gr 50 Steel Coupon

TEST REPORT																																																																					
ORDER, CONTRACT NO.					PLATE ORDER NO.																																																																
<b>VEENDOR</b> <b>ArcelorMittal USA Inc.</b> QUALITY DEPARTMENT 2-106 3210 WATLING STREET EAST CHICAGO, INDIANA 46312					<b>SHIPPER'S NO.</b> F161661																																																																
					<b>INVOICE NO.</b> 1024332																																																																
					<b>REPORT DATE</b> 12/23, 2012																																																																
					<b>INVOICE DATE</b> 12/23, 2012																																																																
<b>VEHICLE CONFIGURATION</b> IHB /167177					<b>INVOICE NO.</b> F131631																																																																
<b>SOLD TO</b> STATE STEEL SUPPLY CO PO BOX 3224 SIOLK CITY IA 51102					<b>SHIP TO</b> STATE STEEL OF OMAHA THEIR SIDING BNSF TRACK #1740-01 CHALCO NE 68138																																																																
<b>SPECIFICATION</b> ARCELORMITTAL / HOT ROLLED STEEL / COILS / HSLAS-F / INCLUSION SHAPE CONTROL / ASTM A 1011-12B GR 50 / NON TEMPER ROLLED / MILL EDGE																																																																					
<table border="1"> <thead> <tr> <th rowspan="2">ITEM NO.</th> <th rowspan="2">ORDER DESCRIPTION</th> <th rowspan="2">QUANT.</th> <th rowspan="2">WEIGHT (LBS)</th> <th rowspan="2">HEAT NO.</th> <th colspan="4">COIL/LIFT IDS</th> <th colspan="4">TEST RESULTS</th> </tr> <tr> <th>OSP/ARCELORMITTAL DIR</th> <th>YIELD PSI</th> <th>TENSILE PSI</th> <th>STR ELONG IN %</th> </tr> </thead> <tbody> <tr> <td rowspan="2">.1278 IN X 60.2500 IN COIL</td> <td rowspan="2"></td> <td rowspan="2"></td> <td rowspan="2">46102</td> <td rowspan="2">231232</td> <td>06952992</td> <td>L</td> <td>57,700</td> <td>67,700</td> <td>2 31</td> </tr> <tr> <td>L</td> <td>60,000</td> <td>69,300</td> <td>2 31</td> </tr> </tbody> </table>										ITEM NO.	ORDER DESCRIPTION	QUANT.	WEIGHT (LBS)	HEAT NO.	COIL/LIFT IDS				TEST RESULTS				OSP/ARCELORMITTAL DIR	YIELD PSI	TENSILE PSI	STR ELONG IN %	.1278 IN X 60.2500 IN COIL			46102	231232	06952992	L	57,700	67,700	2 31	L	60,000	69,300	2 31																													
ITEM NO.	ORDER DESCRIPTION	QUANT.	WEIGHT (LBS)	HEAT NO.	COIL/LIFT IDS				TEST RESULTS																																																												
					OSP/ARCELORMITTAL DIR	YIELD PSI	TENSILE PSI	STR ELONG IN %																																																													
.1278 IN X 60.2500 IN COIL			46102	231232	06952992	L	57,700	67,700	2 31																																																												
					L	60,000	69,300	2 31																																																													
<p>All tests were performed by ArcelorMittal Indiana Harbor Microtest Lab, unless otherwise specified. In accordance with the following: chemical analysis per ASTM A415 and E1010; mechanical properties per ASTM A370, 92, 95T, 9846, 98 22201, 22201, 22201, 22201, 22201, and ISO 6893-1; hardness per ASTM E10; core loss and permeability per ASTM A362; coating weight per ISO 1460 and ASTM A563; A428 and A574; sulfuration per head tests for powdering; surface roughness per AAS (AASME 846.1 and 846.2); and Charpy impact per ASTM E23 and A370. All tests performed in the current version of the standard, unless otherwise noted. These results relate only to the items from the heat or coil tested.</p> <table border="1"> <thead> <tr> <th colspan="15">HEAT ANALYSIS (wt. %)</th> </tr> <tr> <th>HEAT NO.</th> <th>C</th> <th>Mn</th> <th>P</th> <th>S</th> <th>Si</th> <th>Cu</th> <th>Al</th> <th>Mo</th> <th>Cr</th> <th>Nb</th> <th>V</th> <th>As</th> <th>Sn</th> <th></th> </tr> </thead> <tbody> <tr> <td>231232</td> <td>.05</td> <td>1.02</td> <td>.006</td> <td>.003</td> <td>.02</td> <td>&lt;.02</td> <td>&lt;.02</td> <td>&lt;.02</td> <td>.03</td> <td>.02</td> <td>&lt;.006</td> <td>.042</td> <td>&lt;.02</td> <td></td> </tr> <tr> <td colspan="15">           T I N B            .014.0071 .0001         </td> </tr> </tbody> </table>										HEAT ANALYSIS (wt. %)															HEAT NO.	C	Mn	P	S	Si	Cu	Al	Mo	Cr	Nb	V	As	Sn		231232	.05	1.02	.006	.003	.02	<.02	<.02	<.02	.03	.02	<.006	.042	<.02		T I N B .014.0071 .0001														
HEAT ANALYSIS (wt. %)																																																																					
HEAT NO.	C	Mn	P	S	Si	Cu	Al	Mo	Cr	Nb	V	As	Sn																																																								
231232	.05	1.02	.006	.003	.02	<.02	<.02	<.02	.03	.02	<.006	.042	<.02																																																								
T I N B .014.0071 .0001																																																																					
MELTED AND MANUF IN USA																																																																					

Figure B-2. A1011-12B Gr 50 Thin Steel Coupon



# Certified Analysis



Trinity Highway Products, LLC  
 550 East Robb Ave.  
 Lima, OH 45801  
 Customer: MIDWEST MACH & SUPPLY CO.  
 P. O. BOX 703  
 MILFORD, NE 68405  
 Project: STOCK

Order Number: 1201693 Prod Ln Grp: 3-Guardrail (Dom)  
 Customer PO: 2790  
 BOL Number: 77138 Ship Date:  
 Document #: 1  
 Shipped To: NE  
 Use State: NE

As of: 8/14/13

Nov. 8, 2013 7:32AM

Qty	Part #	Description	Spec	CL	TY	Heat Code/ Heat	Yield	TS	Elg	C	Mn	P	S	Si	Cu	Cr	Vn	ACW
40	11G	12/12*59*1.5/8			2	L12913												
			M-180	A	2	167153	55,100	70,690	32.0	0.180	0.730	0.011	0.005	0.010	0.070	0.000	0.050	0.000 4
			M-180	A	2	168413	54,570	71,150	31.7	0.190	0.720	0.012	0.004	0.020	0.130	0.000	0.070	0.001 4
			M-180	A	2	168414	56,130	72,780	29.6	0.200	0.730	0.011	0.002	0.020	0.130	0.000	0.070	0.001 4
			M-180	A	2	168752	58,510	75,350	31.7	0.200	0.730	0.010	0.005	0.020	0.120	0.000	0.050	0.001 4
			M-180	A	2	168937	57,020	73,770	28.9	0.190	0.730	0.012	0.004	0.010	0.130	0.000	0.070	0.000 4
			M-180	A	2	168938	56,060	73,910	29.7	0.190	0.720	0.012	0.004	0.010	0.130	0.000	0.060	0.001 4
			M-180	A	2	168940	54,140	72,360	30.1	0.200	0.750	0.011	0.006	0.010	0.140	0.000	0.060	0.001 4
20	907G	12/BUFFER/ROLLED	M-180	A	2	4145107	47,400	66,500	32.0	0.200	0.380	0.005	0.008	0.010	0.020	0.000	0.030	0.002 4
10	923G	BRONSTAD 94"W/O	M-180	A	2	4145107	47,400	66,500	32.0	0.200	0.380	0.005	0.008	0.010	0.020	0.000	0.030	0.002 4
18	929G	10/BND SHO/RS2 EXT	M-180	B	2	C65380	61,000	84,500	23.2	0.210	0.810	0.018	0.005	0.020	0.110	0.003	0.050	0.001 4
4	2030G	12/12*6*3/8 30"RCC			2	L12013												
			M-180	A	2	166224	58,340	74,860	32.3	0.190	0.730	0.011	0.004	0.010	0.130	0.000	0.090	0.001 4
			M-180	A	2	166282	58,270	74,990	26.7	0.190	0.720	0.011	0.002	0.020	0.120	0.000	0.070	0.001 4
			M-180	A	2	166767	56,550	73,470	27.8	0.190	0.730	0.009	0.004	0.010	0.070	0.000	0.040	0.001 4
			M-180	A	2	166768	59,620	75,820	26.8	0.200	0.740	0.009	0.004	0.020	0.080	0.001	0.050	0.000 4
					2	166769												
			M-180	A	2	167156	57,160	74,250	30.1	0.190	0.710	0.008	0.004	0.020	0.090	0.000	0.040	0.000 4
			M-180	A	2	41315760	67,000	87,600	27.0	0.200	0.870	0.007	0.002	0.030	0.080	0.000	0.030	0.001 4
			M-180	A	2	166224	58,340	74,860	32.3	0.190	0.730	0.011	0.004	0.010	0.130	0.000	0.090	0.001 4
			M-180	A	2	166282	58,270	74,990	26.7	0.190	0.720	0.011	0.002	0.020	0.120	0.000	0.070	0.001 4
			M-180	A	2	166767	56,550	73,470	27.8	0.190	0.730	0.009	0.004	0.010	0.070	0.000	0.040	0.001 4
			M-180	A	2	166768	59,620	75,820	26.8	0.200	0.740	0.009	0.004	0.020	0.080	0.001	0.050	0.000 4

Nov. 5, 2012 9:11

Figure B-3. AASHTO M180 Steel Coupons

## **Appendix C. FORTRAN Post-Processing Code**

```

program nodal_analysis

!=====
! Declare variables
!=====
integer::i,nodes,steps,f,t,nid2,j,count_max

integer,allocatable::nid(:,,:),count(:,),nid3(:,),index(:)
integer,allocatable::X_node(:,),count_nom(:)

character::fluff

real::delta1,E,SED_crit,x2,y2,dist,factor, node_spacing
real::sig_y,e_y,sig_y_t,SED_crit_n,Fail

real,allocatable::time(:,),x(:,),y(:,),YM(:)
real,allocatable::SED_node(:,),dist_0(:,),dx(:,),dy(:,)
real,allocatable::e_y_t(:,),SED_truss(:,)

!=====
! Open input and output files
!=====
OPEN(unit=100,file='nodout')
OPEN(unit=101,file='nodes.k')
OPEN(unit=102,file='input.txt')
OPEN(unit=200,file='output.txt')

write(200,*)"Nodal Failure Times"
write(200,*)"      nid      time"

!=====
! Read 'input.txt' file (unit = 102)
! Calculate length scale and failure scale factor
!=====
read(102,*)
read(102,*)nodes
read(102,*)
read(102,*)steps
read(102,*)
read(102,*)node_spacing
read(102,*)
read(102,*)factor
read(102,*)
read(102,*)E
read(102,*)
read(102,*)SED_crit
read(102,*)
read(102,*)sig_y

delta1=factor*node_spacing

Fail=(-185.4*log(node_spacing)+443.64)*0.1341*exp(0.4082*factor)

```

```

SED_crit_n=Fail*SED_crit

e_y=sig_y/E
sig_y_t=sig_y

!=====
! Allocation and Formatting
!=====
allocate(time(steps+1),x(steps+1,nodes),y(steps+1,nodes))
allocate(nid(steps+1,nodes),e_y_t(nodes))
allocate(SED_node(steps+1,nodes),dist_0(nodes,nodes))
allocate(dx(steps+1,nodes),dy(steps+1,nodes))
allocate(count(nodes),YM(nodes),strain(steps,nodes))
allocate(stress(steps,nodes),SED_truss(steps,nodes))

10 FORMAT(I10,F12.5,F12.5)
20 FORMAT(A104,F12.5)

!=====
! Input
!=====
read(101,*)
read(101,*)
do i=1,nodes
  read(101,*)nid(1,i),x(1,i),y(1,i)
end do

do f=1,4
  read(100,*)
end do

do t=1,steps
  read(100,*)
  read(100,*)
  read(100,*)
  read(100,20)fluff,time(t)
  read(100,*)
  read(100,*)
  do i=1,nodes
    read(100,10)nid(t,i),dx(t,i),dy(t,i)
    x(t,i)=x(1,i)+dx(t,i)
    y(t,i)=y(1,i)+dy(t,i)
  enddo
  do f=1,(nodes+6)
    read(100,*)
  end do
end do

!=====
! Initial truss lengths and number of trusses around each node
!=====

```

```

count_max=0

do i=1,nodes
  do j=1,nodes
    nid2=nid(1,j)
    x2=x(1,j)
    y2=y(1,j)
    dist_0(i,j)=sqrt((x2-x(1,i))**2+(y2-y(1,i))**2)
    if(nid2.ne.nid(1,i))then
      if(dist_0(i,j)<=delta1)then
        count(i)=count(i)+1
      end if
    end if
    if(count(i)>count_max)then
      count_max=count(i)
    end if
  end do
end do

!=====
! SED calculations around each node
! including a check of the failure parameter
!=====
do t=1,steps
  print*,(real(t)*100./real(steps))
  do i=1,nodes
    YM(i)=(2.*E/(3.14159*9.))*count_max/count(i)
    e_y_t(i)=sig_y_t/YM(i)
    do j=1,nodes
      nid2=nid(1,j)
      x2=x(t,j)
      y2=y(t,j)
      dist=sqrt((x2-x(t,i))**2+(y2-y(t,i))**2)
      if(dist_0(i,j)<=delta1)then
        if(nid2.ne.nid(1,i))then
          strain(t,j)=abs((dist-(dist_0(i,j)))/dist_0(i,j))
          stress(t,j)=strain(t,j)*YM(i)
          if(stress(t,j)>sig_y)then
            stress(t,j)=sig_y
          end if
          SED_truss(t,j)=abs(strain(t,j)-strain(t-1,j)) &
            *((stress(t,j)+stress(t-1,j))/2.)
          SED_node(t,i)=SED_node(t,i)+SED_truss(t,j)
        end if
      end if
    end do
    if(SED_node(t,i).ge.SED_crit_n.and. &
      SED_node(t-1,i).lt.SED_crit_n)then
      write(200,*)nid(t,i),time(t)
    end if
  end do
end do

```

end program

## **Appendix D. Example “nodes.k” File**

```
*NODE
$#   nid      x      y      z      tc      rc
      1      245.339005      58.799500      0.000      0      0
      2      245.339005      62.228741      0.000      0      0
      3      248.770126      58.799500      0.000      0      0
      4      245.339005      65.657982      0.000      0      0
      5      248.769882      62.228981      0.000      0      0
      6      252.201263      58.799500      0.000      0      0
      7      245.339005      69.087227      0.000      0      0
*END
```



## **Appendix E. Example of “input.txt” File**

enter number of nodes:  
1040  
enter number of time steps to analyze:  
1000  
enter nodal spacing:  
3.45  
enter length scale factor:  
5.0  
enter Young's Modulus:  
200  
enter critical SED:  
0.145  
enter yield stress:  
0.439

**END OF DOCUMENT**